

**Modeling the Structure of the Proton: Deeply Virtual  
Compton Scattering and Generalized Parton  
Distributions**

A dissertation submitted by  
**Jonathon Poage**

in partial fulfillment of the requirements for the degree of  
**Doctor of Philosophy**  
**in**  
**Physics**

Tufts University

February 11, 2017

Adviser: Gary Goldstein

**Abstract:** The structure of the proton and its role in Deeply Virtual Compton Scattering (DVCS) are investigated using the spectator model and Generalized Parton Distributions (GPDs). DVCS is a well established means for probing the internal structure of the proton, and GPDs are mathematical objects that are useful for describing the proton's structure with more complexity than Parton Distribution Functions (PDFs). The soft parts of the DVCS amplitudes are evaluated with a partonic interpretation by using the framework of the spectator model, and parametrized models are formed for quark, antiquark, and gluon GPDs. Several parameters for the GPDs are obtained by fitting the GPDs to established PDF parametrizations, as part of an iterative fit procedure. The applications of the GPDs and their contributions to DVCS observables are then explored.

**Acknowledgements:** I would like to express my gratitude to my adviser, Gary Goldstein, for his patience and unwavering guidance throughout my studies. He has my appreciation for enriching my graduate education with his invaluable insight.

I would like to thank Simonetta Liuti and Abha Rajan for their thoughtful support, as well as for their hospitality during my time in Virginia. I thank J. Osvaldo Gonzalez-Hernandez for graciously mentoring me throughout my studies. I would also like to extend my appreciation to the students, faculty, and staff at Tufts, both in the physics department and elsewhere, for making my time as a graduate student a tremendous experience.

I thank my family for their continual optimism and encouragement, which bolstered my confidence and my resolve. I extend a special thanks to my wife, Nhu-Y Le, for her loving support in every year of my graduate education.

# Contents

<b>1</b>	<b>Introduction</b>	<b>2</b>
1.1	Overview . . . . .	2
1.2	The Parton Model . . . . .	5
1.2.1	Electron-Proton Scattering . . . . .	6
1.2.2	Form Factors and Structure Functions . . . . .	8
1.2.3	Bjorken Scaling . . . . .	11
1.2.4	Parton Distribution Functions . . . . .	13
1.3	Generalized Parton Distributions . . . . .	15
1.3.1	Forward Scattering Amplitude . . . . .	15
1.3.2	Current Expansion . . . . .	18
1.3.3	Handbag Model . . . . .	21
1.3.4	Helicity Conserving GPDs . . . . .	25
1.4	Partonic Interpretation and Light-Cone Helicity . . . . .	27
1.4.1	Light-Cone Quantization . . . . .	27
1.4.2	Partonic Interpretation . . . . .	30
1.4.3	LC Helicity Amplitudes . . . . .	33

1.4.4	Gluon Fields in the $A^+ = 0$ Gauge . . . . .	35
1.5	GPD Properties . . . . .	36
1.5.1	Polynomiality and Moments in $x$ . . . . .	38
1.6	Modeling the GPDs . . . . .	43
<b>2</b>	<b>Kinematics</b>	<b>44</b>
2.1	Conventions . . . . .	44
2.2	Kinematics . . . . .	46
2.2.1	Note on Kinematic Regions of $x$ . . . . .	48
2.3	Spinors and Polarization Vectors . . . . .	50
2.3.1	Spin $\frac{1}{2}$ . . . . .	50
2.3.2	Spin 1 . . . . .	52
2.4	Factorization and the Spectator Model . . . . .	56
2.4.1	Soft Amplitude Kinematics . . . . .	58
2.4.2	Hard Amplitude Kinematics . . . . .	60
<b>3</b>	<b>GPD Models</b>	<b>64</b>
3.1	Soft Helicity Amplitudes . . . . .	64
3.1.1	Quark Soft Amplitude Structure . . . . .	64
3.1.2	Gluon Soft Amplitude Structure . . . . .	66
3.1.3	Notes on Extra Kinematics . . . . .	68
3.2	$k^-$ Contour Integration . . . . .	69
3.3	Soft Amplitude Calculations . . . . .	72
3.3.1	Quark Soft Amplitudes . . . . .	72

3.3.2	Gluon Soft Amplitudes . . . . .	74
3.4	Hard Helicity Amplitudes . . . . .	76
3.4.1	Quark Hard Amplitudes LO . . . . .	77
3.4.2	NLO Quark and Gluon Hard Amplitudes . . . . .	79
3.5	Extra Kinematics . . . . .	84
3.6	Regge Term . . . . .	88
3.7	GPDs . . . . .	89
3.7.1	Parametrization . . . . .	93
3.8	ERBL and DGLAP ( $x < -\xi$ ) Regions . . . . .	94
<b>4</b>	<b>GPD Fit Results</b>	<b>98</b>
4.1	Fit Results . . . . .	98
4.2	Plots with $\zeta = 0, t = 0$ . . . . .	100
4.3	Distributions at the Initial Scale . . . . .	101
4.4	Distributions at $25 \text{ GeV}^2$ . . . . .	106
4.5	$Q^2$ Dependence . . . . .	114
4.6	Plots with $\zeta \neq 0, t \neq 0$ . . . . .	118
4.7	$t$ Dependence . . . . .	119
4.8	$\zeta > 0$ . . . . .	122
4.9	Predictions of the Polarized Gluon PDF . . . . .	128
4.10	Applications of GPDs . . . . .	130
<b>5</b>	<b>Applications and Outlook</b>	<b>131</b>
5.1	Applications of GPDs . . . . .	131

5.2	Electron-Proton and Positron-Proton Scattering . . . . .	132
5.2.1	Observables . . . . .	138
5.2.2	DVCS Observables . . . . .	141
5.2.3	Experimental Data and Observables . . . . .	146
5.3	Accessing the Gluon GPDs . . . . .	151
5.4	GPDs and Form Factors . . . . .	153
5.5	Impact Parameter Dependent Parton Distribution Functions .	153
5.6	Helicity-Flip Gluon GPDs . . . . .	155
5.7	Concluding Remarks and Outlook . . . . .	158
<b>A</b>	<b>Acronyms</b>	<b>161</b>
<b>B</b>	<b>GPD Parametrizations</b>	<b>163</b>
<b>C</b>	<b>Gordon Identities</b>	<b>173</b>
<b>D</b>	<b>QCD Evolution Equations</b>	<b>175</b>

Modeling the Structure of the Proton: Deeply Virtual  
Compton Scattering and Generalized Parton  
Distributions



# Chapter 1

## Introduction

### 1.1 Overview

The goal of this analysis is to expand upon the current understanding of the structure of the proton. Many of the proton's properties are already well established. These include properties of the proton as a whole, such as its mass or charge, as well as properties of the proton's internal structure. The internal structure of the proton is typically deciphered from various theoretical, mathematical objects and functions. Parton Distribution Functions (PDFs) describe the probability for partons within the proton - quarks, antiquarks, and gluons - to carry a certain fraction of the proton's forward momentum. Transverse-Momentum Distributions (TMDs) contain information about the transverse momentum of partons within the proton as well as their longitudinal momentum fractions. Form Factors contain information about the coupling of the proton with other objects, such as photons, as a function of the object's

squared four-momentum. Some properties of the proton's internal structure are still a mystery, and Generalized Parton Distributions (GPDs) can offer further insight once their models are completed.

GPDs offer many benefits over the previously established PDFs or TMDs, because they take into account more complexity. For example, the PDFs apply to processes with no net four-momentum transfer between the initial and final state hadrons, while GPDs can describe processes with a nonzero net four-momentum transfer. GPDs are useful for evaluating a variety of Compton scattering processes, including Deeply Virtual Compton Scattering (DVCS), while the PDFs are not as versatile. In addition, quark and gluon GPDs are connected to the quark and gluon PDFs. GPDs are also connected to various electromagnetic form factors. GPDs essentially provide all of the benefits of the PDFs and form factors, along with more benefits of their own.

The GPDs can also be used to explore the structure of the proton with respect to the two spatial dimensions that are transverse to the proton's direction of motion. The GPDs are associated with processes that can involve a net transverse momentum transfer between the initial and final state hadrons. They can be used to obtain impact parameter dependent PDFs, which contain information about the structure of the proton with respect to the spatial dimensions that are transverse to the proton's direction of motion. The impact parameter dependent PDFs for a particular parton type essentially describe how spread out the partons of that particular type are from the proton's transverse center of momentum, depending on the fraction of the proton's total

longitudinal momentum carried by the partons.

GPDs are also useful for evaluating the expectation values for the total angular momentum along the  $z$  direction carried by each parton type within a proton, for the case that the proton's spin is aligned along the positive  $z$  axis and the proton is moving very quickly in the positive  $z$  direction. Identical results are also obtained for the expectation values of light-cone helicity operators in place of the operators for angular momentum along the  $z$  direction. The results of these expectation values are independent of the magnitude of the proton's momentum, so long as the proton is at rest or travels in either the positive or negative  $z$  direction. It may also be possible to separate the spin content from the orbital angular momentum content for each parton type, though this subject is currently under discussion.

Overall, this analysis focuses on developing models for the sea quark and gluon GPDs. This analysis also identifies ways to access the GPDs experimentally, primarily through deeply virtual exclusive processes. Future studies can use information from this analysis to further develop models for the GPDs, evaluate the models with respect to experimental data, and interpret the results in order to ultimately gain a greater understanding of the internal structure of the proton.

## 1.2 The Parton Model

The standard model describes hadrons as composite particles, rather than pointlike. This thesis focuses on the structure of the proton in particular, although the methods used in the analysis could be applied to neutrons or other hadrons. One way to study the structure of the proton is to use a high energy probe in a process called Deep Inelastic Scattering (DIS). This section focuses on deep inelastic electron-proton scattering, in which an electron emits a high energy virtual photon that interacts with the proton, taking into account all possible hadronic final states. Other scattering processes, including neutrino-proton scattering, are also very important for the parton model, but they are not relevant to this analysis. There are many mathematical methods for modeling the proton's interaction with the photon, and they can be used to make predictions that can be compared to experimental results. The parton model takes the next step by introducing mathematical objects that model the partons that comprise the proton. The predictions from the parton model, when summing over each parton's contribution, should be identical to those from treating the proton as a single object. Finally, the parton model can be applied to Deeply Virtual Compton Scattering in order to obtain Generalized Parton Distribution functions, for the case where the incoming and outgoing hadrons do not necessarily have identical four-momentum.

### 1.2.1 Electron-Proton Scattering

The process of Deep Inelastic Scattering is ideal for probing the structure of the proton. This section will discuss deep inelastic electron-proton scattering. See figure 1.1 for a diagram of the inelastic electron-proton scattering process. The initial state electron with four-momentum  $k$  emits a photon with four-momentum  $q = k - k'$ , where  $k'$  is the four-momentum of the final state electron. The final hadronic state with total momentum  $p'$  is unobserved for inclusive scattering, and so the X indicates that all possible states are summed over. The proton-photon-hadron vertex is enlarged to indicate that the proton has a composite structure. The scattering amplitude is used to calculate a total, unpolarized cross section, and it is useful to separate the contributions to the amplitude from the leptons and the hadrons.

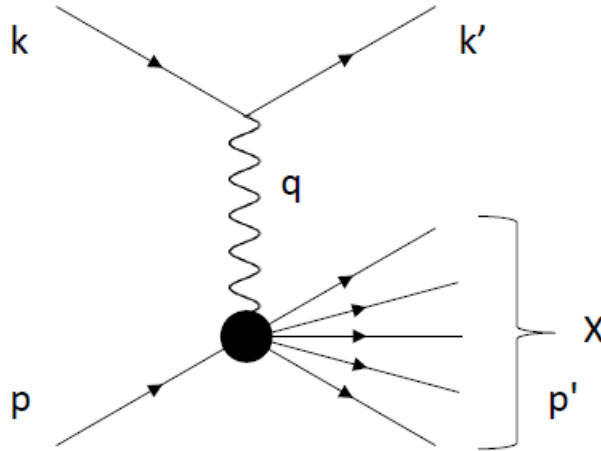


Figure 1.1: Inelastic electron-proton scattering, with one-photon exchange. The momentum labels are displayed for each object, and the X indicates a sum over hadronic final states.

It is also worthwhile to consider elastic electron-proton scattering with one-photon exchange. The elastic process is similar to the inelastic process, except that the final hadronic state is just a proton. See figure 1.2 for a diagram of the elastic electron-proton scattering process. As with inelastic scattering, the amplitude is used to calculate a total, unpolarized cross section, and again there is a distinction between the leptonic and hadronic contributions.

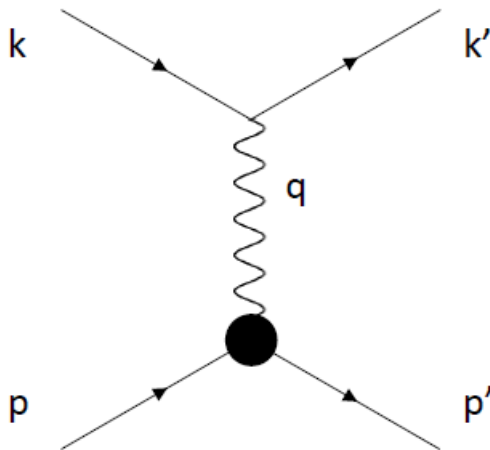


Figure 1.2: Elastic electron-proton scattering, with one-photon exchange. The momentum labels are displayed for each object.

In each case, the unpolarized lepton tensor is defined as

$$\begin{aligned}
 L^{\mu\nu} &= \frac{1}{2} \sum_{s,s'} \bar{u}(k', s') \gamma^\mu u(k, s) [\bar{u}(k', s') \gamma^\nu u(k, s)]^\dagger \\
 &= 2 \left[ k'^\mu k^\nu + k'^\nu k^\mu + \frac{q^2}{2} g^{\mu\nu} \right]
 \end{aligned} \tag{1.1}$$

where  $s$  and  $s'$  are the spin labels of the initial and final state electrons, respectively, and the electron masses are considered to be negligible. The lepton tensor is contracted with a hadron tensor in the process of calculating the cross section. The hadronic terms are a bit more complicated, and will be discussed in section 1.2.2

### 1.2.2 Form Factors and Structure Functions

The hadron tensor is evaluated in a similar way as the lepton tensor. The protons and hadronic final states are not pointlike, so their interactions are described by the proton current. In the case of elastic electron-proton scattering, the hadron tensor can be referred to as a 'proton tensor', and it is proportional to the following terms

$$B^{\mu\nu} \sim \sum_{r,r'} \langle p', r' | \hat{j}_{em,p}^{\mu}(0) | p, r \rangle \left( \langle p', r' | \hat{j}_{em,p}^{\nu}(0) | p, r \rangle \right)^* \quad (1.2)$$

where  $r$  and  $r'$  are the spin labels of the initial and final state protons, respectively. The spin states are summed over for unpolarized scattering.

The unpolarized hadron tensor for inelastic scattering is defined as

$$4\pi W^{\mu\nu} = \sum_X \langle p | \hat{j}_{em,p}^{\nu}(0) | X; p' \rangle \langle X; p' | \hat{j}_{em,p}^{\mu}(0) | p \rangle (2\pi)^4 \delta^{(4)}(p + q - p') \quad (1.3)$$

where the sum over final states,  $X$ , includes all possible quantum numbers for each hadronic state, as well as the phase space for each hadronic state with

restrictions so that the total momentum adds up to  $p'$ . Again, the spin states are summed over for unpolarized scattering.

The proton tensor for elastic scattering is best expanded directly in terms of the proton's current, using the relation  $q^2 = -Q^2$ . The current is expressed as

$$\begin{aligned} J_{em,p}^\mu(0) &\equiv \langle p', r' | \hat{j}_{em,p}^\mu(0) | p, r \rangle \\ &= (+e) \bar{u}(p', r') \left[ \gamma^\mu \mathcal{F}_1(Q^2) + \frac{i\kappa \mathcal{F}_2(Q^2)}{2M} \sigma^{\mu\nu} q_\nu \right] u(p, r) \end{aligned} \quad (1.4)$$

where  $\mathcal{F}_1$  and  $\mathcal{F}_2$  are the Dirac and Pauli Form Factors, normalized so that  $\mathcal{F}_1(0) = 1$  and  $\mathcal{F}_2(0) = 1$  for the proton.  $\kappa = 1.79$  is related to the proton's magnetic moment by  $\mu_p = 1 + \kappa$ ,  $e$  is the elementary charge, and  $M$  is the proton's mass. This expression follows the conventions of [37], but other conventions may vary. Because of current conservation, the expression satisfies the condition that  $q_\mu J_{em,p}^\mu(0) = 0$ . The cross section for elastic electron-proton scattering can be expressed in terms of these Form Factors, or alternatively in terms of the electric ( $G_E$ ) and magnetic ( $G_M$ ) Form Factors. Additionally, there is an axial vector proton current with axial ( $G_A$ ) and pseudoscalar ( $G_P$ ) form factors, which are more relevant for processes that distinguish polarization states. It will be shown later that the GPDs relate to some of these form factors without the need to calculate the full cross section.

The hadron tensor for the inelastic case is constructed to satisfy the Ward identity, such that  $q_\mu W^{\mu\nu} = q_\nu W^{\mu\nu} = 0$ , as well as symmetry properties. The



tensor is defined as

$$W^{\mu\nu} = W_1 \left( -g^{\mu\nu} - \frac{q^\mu q^\nu}{Q^2} \right) + \frac{W_2}{M^2} \left[ p^\mu + \frac{p \cdot q}{Q^2} q^\mu \right] \left[ p^\nu + \frac{p \cdot q}{Q^2} q^\nu \right] \quad (1.5)$$

with the conventional structure functions  $W_1$  and  $W_2$  for the symmetric tensor. Neutrino-proton scattering involves another structure function,  $W_3$ , as well as extra terms in the lepton tensor, all of which are not relevant to this analysis. The inclusive differential cross section is obtained in the laboratory frame, with the initial state target proton at rest, by the usual method. This differential cross section is given by

$$d\sigma^{(inelastic)} = \left( \frac{4\pi\alpha}{q^2} \right)^2 \frac{1}{4\sqrt{(k \cdot p)^2 - m^2 M^2}} 4\pi M L_{\mu\nu} W^{\mu\nu} \frac{d^3 k'}{2E_{k'} (2\pi)^3} \quad (1.6)$$

where  $\alpha$  is the fine structure constant, and  $m$  is the electron's mass which is considered small. In the laboratory frame, the outgoing electron travels at an angle  $\theta$  with respect to the initial state electron's momentum. The differential cross section can be expressed as

$$\frac{d^2\sigma^{(inelastic)}}{dQ^2 d\nu} = \frac{\pi\alpha^2}{4E_k^2 \sin^4(\frac{\theta}{2})} \frac{1}{E_k E_{k'}} \left[ W_2 \cos^2\left(\frac{\theta}{2}\right) + 2W_1 \sin^2\left(\frac{\theta}{2}\right) \right] \quad (1.7)$$

where  $\nu = E_k - E_{k'}$  is the photon's energy. A higher photon energy and a higher  $Q^2$  will allow the photon to probe further into the structure of the proton, and so Bjorken scaling will bring the scattering process into the limit of infinite photon energy.

### 1.2.3 Bjorken Scaling

Bjorken scaling takes the limit as  $Q^2$  and the photon energy  $\nu$  approach infinity while keeping their ratio finite. With  $\nu$  set in the laboratory frame,

$$Q^2 \rightarrow \infty, \quad \nu \rightarrow \infty$$
$$x = \frac{Q^2}{2p \cdot q} = \frac{Q^2}{2M\nu} \quad (1.8)$$

where  $x$  is the Bjorken variable  $x_{Bj}$ . The highly energetic probing photon can now resolve the partons within the proton, and so it can be treated as interacting with a single parton rather than the proton as a whole. The interacting parton can be treated as approximately having a fraction of the proton's total four-momentum and mass, such that for a parton of four-momentum  $p_i$  and mass  $m_i$

$$p_i^\mu \simeq f p^\mu, \quad m_i \simeq f M \quad (1.9)$$

and it can be shown that this fraction  $f$  is the same as the Bjorken variable  $x_{Bj}$ , if the struck parton remains on-shell. There is an alternative scheme where the parton instead carries a fraction of the proton's momentum along the lightcone, as described by [25]. The partons are treated as pointlike, and the differential cross section for electron-parton scattering with a parton of type  $i$  is expressed below. For now, the only partons considered are quarks

and antiquarks.

$$\frac{d^2\sigma^i}{dQ^2 d\nu} \stackrel{(eq, e\bar{q})}{=} \frac{\pi\alpha^2}{4E_k^2 \sin^4(\frac{\theta}{2})} \frac{1}{E_k E_{k'}} \left[ e_i^2 \cos^2\left(\frac{\theta}{2}\right) + e_i^2 \frac{Q^2}{4m_i^2} 2\sin^2\left(\frac{\theta}{2}\right) \right] \delta\left(\nu - \frac{Q^2}{2m_i}\right). \quad (1.10)$$

where  $e_i$  is the parton charge, in units of  $e$ . Equations 1.7 and 1.10 are compared to see how the structure functions from the hadron tensor compare to the individual parton terms. It is simple to identify the contributions from a given parton of type  $i$  to each structure function. A given parton's full contribution to  $W_1$  is obtained by first weighting the contributing term by the probability for that parton of type  $i$  to have a momentum fraction  $x$ , using the distribution  $f_i(x)$ . Next, the weighted term, which includes a Dirac  $\delta$ -function, is integrated over the full range of possible momentum fractions, with  $x$  ranging from 0 to 1. Finally, the results can be summed over every possible parton type to obtain the full expression for  $W_1$ , and the process is repeated for  $W_2$ . The final expressions for the structure functions in the Bjorken limit become

$$MW_1 = F_1(x) \quad (1.11)$$

$$\nu W_2 = \sum_i e_i^2 x f_i(x) \equiv F_2(x) \quad (1.12)$$

where the Callan-Gross relation gives

$$2xF_1(x) = F_2(x) \quad (1.13)$$

where  $F_1$  and  $F_2$  are functions of  $x$ , although they scale with  $Q^2$  as well. This leads to the parton model, which will be explained in more detail in section 1.2.4.

### 1.2.4 Parton Distribution Functions

The probability distributions  $f_i(x)$  in the previous section are identified as parton distribution functions. The Standard Model identifies six quark flavors along with their corresponding antiquarks. The quark distributions  $f_i(x) = q(x)$  for up, down, strange, charm, bottom, and top quarks respectively are

$$q(x) = u(x), d(x), s(x), c(x), b(x), t(x) \quad (1.14)$$

There is also a corresponding distribution for the antiquark of each flavor ( $\bar{q}(x) = \bar{u}(x), \bar{d}(x), \dots$ ). For each quark flavor, there is also a distinction between valence and sea quarks.

$$q(x) = q_V(x) + q_{sea}(x), \quad q_V(x) = q(x) - \bar{q}(x) \quad (1.15)$$

where it is assumed that

$$\bar{q}(x) = q_{sea}(x) \quad (1.16)$$

The up and down quark and antiquark distributions obey the following sum rules

$$\int_0^1 dx u_V(x) = 2 \quad (1.17)$$

$$\int_0^1 dx d_V(x) = 1 \quad (1.18)$$

in agreement with the basic model of two up valence quarks, or an excess of two up quarks over up antiquarks, and one down valence quark in the proton. The functions  $F_1$  and  $F_2$  have been defined for the proton in terms of parton distribution functions, but they can also be obtained for other nucleons such as neutrons by using isospin invariance. There is also a gluon parton distribution function,  $g(x)$ . The momentum sum rule for quarks using three flavors gives

$$\int_0^1 dx x [u(x) + \bar{u}(x) + d(x) + \bar{d}(x) + s(x) + \bar{s}(x)] = 1 - \epsilon \quad (1.19)$$

where  $\epsilon$  is the fraction of the proton's momentum carried by other partons.

The PDFs discussed so far do not distinguish the spin states for the partons. For each parton type, it is possible to define two new distributions that separate the spin states. For any given quark flavor  $q$ , the distribution  $q^\uparrow(x)$  represents the probability that the quark spin is parallel to the proton's spin, while the distribution  $q^\downarrow(x)$  represents the probability that the quark spin is antiparallel to the proton's spin. The unpolarized PDF is given by  $q(x) = q^\uparrow(x) + q^\downarrow(x)$ , while the polarized PDF is given by  $\Delta q(x) = q^\uparrow(x) - q^\downarrow(x)$ . There are also

polarized PDFs for antiquarks and gluons, along with their corresponding unpolarized PDFs.

## 1.3 Generalized Parton Distributions

The hadron tensor and parton distribution functions are well understood for DIS. The PDFs have limited applications because they only take the parton's momentum fraction along the lightcone into consideration. They are not capable of describing partons with transverse momentum, for example. Other functions, such as transverse-momentum distributions [5] and Generalized Parton Distribution functions add more complexity by including extra kinematics compared to the PDFs. This analysis focuses on GPDs and their applications. The leading forms of the GPDs are obtained by the handbag model, which will be explained in the following sections.

### 1.3.1 Forward Scattering Amplitude

The squared amplitude for inelastic electron-proton scattering can be compared to the imaginary part of the forward amplitude of the process ( $e + P \rightarrow e + P$ ) with two-photon exchange and a sum over all intermediate hadronic states. The hadron tensor and the PDFs are associated with the hadronic part of this forward scattering amplitude. Of course, this only applies in the forward limit, when the initial state proton and final state proton have the same momentum. See figure 1.3 for a diagram of the forward scattering amplitude,

with separate hadronic and leptonic contributions.

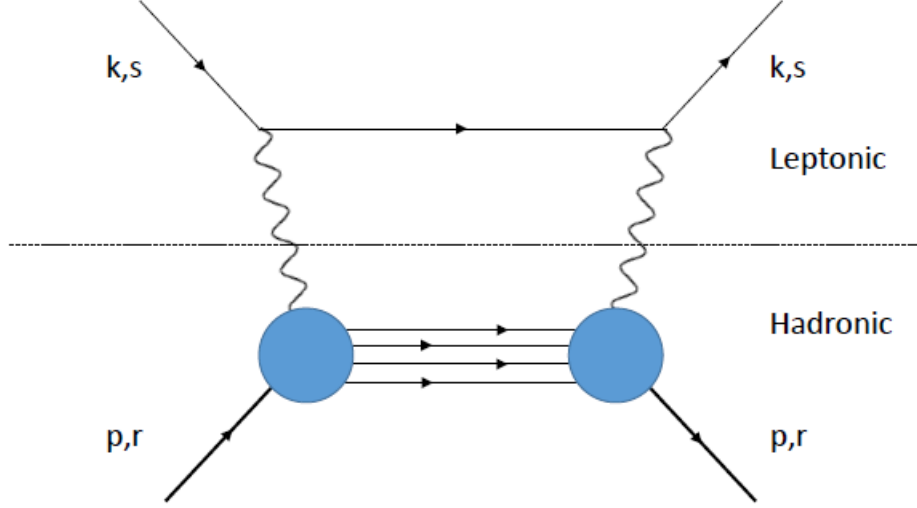


Figure 1.3: Forward scattering amplitude for the process  $(e + P \rightarrow e + P)$  with two-photon exchange, with momentum and spin labels. The intermediate hadronic state in the diagram represents a sum over the full set of possible states.

The hadronic contribution is independent of the leptonic interactions with the photons. In order to model the structure of the proton, it is useful to isolate the hadronic interactions. In this case, the proton absorbs a photon and emits another photon. This Compton scattering process lends insight into the structure of the proton as well as the relevance of the PDFs, and has a direct conceptual link to DIS. The proton's structure can also be modeled with more complexity by examining other types of hadronic interactions, although this requires overall processes other than DIS.

The most relevant hadronic interaction for this analysis is Deeply Virtual Compton Scattering. It involves the proton absorbing a virtual photon and

emitting a real photon. The incoming virtual photon may have been emitted from an electron, for example, in an electron-proton scattering process. In any case, it is sufficient to isolate the hadronic interaction in order to model the proton's structure. It is not important to model how the virtual photon was produced in the first place. DVCS introduces a momentum transfer between the initial and final state hadrons. In the forward limit, when there is no net momentum transfer, then the process is no longer DVCS, but rather the Compton scattering process described earlier in connection to DIS. The inclusion of a momentum transfer makes DVCS ideal for modeling the GPDs. The remaining sections will show how the hadron tensor is expanded to introduce a partonic interpretation of DVCS.

It should be noted that there are other hadronic interactions relevant to the GPDs. These include Deeply Virtual Meson Production (DVMP) [31], weak interactions, Time-like Compton Scattering (TCS), and Doubly Virtual Compton Scattering [6]. Depending on which GPDs are being modeled, some hadronic interactions may be more suitable than others. For example, see [36] for a discussion of exclusive  $\pi^0$  electroproduction. DVCS is ideal for this analysis, and so the other interactions will not be discussed.



### 1.3.2 Current Expansion

The hadronic tensor for DVCS can be expressed as [11]

$$T^{\mu\nu} = i \int d^4z e^{i\frac{(q+q')^\alpha}{2}z_\alpha} \langle p' | T \hat{j}_{em,p}^\mu \left( -\frac{z}{2} \right) \hat{j}_{em,p}^\nu \left( \frac{z}{2} \right) | p \rangle \quad (1.20)$$

where  $q$  and  $q'$  are the four-momentum labels of the incoming and outgoing photons respectively. The  $_{(em,p)}$  labels are taken to be implicit from now on. The currents can then be expanded in terms of spin- $\frac{1}{2}$  field operators. The current can be expanded using the following convention

$$\hat{j}^\mu(\xi) = \bar{\psi}(\xi) \gamma^\mu \psi(\xi) \quad (1.21)$$

$$= \sum_q e_q \bar{\psi}_q(\xi) \gamma^\mu \psi_q(\xi) \quad (1.22)$$

where the sum is over quark fields of flavor  $q = u, d, s, \dots$  with charges  $e_q$ . The fermions associated with the fields are assumed to be massless. The time ordered product of currents can be expanded in terms of the fermion fields in the following way

$$T \hat{j}^\mu \left( -\frac{z}{2} \right) \hat{j}^\nu \left( \frac{z}{2} \right) = i \bar{\psi} \left( -\frac{z}{2} \right) \gamma^\mu S(-z) \gamma^\nu \psi \left( \frac{z}{2} \right) + i \bar{\psi} \left( \frac{z}{2} \right) \gamma^\nu S(z) \gamma^\mu \psi \left( -\frac{z}{2} \right) \quad (1.23)$$

where  $S(z)$  is the free quark propagator in coordinate-space [6]

$$S(z) = \frac{\not{z}}{2\pi^2 z^4} \quad (1.24)$$

By using a few relations with the gamma matrices, the following expression is obtained for the time ordered product.

$$\begin{aligned}
iT\hat{j}^\mu\left(-\frac{z}{2}\right)\hat{j}^\nu\left(\frac{z}{2}\right) &= \sum_q e_q^2 \frac{z_\rho}{2\pi^2 z^4} \left( s^{\mu\rho\nu\sigma} \left[ \bar{\psi}_q\left(-\frac{z}{2}\right) \gamma_\sigma \psi_q\left(\frac{z}{2}\right) - \{z \rightarrow -z\} \right] \right. \\
&\quad \left. - i\epsilon^{\mu\rho\nu\sigma} \left[ \bar{\psi}_q\left(-\frac{z}{2}\right) \gamma_\sigma \gamma_5 \psi_q\left(\frac{z}{2}\right) + \{z \rightarrow -z\} \right] \right) + O(z^{-2})
\end{aligned} \tag{1.25}$$

up to higher-order corrections. The rank 4 tensor  $s$  is defined as

$$s^{\mu\rho\nu\sigma} = g^{\mu\rho} g^{\nu\sigma} + g^{\mu\sigma} g^{\nu\rho} - g^{\mu\nu} g^{\rho\sigma} \tag{1.26}$$

The antisymmetric tensor  $\epsilon^{\mu\rho\nu\sigma}$  uses the convention  $\epsilon_{0123} = 1$ . Even permutations of these indices give the same value, while odd permutations reverse the sign.  $\epsilon^{\mu\rho\nu\sigma} = 0$  if at least two indices have the same value.

It is straightforward to show that for DIS in the Bjorken limit, the hadron tensor is dominated by interactions on the light cone. That is, in terms of light cone coordinates,  $(z^+, z^-, \mathbf{z}_\perp)$ , the dominant contribution with  $q^- \rightarrow \infty$  comes from  $z^+ \rightarrow 0, z_\perp \rightarrow 0$ , and  $z^2 \rightarrow 0$  with finite  $z^-$  [18]. For DVCS, the incoming virtual photon is far off shell, with  $Q^2 \rightarrow \infty$ , and the outgoing photon is on shell. The average momentum of the incoming and outgoing photons is defined as  $\bar{q} = \frac{(q+q')}{2}$ , and  $\Delta = P - P'$  is the momentum transfer between the initial and final state hadrons.  $\bar{Q}^2 \rightarrow \infty$  as well in the limit that  $|\Delta^2|$  is small compared to  $Q^2$ , with the outgoing photon on shell. The light cone dominance for DIS is assumed to be true for DVCS as well, for the

case that  $|\Delta^2|$  is small compared to  $Q^2$ . There is another constraint that the transverse momentum magnitudes are small, so that the interactions between the photons and protons take place approximately along the light cone with very small  $z_\perp \simeq 0$ . The DVCS amplitude is dominated by interactions along the light cone, and the leading terms of the time ordered current expansion for the Compton amplitude provide the basis for the handbag model, which will be discussed in section 1.3.3.

The expansion of the Compton amplitude also contains Wilson line expressions of the form  $W[\pm\frac{z}{2}, \mp\frac{z}{2}]$ . The quark and gluon fields at two different points,  $a$  and  $b$ , won't necessarily be comparable without a Wilson line, because the local gauges at the two points might have different phases. The Wilson line  $W[a, b]$  provides a connection between the local gauges at the two points, and allows the fields at points  $a$  and  $b$  to be compared. When only  $z^-$  is nonzero, at leading twist, a term that will be defined later, the Wilson line expressions reduce to

$$\begin{aligned} W\left[\pm\frac{z}{2}, \mp\frac{z}{2}\right] &= \mathcal{P}e^{ig\int_{\mp\frac{z}{2}}^{\pm\frac{z}{2}} dx^\mu A_\mu} \\ &\rightarrow \mathcal{P}e^{ig\int_{\mp\frac{1}{2}z^-}^{\pm\frac{1}{2}z^-} dx^- A^+} \end{aligned} \quad (1.27)$$

where  $\mathcal{P}$  denotes ordering along the path from  $\pm\frac{z}{2}$  to  $\mp\frac{z}{2}$ , and both  $A_\mu$  and  $A^+$  are functions of position. In the  $A^+ = 0$  gauge, the Wilson line expressions reduce to 1 at leading twist. They have additional terms that contribute at higher twist and different gauges.

### 1.3.3 Handbag Model

The expansion of the Compton amplitude in terms of quark fields has a useful partonic interpretation called the handbag model. One leading term for the quark fields describes a process where a quark from within the initial hadron interacts with both photons and then returns to form the final state hadron, but other interactions are possible as well depending on the kinematics of the scattering objects. For example, the photons may interact with an antiquark instead, or a combination of a quark and an antiquark. The factorized handbag diagrams for the leading-order amplitudes involving a quark are shown in figure 1.4. The handbag model will use new momentum and helicity labels as follows:  $(P, \Lambda)$  and  $(P', \Lambda')$  for the initial and final state hadrons,  $(k, \lambda)$  and  $(k', \lambda')$  for the initial and final partons or antipartons, and finally  $(q, \Lambda_\gamma)$  and  $(q', \Lambda'_\gamma)$  for the incoming and outgoing photons respectively.

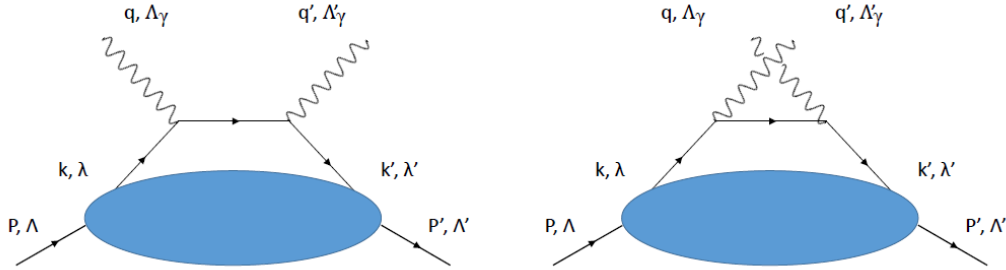


Figure 1.4: Handbag diagrams for DVCS involving a quark interacting with both photons.

The hard and soft subprocesses both correspond to terms in the Compton amplitude, after expanding the product of currents. After transforming to momentum space in terms of  $\bar{k} = \frac{k+k'}{2}$ , the matrix elements in connection

with the soft subprocesses are defined as

$$F^{q\mu} = \bar{P}^+ \int \frac{dz^-}{2\pi} e^{ix\bar{P}^+z^-} \langle P' | \bar{\psi}_q \left( -\frac{z}{2} \right) \gamma^\mu \psi_q \left( \frac{z}{2} \right) | P \rangle \Big|_{z^+=0, \mathbf{z}_\perp=0} \quad (1.28)$$

$$\tilde{F}^{q\mu} = \bar{P}^+ \int \frac{dz^-}{2\pi} e^{ix\bar{P}^+z^-} \langle P' | \bar{\psi}_q \left( -\frac{z}{2} \right) \gamma^\mu \gamma_5 \psi_q \left( \frac{z}{2} \right) | P \rangle \Big|_{z^+=0, \mathbf{z}_\perp=0} \quad (1.29)$$

where  $\bar{P} = \frac{P+P'}{2}$  is the average four-momentum of the initial and final state hadrons,  $\bar{k}^+ \equiv x\bar{P}^+$ , and  $q = u, d, s \dots$  indicates the quark flavor.

Each matrix element can be further expanded in terms of twist. The geometric twist is defined as  $\tau = d - s$ , where  $s$  is the Lorentz spin of the operator and  $d$  is the dimension in mass units. Effectively, twist can be thought of as a way to classify terms based on the order of their suppression by  $Q$ . Contributions from higher twist terms typically are suppressed by larger powers of  $\frac{1}{Q}$ . Jaffe introduces another definition for the twist of the invariant matrix elements, such as the ones used in this analysis. His definition of twist [17] classifies the order in  $\frac{M}{Q}$  at which an operator matrix element contributes to processes, where  $M$  is the proton's mass for DIS or, by extension, DVCS. Terms of twist- $t$  are suppressed by factors of  $(\frac{M}{Q})^{t-2}$ , though each term can have contributions with higher suppression as well. Twist-2 terms have no suppression in their leading contributions.

For this analysis, the matrix elements are expressed in a frame with the initial state proton moving very fast in the  $+\hat{z}$  direction, with a very large

four-momentum component  $P^+$ . The light cone vectors are defined as

$$p^\mu = \frac{1}{\sqrt{2}}(1, 0, 0, 1), \quad n^\mu = \frac{1}{\sqrt{2}}(1, 0, 0, -1) \quad (1.30)$$

The matrix elements in equations 1.28-1.29 can be expanded into components in terms of the light-cone vectors, and each component may have a different twist. The leading twist terms pertaining to the chiral-even GPDs are obtained by contracting  $F^{q\mu}$  or  $\tilde{F}^{q\mu}$  with  $n_\mu$ . Chiral-even GPDs are related to interactions where the chirality of the interacting partons is conserved. After reshuffling terms in the Compton amplitude, the generalized quark distributions that provide the basis for the leading twist chiral-even GPDs are defined as

$$F^q = \frac{1}{2} \int \frac{dz^-}{2\pi} e^{ix\bar{P}^+z^-} \langle P' | \bar{\psi}_q \left( -\frac{z}{2} \right) \gamma^+ \psi_q \left( \frac{z}{2} \right) | P \rangle \Big|_{z^+=0, \mathbf{z}_\perp=0} \quad (1.31)$$

$$\tilde{F}^q = \frac{1}{2} \int \frac{dz^-}{2\pi} e^{ix\bar{P}^+z^-} \langle P' | \bar{\psi}_q \left( -\frac{z}{2} \right) \gamma^+ \gamma_5 \psi_q \left( \frac{z}{2} \right) | P \rangle \Big|_{z^+=0, \mathbf{z}_\perp=0} \quad (1.32)$$

The generalized quark distributions are useful for interpreting the soft subprocesses of the handbag diagrams. They relate to subprocesses that involve initial and final state hadrons, and the quarks and antiquarks that will be contributing to the hard subprocesses. They provide the basis for a partonic interpretation that will further expand on the soft subprocesses in terms of helicity states. In addition to the generalized quark distributions, there are gluon distributions that relate to soft subprocesses involving initial and final

state hadrons, with gluons contributing to the hard subprocesses rather than quarks and antiquarks.

The gluon distributions can be derived from a correlator expressed as

$$\Gamma^{\alpha\mu;\beta\nu} = \int \frac{d^4z}{(2\pi)^4} e^{i\bar{k}^\rho z_\rho} \langle P' | G^{\alpha\mu} \left( -\frac{z}{2} \right) \mathcal{U} \left( -\frac{z}{2}, \frac{z}{2} \right) G^{\beta\nu} \left( \frac{z}{2} \right) | P \rangle \quad (1.33)$$

where  $G^{\mu\nu}(x)$  is the gluon field strength tensor, and  $\mathcal{U}(-\frac{z}{2}, \frac{z}{2})$  is a gauge link. This gauge link will be omitted from now on, because it reduces to 1 for the leading twist GPDs for this analysis with the chosen gauge of  $A^+ = 0$ . After transforming to momentum space in terms of  $\bar{k}$ , the leading twist terms are extracted by contracting the appropriate indices in the field strength tensors with the appropriate light cone vectors. Using the resulting expressions, the gluon distributions can be defined as

$$F^g = \frac{1}{\bar{P}^+} \int \frac{dz^-}{2\pi} e^{ix\bar{P}^+z^-} \langle P' | G^{+\mu} \left( -\frac{z}{2} \right) G_\mu^+ \left( \frac{z}{2} \right) | P \rangle \Big|_{z^+=0, \mathbf{z}_\perp=0} \quad (1.34)$$

$$\tilde{F}^g = -\frac{i}{\bar{P}^+} \int \frac{dz^-}{2\pi} e^{ix\bar{P}^+z^-} \langle P' | G^{+\mu} \left( -\frac{z}{2} \right) \tilde{G}_\mu^+ \left( \frac{z}{2} \right) | P \rangle \Big|_{z^+=0, \mathbf{z}_\perp=0} \quad (1.35)$$

where the dual field strength tensor is

$$\tilde{G}^{\alpha\beta}(x) = \frac{1}{2} \epsilon^{\alpha\beta\gamma\delta} G_{\gamma\delta}(x) \quad (1.36)$$

Finally, the quark and gluon distributions are expanded into vector and axial vector terms of varying twist to obtain the GPDs. This concept is similar to

expanding the electromagnetic current in terms of Form Factors. The helicity conserving GPDs at leading twist are presented in section 1.3.4. The partonic interpretation of the quark and gluon distributions will be discussed later in section 1.4.

### 1.3.4 Helicity Conserving GPDs

The twist-2 quark distributions expand in the following way in terms of chiral-even GPDs [2]

$$F^q = \frac{1}{2\bar{P}^+} \left[ H^q(x, \xi, t) \bar{u}(P') \gamma^+ u(P) + E^q(x, \xi, t) \bar{u}(P') \frac{i\sigma^{+\alpha}(-\Delta_\alpha)}{2M} u(P) \right] \quad (1.37)$$

$$\tilde{F}^q = \frac{1}{2\bar{P}^+} \left[ \tilde{H}^q(x, \xi, t) \bar{u}(P') \gamma^+ \gamma_5 u(P) + \tilde{E}^q(x, \xi, t) \bar{u}(P') \frac{\gamma_5(-\Delta^+)}{2M} u(P) \right] \quad (1.38)$$

where ... denotes contributions of higher twist that are not considered in this analysis. Similarly, the gluon distributions expand in the following way, keeping only the leading twist terms relevant to this analysis

$$F^g = \frac{1}{2\bar{P}^+} \left[ H^g(x, \xi, t) \bar{u}(P') \gamma^+ u(P) + E^g(x, \xi, t) \bar{u}(P') \frac{i\sigma^{+\alpha}(-\Delta_\alpha)}{2M} u(P) \right] \quad (1.39)$$

$$\tilde{F}^g = \frac{1}{2\bar{P}^+} \left[ \tilde{H}^g(x, \xi, t) \bar{u}(P') \gamma^+ \gamma_5 u(P) + \tilde{E}^g(x, \xi, t) \bar{u}(P') \frac{\gamma_5(-\Delta^+)}{2M} u(P) \right] \quad (1.40)$$

The variable  $x$ , as defined earlier, is the fraction of the plus momentum  $\bar{P}^+$  carried by  $\bar{k}^+$ . The skewness variable  $\xi$  relates the plus component of the momentum transfer between the initial and final state hadrons to  $\bar{P}^+$ , and so



a nonzero value indicates that the plus momentum components of the initial and final state hadrons are different. The variable  $t$  is the invariant momentum transfer  $(P - P')^2$ .

$$x = \frac{\bar{k}^+}{\bar{P}^+}, \quad \xi = \frac{P^+ - P'^+}{2\bar{P}^+}, \quad t = \Delta^2 \quad (1.41)$$

At leading twist, there are four helicity conserving GPDs for transversely polarized gluons and four chiral-even GPDs for each quark flavor. For any particular quark flavor or for gluons, these four GPDs are labeled as  $H(x, \xi, t)$ ,  $E(x, \xi, t)$ ,  $\tilde{H}(x, \xi, t)$ , and  $\tilde{E}(x, \xi, t)$ . Ordinarily a label of  $(q = u, d, s...)$  indicates the quark flavor or a label of  $g$  indicates that the partons are gluons, but these labels have been omitted here. The GPDs each play an important role in the Light-Cone Helicity amplitudes, which will be discussed in section 1.4 in more detail.

At leading twist, there are also four helicity-flip GPDs for transversely polarized gluons and four chiral-odd GPDs for each quark flavor. For any particular quark flavor or for gluons, these four GPDs are given by  $H_T(x, \xi, t)$ ,  $E_T(x, \xi, t)$ ,  $\tilde{H}_T(x, \xi, t)$ , and  $\tilde{E}_T(x, \xi, t)$ . The labels of  $(q = u, d, s...)$  and  $g$  are again omitted. These helicity-flip or chiral-odd GPDs are important for giving a full account of the combinations of parton helicity states, but they are not relevant for this analysis. The remainder of this discussion will focus primarily on the helicity conserving or chiral-even GPDs.

## 1.4 Partonic Interpretation and Light-Cone Helicity

The generalized quark and gluon distributions defined in section 1.3.3 have a partonic interpretation that is helpful for understanding the role of the GPDs. The distributions are expressed in terms of on mass shell partons, by using the framework of light-cone quantization. The partons can then be assigned helicities, and the soft subprocesses are evaluated in terms of light-cone helicity (LC helicity) amplitudes. The GPDs can be evaluated using different combinations of LC helicity amplitudes, and so the connection of each GPD to the LC helicity states of the partons and hadrons becomes more apparent. For any four-vector  $V$  given by  $(V^0, V^1, V^2, V^3)$ , the LC  $\pm$  components are defined as  $V^\pm = \frac{1}{\sqrt{2}}(V^0 \pm V^3)$  for this discussion.

### 1.4.1 Light-Cone Quantization

In the framework of light-cone quantization, the quark and gluon fields are expanded at a light-cone time of  $z^+ = 0$ , in the  $A^+ = 0$  gauge for the gluon fields. The quark fields are projected into a "good" and a "bad" component using the projection operator:

$$P_\pm = \frac{1}{2}\gamma^\mp\gamma^\pm \tag{1.42}$$

$$\psi_{q+} = P_+\psi_q, \quad \psi_{q-} = P_-\psi_q \tag{1.43}$$

The "bad" field components  $\psi_{q-}$  are dynamically dependent on the "good" field components  $\psi_{q+} \equiv \phi_q$ , and so canonical anticommutation relations for free fields are imposed on the dynamically independent "good" fields. For gluon fields, the "bad" field component  $A^-$  is dynamically dependent in the condition that  $A^+ = 0$ . The commutation relations for free fields are imposed on the "good" components of the gluon fields, which are the transverse components  $A^i$  for  $i = 1, 2$ .

The quark field Fourier decomposition in terms of creation and annihilation operators is

$$\begin{aligned} \phi(z) \Big|_{z^+=0} &= \int \frac{d^2 k_\perp dk^+}{16\pi^3 k^+} \theta(k^+) \\ &\sum_\lambda \left[ b(k^+, \mathbf{k}_\perp, \lambda) u_+(k^+, \lambda) e^{-i(k^\alpha z_\alpha)} + d^\dagger(k^+, \mathbf{k}_\perp, \lambda) v_+(k^+, \lambda) e^{i(k^\alpha z_\alpha)} \right] \Big|_{z^+=0} \end{aligned}$$

where the color fields have been omitted from the expression. The index  $\lambda = \pm \frac{1}{2}$  denotes the LC helicity of the parton, and the "good" components of the spinors are projected as  $u_+ = P_+ u$  for quarks and  $v_+ = P_+ v$  for antiquarks. Calculations for fermions with LC helicity can use the LC helicity spinor convention presented by Diehl [11]. It can be shown that calculations with LC helicity give approximately the same results as calculations with ordinary helicity for particles moving fast in the  $+\hat{z}$  direction. Using the same convention as Diehl for a particle of four-momentum  $p$ , mass  $m$ , and LC helicity  $\lambda = \pm \frac{1}{2}$

denoted by  $(\pm)$ , the LC helicity spinors are

$$\begin{aligned}
u_{LC}(p, +) &= \frac{1}{\sqrt{2(p^0 + p^3)}} \begin{pmatrix} p^0 + p^3 + m \\ p^1 + ip^2 \\ p^0 + p^3 - m \\ p^1 + ip^2 \end{pmatrix}, & u_{LC}(p, -) &= \frac{1}{\sqrt{2(p^0 + p^3)}} \begin{pmatrix} -p^1 + ip^2 \\ p^0 + p^3 + m \\ p^1 - ip^2 \\ -p^0 - p^3 + m \end{pmatrix}, \\
v_{LC}(p, +) &= \frac{-1}{\sqrt{2(p^0 + p^3)}} \begin{pmatrix} -p^1 + ip^2 \\ p^0 + p^3 - m \\ p^1 - ip^2 \\ -p^0 - p^3 - m \end{pmatrix}, & v_{LC}(p, -) &= \frac{-1}{\sqrt{2(p^0 + p^3)}} \begin{pmatrix} p^0 + p^3 - m \\ p^1 + ip^2 \\ p^0 + p^3 + m \\ p^1 + ip^2 \end{pmatrix}
\end{aligned} \tag{1.44}$$

The Fourier decomposition of the "good" gluon field components in terms of creation and annihilation operators is given by

$$\begin{aligned}
A^i(z) \Big|_{z^+=0} &= \int \frac{d^2 k_\perp dk^+}{16\pi^3 k^+} \theta(k^+) \\
&\sum_\lambda \left[ a(k^+, \mathbf{k}_\perp, \lambda) \epsilon^i(\lambda) e^{-i(k^\alpha z_\alpha)} + a^\dagger(k^+, \mathbf{k}_\perp, \lambda) \epsilon^{i*}(\lambda) e^{i(k^\alpha z_\alpha)} \right] \Big|_{z^+=0}
\end{aligned}$$

where the transverse index  $i = 1, 2$ , and the color fields have again been omitted from the expression. The polarization vectors, also labeled as  $\epsilon(\pm)$ , are for states with LC helicity  $\lambda = \pm 1$ . In terms of the transverse indices, the

vectors are given by

$$\epsilon(+)=\frac{-1}{\sqrt{2}}\begin{pmatrix}1\\i\end{pmatrix},\quad\epsilon(-)=\frac{1}{\sqrt{2}}\begin{pmatrix}1\\-i\end{pmatrix}\quad(1.45)$$

The creation and annihilation operators obey the following anticommutation and commutation relations [9], where the labels  $(k^+, \mathbf{k}_\perp, \lambda)$  along with the color index  $c$  are represented by the single label  $(w)$  that contains all of that information.

$$\{b_{q'}(w'), b_q^\dagger(w)\} = \{d_{q'}(w'), d_q^\dagger(w)\} = 16\pi^3 k^+ \delta(k'^+ - k^+) \delta^{(2)}(\mathbf{k}'_\perp - \mathbf{k}_\perp) \delta_{q'q} \delta_{\lambda'\lambda} \delta_{c'c} \quad(1.46)$$

$$[a(w'), a^\dagger(w)] = 16\pi^3 k^+ \delta(k'^+ - k^+) \delta^{(2)}(\mathbf{k}'_\perp - \mathbf{k}_\perp) \delta_{\lambda'\lambda} \delta_{c'c} \quad(1.47)$$

The eigenstate for a single quark with a particular momentum, helicity, and color is formed by the creation operator  $b^\dagger$  acting on the perturbative vacuum, and similarly for antiquarks with  $d^\dagger$  and gluons with  $a^\dagger$ .

### 1.4.2 Partonic Interpretation

The generalized quark and gluon distributions in section 1.3.3 take a distinct partonic interpretation when the "good" components of the fields are expanded in terms of creation and annihilation operators, using relations from section 1.4.1. For each of the generalized quark distributions, the expanded product of fields results in many terms before integration. Each unintegrated term

is proportional to a pair of operators between initial and final proton states, using  $\langle P'|b^\dagger(w')b(w)|P\rangle$  as an example. This means that each term contributes to a corresponding process. The term in the example given contributes to the amplitude for which the initial state hadron emits a quark with momentum  $k$  and absorbs a quark with momentum  $k'$  to form the final state hadron, where each quark also has its appropriate color charge and LC helicity according to the creation and annihilation operators. Other combinations of creation and annihilation operators contribute to different processes, such as the initial hadron emitting an antiquark and a quark.

Each term is also restricted to a specific kinematic region after integrating over a few variables. For example, in the expansion of the generalized quark distribution  $F^q$ , the values for  $k^+$  and  $k'^+$  are restricted in two ways. First, each unintegrated term is proportional to the product  $\theta(k^+)\theta(k'^+)$ , and so integration eliminates the terms for which either momentum component is negative. Second, after a series of integrations, the momentum components of any given term are restricted by the following condition:

$$x = \frac{s_k k^+ + s_{k'} k'^+}{2\bar{P}^+} \quad (1.48)$$

where, depending on the term, the signs take one of four combinations of  $s_k = \pm 1$  and  $s_{k'} = \pm 1$ .

As a result, each term can only give nonzero contributions to a particular region of  $x$  and  $\xi$ . The region of interest for this analysis is the DGLAP

(Dokshitzer, Gribov, Lipatov, Altarelli, Parisi) region [3] with  $x > \xi$ . The skewness  $\xi$  is set to be positive when nonzero, and the GPDs with  $-\xi$  can be solved afterwards using properties resulting from time reversal invariance. In this region, under these conditions, the outgoing parton will have a positive LC + momentum component  $(x + \xi)\bar{P}^+$ , and the incoming parton will have a positive LC + momentum component  $(x - \xi)\bar{P}^+$ . These momentum components can be zero as well if the condition  $x = \xi$  is included, but they will not be negative. In other words, the LC + momentum components of the outgoing parton, the incoming parton, and the total momentum transfer from the photon interactions are restricted such that the LC + momentum components for the partons will not be negative.

In this DGLAP region, the soft subprocesses for the quark distributions involve the initial hadron emitting a quark and absorbing a quark to form the final state hadron, and the soft subprocesses for the gluon distributions involve the initial state hadron emitting a gluon and absorbing a gluon to form the final state hadron. The soft subprocesses take different partonic interpretations in the kinematic regions with  $x < \xi$ . For example, when  $-\xi < x < \xi$ , the soft subprocesses for the quark distributions involve an interacting quark and an interacting antiquark. The subprocesses in the DGLAP region with  $x > \xi$  will be modeled by LC helicity amplitudes in section 1.4.3, and the connection between these amplitudes and the GPDs will be discussed. See [3] and [9] for more detailed discussions.

### 1.4.3 LC Helicity Amplitudes

The LC helicity amplitudes for the DGLAP region with  $x \in [\xi, 1]$  are constructed by considering the soft subprocesses described in section 1.4.2, where the initial state hadron emits a quark and absorbs a quark, or emits a gluon and absorbs a gluon. The protons, quarks, and gluons have the usual momentum and helicity labels defined in section 1.3.3, but the helicity labels in this section, 1.4.3, represent LC helicity states rather than ordinary helicity. The LC helicity amplitudes are expressed as the matrix elements

$$A_{\Lambda'\lambda',\Lambda\lambda}^{(LC)q} = \int \frac{dz^-}{2\pi} e^{ix\bar{P}^+z^-} \langle P', \Lambda' | \mathcal{O}_{\lambda'\lambda}^q(z) | P, \Lambda \rangle \Big|_{z^+=0, \mathbf{z}_\perp=0} \quad (1.49)$$

$$A_{\Lambda'\lambda',\Lambda\lambda}^{(LC)g} = \frac{1}{\bar{P}^+} \int \frac{dz^-}{2\pi} e^{ix\bar{P}^+z^-} \langle P', \Lambda' | \mathcal{O}_{\lambda'\lambda}^g(z) | P, \Lambda \rangle \Big|_{z^+=0, \mathbf{z}_\perp=0} \quad (1.50)$$

where the operators  $\mathcal{O}_{\lambda'\lambda}^{q,g}$  are constructed in a way that projects the LC helicity states of the emitted and absorbed partons. The LC helicity conserving operators are given by

$$\mathcal{O}_{++}^q = \frac{1}{4} \bar{\psi}_q \gamma^+ (1 + \gamma_5) \psi_q \quad (1.51)$$

$$\mathcal{O}_{--}^q = \frac{1}{4} \bar{\psi}_q \gamma^+ (1 - \gamma_5) \psi_q \quad (1.52)$$

$$\mathcal{O}_{++}^g = \frac{1}{2} [G^{+\alpha} G_\alpha^+ - i G^{+\alpha} \tilde{G}_\alpha^+] \quad (1.53)$$

$$\mathcal{O}_{--}^g = \frac{1}{2} [G^{+\alpha} G_\alpha^+ + i G^{+\alpha} \tilde{G}_\alpha^+] \quad (1.54)$$



The corresponding LC helicity flipping operators are not considered in this analysis. Expressions for the LC helicity flipping operators can be found in [11].

The LC helicity amplitudes are compared to the generalized quark and gluon distributions by direct substitution. For either quarks or gluons

$$F_{\Lambda,\Lambda'}^{(LC)} = A_{\Lambda'+,\Lambda+}^{(LC)} + A_{\Lambda'-,\Lambda-}^{(LC)} \quad (1.55)$$

$$\tilde{F}_{\Lambda,\Lambda'}^{(LC)} = A_{\Lambda'+,\Lambda+}^{(LC)} - A_{\Lambda'-,\Lambda-}^{(LC)} \quad (1.56)$$

where the matrix elements  $F_{\Lambda,\Lambda'}^{(LC)}$  and  $\tilde{F}_{\Lambda,\Lambda'}^{(LC)}$  are the expressions from equations 1.31 and 1.32 for quarks, and equations 1.34 and 1.35 for gluons, with LC helicity states assigned to the initial and final state hadrons. These matrix elements can then be expanded at leading twist in terms of the GPDs, as shown in section 1.3.4, and evaluated using the appropriate LC helicity spinors for the initial and final state hadrons. The following expressions relate the parton LC helicity conserving amplitudes to the GPDs.

$$A_{++,++}^{(LC)} = \sqrt{1-\xi^2} \left( \frac{H+\tilde{H}}{2} - \frac{\xi^2}{1-\xi^2} \frac{E+\tilde{E}}{2} \right) \quad (1.57)$$

$$A_{-+,-+}^{(LC)} = \sqrt{1-\xi^2} \left( \frac{H-\tilde{H}}{2} - \frac{\xi^2}{1-\xi^2} \frac{E-\tilde{E}}{2} \right) \quad (1.58)$$

$$A_{++,-+}^{(LC)} = -e^{-i\phi_D} \frac{\sqrt{t_0-t}}{2M} \frac{E-\xi\tilde{E}}{2} \quad (1.59)$$

$$A_{-+,++}^{(LC)} = e^{i\phi_D} \frac{\sqrt{t_0-t}}{2M} \frac{E+\xi\tilde{E}}{2} \quad (1.60)$$

where  $t_0$  is the least negative value possible for  $t$  at a given  $\xi$ , and  $\phi_D$  is the

azimuthal angle of the vector  $D$

$$t_0 = -\frac{4\xi^2 M^2}{1 - \xi^2}, \quad D = \frac{P'}{1 - \xi} - \frac{P}{1 + \xi} \quad (1.61)$$

and the remaining parton LC helicity conserving amplitudes can be solved using constraints from parity invariance. It is apparent that  $H$  and  $\tilde{H}$  are constrained to the four amplitudes that conserve hadron LC helicity, while  $E$  and  $\tilde{E}$  can contribute to all eight of the amplitudes. Also,  $H$  and  $E$  are sometimes referred to as "unpolarized", while  $\tilde{H}$  and  $\tilde{E}$  are sometimes referred to as "polarized", all with reference to the spin of the partons. See section 1.5 for more properties of the helicity conserving GPDs. In addition, the LC helicity amplitudes in the parton LC helicity flip sector can be expressed in terms of helicity-flip GPDs. This analysis will focus primarily on the helicity conserving GPDs.

#### 1.4.4 Gluon Fields in the $A^+ = 0$ Gauge

Feynman diagrams associated with soft processes involving gluons are evaluated using gluon fields. The gluon GPDs are instead evaluated by using gluon field strength tensors to derive either the LC helicity amplitudes in section 1.4.3 or the generalized gluon distributions. As a result, care must be taken when comparing these LC helicity amplitudes and generalized gluon distributions to the amplitudes that are directly associated with Feynman diagrams. In the  $A^+ = 0$  gauge, the field strength tensor components  $F^{+\mu}$  simplify to

$\partial^+ A^\mu$ . After applying the partial derivatives, the generalized gluon distributions can be expressed directly in terms of gluon fields as well. The conversion from gluon field strength tensors to gluon fields also introduces factors proportional to  $(x + \xi)(x - \xi)$  [1], partly due to the application of the  $\partial^+$  partial derivatives.

## 1.5 GPD Properties

The helicity conserving GPDs have several properties worth mentioning. A few of these properties are useful for linking the GPDs to experimental data. Some of the most relevant properties for this analysis pertain to the ways the GPDs reduce in the forward limit, when there is no net four-momentum transfer between the initial and final state hadrons. When  $\xi = 0$  and  $t = 0$ , some of the GPDs reduce to forms that involve PDFs. In the forward limit, the following expressions relate the GPDs to the PDFs.

for  $x > 0$

$$H^q(x, 0, 0) = q(x) , \quad \tilde{H}^q(x, 0, 0) = \Delta q(x) ,$$

$$H^g(x, 0, 0) = xg(x) , \quad \tilde{H}^g(x, 0, 0) = x\Delta g(x)$$

for  $x < 0$

$$H^q(x, 0, 0) = -\bar{q}(-x) , \quad \tilde{H}^q(x, 0, 0) = \Delta\bar{q}(-x) \quad (1.62)$$

where the PDF labels are the same as those defined in section 1.2.4. Note that the gluon GPDs  $H^g(x, \xi, t)$  and  $E^g(x, \xi, t)$  are even functions of  $x$ , while  $\tilde{H}^g(x, \xi, t)$  and  $\tilde{E}^g(x, \xi, t)$  are odd functions of  $x$ . This is because gluons are their own antiparticles. The  $E$  and  $\tilde{E}$  GPDs for quarks and gluons have no corresponding relations in the forward limit. They drop out from many expressions because they are often multiplied by terms proportional to  $\xi$  or  $t$ . It is very useful to define antisymmetric and symmetric combinations of the quark GPDs. This is similar to the concept of defining the nonsinglet and singlet combinations of the quark PDFs. The so called "singlet" combinations of the quark GPDs, which by definition here do not sum over quark flavors, are given by

$$\begin{aligned} H^{q(+)}(x, \xi, t) &= H^q(x, \xi, t) - H^q(-x, \xi, t) \\ \tilde{H}^{q(+)}(x, \xi, t) &= \tilde{H}^q(x, \xi, t) + \tilde{H}^q(-x, \xi, t) \end{aligned} \quad (1.63)$$

and the so called "nonsinglet" combinations are given by

$$\begin{aligned} H^{q(-)}(x, \xi, t) &= H^q(x, \xi, t) + H^q(-x, \xi, t) \\ \tilde{H}^{q(-)}(x, \xi, t) &= \tilde{H}^q(x, \xi, t) - \tilde{H}^q(-x, \xi, t) \end{aligned} \quad (1.64)$$

In the forward limit, for the case that  $x > 0$ , the combinations of GPDs reduce to

$$\begin{aligned} H^{q(\pm)}(x, 0, 0) &= q(x) \pm \bar{q}(x) \\ \tilde{H}^{q(\pm)}(x, 0, 0) &= \Delta q(x) \pm \Delta \bar{q}(x) \end{aligned} \tag{1.65}$$

These relations are useful for evaluating any potential models for the GPDs. Many groups have modeled the PDFs [4], and so the GPD models can be expressed in the forward limit and compared to these established PDF parametrizations.

The quark GPDs can be expressed as the sum of symmetric and antisymmetric contributions. This is beneficial for modeling the quark GPDs in the interval  $x \in [-\xi, \xi]$ , which is called the ERBL (Efremov, Radyushkin, Brodsky, Lepage) region. The symmetric and antisymmetric properties of the GPDs are most apparent in this region, as  $x = 0$  is the midpoint. The gluon GPDs are even simpler to model in this region, as each one is already either entirely odd or even in  $x$ .

### 1.5.1 Polynomiality and Moments in $x$

The moments in  $x$  of the GPDs are also important to discuss. They reveal the property of polynomiality, and direct integration over  $x$  relates the GPDs to the Dirac, Pauli, axial, and pseudoscalar form factors. The Mellin moments in  $x$  are evaluated by first considering moments of the generalized quark and

gluon distributions. For example, the following expression contributes to the moments of the quark distribution from equation 1.31

$$\begin{aligned}
(\bar{P}^+)^{n+1} \int dx x^n \int \frac{dz^-}{2\pi} e^{ix\bar{P}^+z^-} \left[ \bar{\psi}_q \left( -\frac{z}{2} \right) \gamma^+ \psi_q \left( \frac{z}{2} \right) \right]_{z^+=0, \mathbf{z}_\perp=0} \\
= \bar{\psi}_q(0) \gamma^+ (i \overleftrightarrow{\partial}^+)^n \psi_q(0)
\end{aligned} \tag{1.66}$$

where the abbreviation  $\overleftrightarrow{\partial}^\mu = \frac{1}{2}(\overrightarrow{\partial}^\mu - \overleftarrow{\partial}^\mu)$ . The Wilson line has been omitted in the  $A^+ = 0$  gauge. There are corresponding expressions for the other generalized quark and gluon distributions. Local twist-2 operators can be defined by generalizing the gauge and replacing the partial derivatives with the covariant derivatives,  $D^\mu = \partial^\mu - ig_s A^\mu$ . One set of operators for quarks is given by

$$\mathcal{O}_q^{\mu\mu_1\ldots\mu_n} = \mathcal{S} \bar{\psi}_q \gamma^\mu i \overleftrightarrow{D}^{\mu_1} \ldots i \overleftrightarrow{D}^{\mu_n} \psi_q \tag{1.67}$$

where  $\mathcal{S}$  denotes symmetrization in all uncontracted Lorentz indices, with a subtraction of trace terms. The operators contribute to the following expansion

in terms of the functions  $A_{n+1,i}^q(t)$ ,  $B_{n+1,i}^q(t)$ , and  $C_{n+1}^q(t)$

$$\begin{aligned}
\langle P' | \mathcal{O}_q^{\mu\mu_1 \dots \mu_n}(0) | P \rangle &= \mathcal{S} \bar{u}(P') \gamma^\mu u(P) \sum_{\substack{i=0 \\ \text{even}}}^n A_{n+1,i}^q(t) (-\Delta^{\mu_1}) \dots (-\Delta^{\mu_i}) \bar{P}^{\mu_{i+1}} \dots \bar{P}^{\mu_n} \\
&+ \mathcal{S} \bar{u}(P') \frac{i\sigma^{\mu\alpha}(-\Delta_\alpha)}{2M} u(P) \sum_{\substack{i=0 \\ \text{even}}}^n B_{n+1,i}^q(t) (-\Delta^{\mu_1}) \dots (-\Delta^{\mu_i}) \bar{P}^{\mu_{i+1}} \dots \bar{P}^{\mu_n} \\
&+ \mathcal{S} \frac{(-\Delta^\mu)}{M} \bar{u}(P') u(P) \text{mod}(n, 2) C_{n+1}^q(t) (-\Delta^{\mu_1}) \dots (-\Delta^{\mu_n})
\end{aligned} \tag{1.68}$$

where the function  $\text{mod}(n, 2)$  is 0 when  $n$  is even and 1 when  $n$  is odd. Restrictions have been imposed in consideration of time reversal invariance, such as the sum over even values of  $i$  so that the vector  $(-\Delta^\mu)$  appears in even powers. The operators with all uncontracted Lorentz indices taking the value  $+$  will contribute to the Mellin moments of the GPDs. These components of the operators can be evaluated by applying Gordon identities and using the relation that  $(-\Delta^+ = -2\xi \bar{P}^+)$ , and the results can be used to express the Mellin moments of the GPDs. This process can be repeated for the remaining quark and gluon operators as well. The other twist-2 operators are given by

$$\begin{aligned}
\tilde{\mathcal{O}}_q^{\mu\mu_1 \dots \mu_n} &= \mathcal{S} \bar{\psi}_q \gamma^\mu \gamma_5 i \overleftrightarrow{D}^{\mu_1} \dots i \overleftrightarrow{D}^{\mu_n} \psi_q \\
\mathcal{O}_g^{\mu\mu_1 \dots \mu_n \nu} &= \mathcal{S} G^{\mu\alpha} i \overleftrightarrow{D}^{\mu_1} \dots i \overleftrightarrow{D}^{\mu_n} G_\alpha^\nu \\
\tilde{\mathcal{O}}_g^{\mu\mu_1 \dots \mu_n \nu} &= \mathcal{S} (-i) G^{\mu\alpha} i \overleftrightarrow{D}^{\mu_1} \dots i \overleftrightarrow{D}^{\mu_n} \tilde{G}_\alpha^\nu
\end{aligned} \tag{1.69}$$

The Mellin moments for the quark GPDs are given in terms of their coefficient functions by the following:

$$\begin{aligned}
\int_{-1}^1 dx x^n H^q(x, \xi, t) &= \sum_{\substack{i=0 \\ \text{even}}}^n (2\xi)^i A_{n+1,i}^q(t) + \text{mod}(n, 2)(2\xi)^{n+1} C_{n+1}^q(t) \\
\int_{-1}^1 dx x^n E^q(x, \xi, t) &= \sum_{\substack{i=0 \\ \text{even}}}^n (2\xi)^i B_{n+1,i}^q(t) - \text{mod}(n, 2)(2\xi)^{n+1} C_{n+1}^q(t) \\
\int_{-1}^1 dx x^n \tilde{H}^q(x, \xi, t) &= \sum_{\substack{i=0 \\ \text{even}}}^n (2\xi)^i \tilde{A}_{n+1,i}^q(t) \\
\int_{-1}^1 dx x^n \tilde{E}^q(x, \xi, t) &= \sum_{\substack{i=0 \\ \text{even}}}^n (2\xi)^i \tilde{B}_{n+1,i}^q(t)
\end{aligned} \tag{1.70}$$

The Mellin moments for the gluon GPDs are given in terms of their coefficient functions as well. The gluon GPDs are each either odd or even in  $x$ , so the integrals are presented for  $x \geq 0$ . Only the even  $(n-1)$  moments, with odd  $n$ , of  $H^g$  and  $E^g$  can be nonzero, while only the odd  $(n-1)$  moments of  $\tilde{H}^g$  and  $\tilde{E}^g$  can be nonzero. The moments of the gluon GPDs are given by the expressions below, keeping in mind that these expressions only apply for the



corresponding odd or even  $n$  values that can give nonzero moments.

$$\begin{aligned}
\int_0^1 dx x^{n-1} H^g(x, \xi, t) &= \sum_{\substack{i=0 \\ \text{even}}}^n (2\xi)^i A_{n+1,i}^g(t) + \text{mod}(n, 2)(2\xi)^{n+1} C_{n+1}^g(t) \\
\int_0^1 dx x^{n-1} E^g(x, \xi, t) &= \sum_{\substack{i=0 \\ \text{even}}}^n (2\xi)^i B_{n+1,i}^g(t) - \text{mod}(n, 2)(2\xi)^{n+1} C_{n+1}^g(t) \\
\int_0^1 dx x^{n-1} \tilde{H}^g(x, \xi, t) &= \sum_{\substack{i=0 \\ \text{even}}}^n (2\xi)^i \tilde{A}_{n+1,i}^g(t) \\
\int_0^1 dx x^{n-1} \tilde{E}^g(x, \xi, t) &= \sum_{\substack{i=0 \\ \text{even}}}^n (2\xi)^i \tilde{B}_{n+1,i}^g(t)
\end{aligned} \tag{1.71}$$

The Mellin moments show the property of polynomiality. For fixed  $t$ , the  $x$ -integrals of  $x^n$  times the quark GPDs or  $x^{n-1}$  times the gluon GPDs result in polynomials in  $\xi$ . For the quark GPDs, the Mellin moments also isolate integrals of the "nonsinglet" and "singlet" GPD combinations, depending on the power of  $x^n$ . This happens because  $x^n$  is entirely odd or even in  $x$ , and so, depending on the value of  $n$ , the Mellin moments of a given quark GPD will isolate the contribution that is either symmetric or antisymmetric in  $x$ .

The moments with  $n = 0$  for the quark GPDs reduce to

$$\begin{aligned}
\int_{-1}^1 dx H^q(x, \xi, t) &= \mathcal{F}_1^q(t) \\
\int_{-1}^1 dx E^q(x, \xi, t) &= \mathcal{F}_2^q(t) \\
\int_{-1}^1 dx \tilde{H}^q(x, \xi, t) &= g_A^q(t) \\
\int_{-1}^1 dx \tilde{E}^q(x, \xi, t) &= g_P^q(t)
\end{aligned} \tag{1.72}$$

where  $\mathcal{F}_1^q(t)$  and  $\mathcal{F}_2^q(t)$  are the Dirac and Pauli form factors associated with the quark flavor  $q$ , and  $g_A^q(t)$  and  $g_P^q(t)$  are the corresponding axial and pseudoscalar form factors, all as functions of  $t$ . These relations are useful for evaluating any quark GPD models, as the first moments in  $x$  of the modeled GPDs can be compared to Form Factor expressions.

## 1.6 Modeling the GPDs

There have been efforts by various groups to model the GPDs. One method for modeling the GPDs involves double distributions. See [40] for a discussion of double distributions in detail. Other methods use a spectator model with a partonic interpretation. See [35] and [32] for earlier developments of the GPDs using a spectator model. The goal of this thesis is to build on previous efforts to model the GPDs using a spectator model. This analysis will discuss models for the GPDs that are associated with sea quarks and gluons.

# Chapter 2

## Kinematics

### 2.1 Conventions

This section defines the conventions that are used in this analysis. The processes used to calculate the GPDs involve fast moving particles. Many of these particles tend to have large momentum components along a light cone, so it is more convenient to express the momentum four-vectors with light cone variables [15]. The standard four-momentum  $P^\mu$  is expressed in a particular frame as  $(P^0, P^1, P^2, P^3)$  or  $(P^0, \vec{\mathbf{P}})$ . In the light cone representation, two four-vectors along the light cone are defined as  $p^\mu = \frac{1}{\sqrt{2}}(1, 0, 0, 1)$  and  $n^\mu = \frac{1}{\sqrt{2}}(1, 0, 0, -1)$ . In the new basis, the four-momentum is expressed as

$$P^\mu = (P^+, P^-, \mathbf{P}_\perp) \tag{2.1}$$

$$P^\pm = \frac{1}{\sqrt{2}}(P^0 \pm P^3), \quad \mathbf{P}_\perp = (P^1, P^2) \tag{2.2}$$

The invariant product of two arbitrary four-vectors is given by

$$A^\mu B_\mu = A^+ B^- + A^- B^+ - \mathbf{A}_\perp \cdot \mathbf{B}_\perp \quad (2.3)$$

The metric tensor and antisymmetric tensor use the conventions

$$g^{\mu\nu} = g_{\mu\nu} = \text{diag}(1, -1, -1, -1), \quad \epsilon_{0123} = -\epsilon^{0123} = 1 \quad (2.4)$$

Even permutations of the indices for the antisymmetric tensor give the same results, and odd permutations reverse the sign.  $\epsilon^{\mu\nu\rho\sigma} = 0$  if at least two indices have the same value. The transverse tensors are defined as

$$g_T^{\mu\nu} = g^{\mu\nu} - p^\mu n^\nu - p^\nu n^\mu, \quad \epsilon_T^{\mu\nu} = \epsilon^{\mu\nu\gamma\delta} n_\gamma p_\delta \quad (2.5)$$

Where the convention for the antisymmetric tensor matches that in [11]. For reference, the nonzero components are  $g_T^{11} = g_T^{22} = -1$  and  $\epsilon_T^{12} = 1 = -\epsilon_T^{21}$

The gamma matrices are expressed in the Dirac-Pauli representation. The 2x2 sigma matrices are the familiar Pauli matrices

$$\sigma_1 = \begin{pmatrix} 0 & 1 \\ 1 & 0 \end{pmatrix}, \quad \sigma_2 = \begin{pmatrix} 0 & -i \\ i & 0 \end{pmatrix}, \quad \sigma_3 = \begin{pmatrix} 1 & 0 \\ 0 & -1 \end{pmatrix} \quad (2.6)$$

and the gamma matrices are expressed in a condensed form as

$$\gamma^0 = \begin{pmatrix} I & 0 \\ 0 & -I \end{pmatrix}, \quad \gamma^k = \begin{pmatrix} 0 & \sigma^k \\ -\sigma^k & 0 \end{pmatrix}, \quad k = 1, 2, 3 \quad (2.7)$$

where  $I$  is the 2x2 identity matrix. Lastly, the combination  $\gamma^5 = i\gamma^0\gamma^1\gamma^2\gamma^3 =$   

$$\begin{pmatrix} 0 & I \\ I & 0 \end{pmatrix}$$

## 2.2 Kinematics

This section will establish the variable conventions and kinematics for the interactions used to calculate the GPDs. The soft amplitudes used to extract the GPDs in later chapters involve a proton emitting an interacting parton and leaving behind a spectator, followed by the spectator interacting with the returning parton to form a proton in the final state. There are two common conventions and sets of variables used to describe the four-momentum of the various particles, corresponding to two different frames. The "symmetric frame" uses Ji's convention [3] and the "asymmetric frame" uses Radyushkin's conventions [40]. The calculations in the two frames are equivalent and each has its advantages. The symmetric frame is useful for describing various properties of the GPDs, such as symmetry relations. The asymmetric frame has a more intuitive partonic interpretation and is used, with some minor changes to the original convention, to calculate the GPDs and soft Amplitudes in later chapters.

The protons' four-momenta are expressed in the following combinations:

$$\bar{P} = \frac{P + P'}{2}, \quad \Delta = P - P' \quad (2.8)$$

where  $P$  is the momentum of the initial proton, and  $P'$  is the final state proton's momentum. In the processes discussed below, the outgoing parton has momentum  $k$  and the incoming has momentum  $k'$ . The invariant momentum transfer squared is

$$t = \Delta^2 \quad (2.9)$$

The full Compton amplitude also involves the four-momenta of the incoming and outgoing photons,  $q$  and  $q'$  respectively. There is a general set of variables presented by Belitsky and Radyushkin [6]. Although many of the general terms involve Lorentz invariant quantities, they approximately reduce to the forms below for DVCS ( $q'^2 = 0$ ) in the Bjorken limit with fast moving photons ( $q^-$  dominates). In the symmetric frame, the momentum fraction of the partons,  $x$ , and the skewness variable,  $\xi$ , take the forms

$$x = \frac{k^+ + k'^+}{2\bar{P}^+}, \quad \xi = \frac{P^+ - P'^+}{P^+ + P'^+} \quad (2.10)$$

In the asymmetric frame, the momentum fraction of the outgoing parton,  $X$ , and the skewness variable,  $\zeta$  take the following forms

$$X = \frac{k^+}{P^+}, \quad \zeta = \frac{\Delta^+}{P^+} \simeq x_{Bj} \quad (2.11)$$

The two frames are connected by the simple transformations

$$x = \frac{X - \frac{\xi}{2}}{1 - \frac{\xi}{2}}, \quad X = \frac{x + \xi}{1 + \xi} \quad (2.12)$$

$$\xi = \frac{\frac{\xi}{2}}{1 - \frac{\xi}{2}}, \quad \zeta = \frac{2\xi}{1 + \xi} \quad (2.13)$$

Figure 2.1 shows the + light cone momentum fractions of each particle in the two frames. The asymmetric frame expresses the momenta in terms of the initial proton's light cone component  $P^+$ , so it has a more intuitive partonic interpretation.

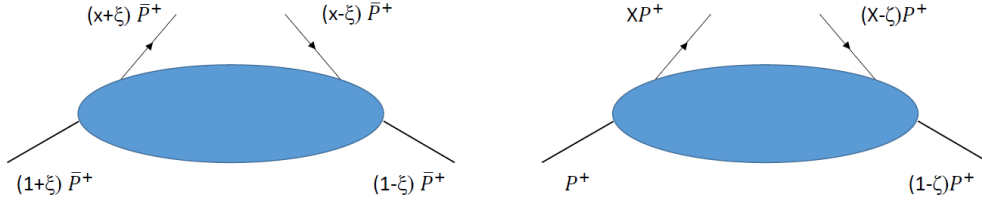


Figure 2.1: The figure above displays the plus-momentum components of the Hadrons and partons in the DGLAP region  $x > \xi$ . Left: Ji's convention and Right: Radyushkin's.

### 2.2.1 Note on Kinematic Regions of $x$

The kinematics in this chapter pertain to the DGLAP kinematic region with  $x > \xi$ . Technically the whole range spans the interval  $x \in [-1, 1]$ , but it is often split into three sections: Two DGLAP regions  $x \in [-1, -\xi]$  and  $x \in [\xi, 1]$ , and the ERBL region  $x \in [-\xi, \xi]$ . Each region has a unique partonic interpretation and slight variations in the momentum fractions of the partons. For the quark GPDs, the DGLAP region with  $x > \xi$  involves the emission and reabsorption

of a quark, while the DGLAP region with  $x < -\xi$  involves the emission and reabsorption of an antiquark. The ERBL region involves both a quark and an antiquark.

To summarize the partonic interpretation, quarks contribute for the region  $x \in [-\xi, 1]$ , and antiquarks contribute to the region  $x \in [-1, \xi]$ . The GPDs for valence quarks, sea quarks (no antiquarks), and gluons are calculated using the spectator model in the DGLAP region with  $x > \xi$ . The ERBL region is modeled with a functional polynomial parametrization that will be discussed in more detail. In this way, the GPDs are modeled for at least the interval  $x \in [0, 1]$ . Gluon GPDs obey symmetry and antisymmetry relations about  $x = 0$ , so they extend readily to the interval  $x \in [-1, 0]$ .

Quark GPDs are a bit more complicated, but they can be expressed in terms of the "singlet" and "nonsinglet" combinations that obey their own symmetry properties (see section 1.5).

$$H^q(x, \xi, t) = \frac{1}{2} \left( H^{q(+)}(x, \xi, t) + H^{q(-)}(x, \xi, t) \right) \quad (2.14)$$

If a quark GPD can be split analytically into a symmetric and an antisymmetric piece, then the GPD can be fully extended from the interval  $x \in [0, 1]$  to  $x \in [-1, 0]$ . Alternatively, it should theoretically be possible to model the contributions from antiquarks in the region with  $x < -\xi$ .



## 2.3 Spinors and Polarization Vectors

### 2.3.1 Spin $\frac{1}{2}$

There is a choice in the convention of the spinors used to describe spin  $\frac{1}{2}$  fermions. The following analysis uses the conventions outlined by Diehl [11]. For a spin  $\frac{1}{2}$  particle with four-momentum  $p$ , having components  $(p^0, p^1, p^2, p^3)$ , and helicity  $\lambda$ , the ordinary helicity spinors are given below. According to standard Feynman rules,  $U(p, \lambda)$  represents an incoming particle and  $V(p, \lambda)$  represents an outgoing antiparticle.

$$U(p, +) = \begin{pmatrix} \sqrt{p^0 + m} \chi_+(p) \\ \sqrt{p^0 - m} \chi_+(p) \end{pmatrix}, \quad U(p, -) = \begin{pmatrix} \sqrt{p^0 + m} \chi_-(p) \\ -\sqrt{p^0 - m} \chi_-(p) \end{pmatrix} \quad (2.15)$$

$$V(p, +) = \begin{pmatrix} -\sqrt{p^0 - m} \chi_-(p) \\ \sqrt{p^0 + m} \chi_-(p) \end{pmatrix}, \quad V(p, -) = \begin{pmatrix} -\sqrt{p^0 - m} \chi_+(p) \\ -\sqrt{p^0 + m} \chi_+(p) \end{pmatrix} \quad (2.16)$$

for helicity states with  $\pm$  corresponding to  $\lambda = \pm \frac{1}{2}$ . The two-spinors are defined as

$$\chi_+(\nu, \phi) = \begin{pmatrix} \cos(\frac{1}{2}\nu) \\ e^{i\phi} \sin(\frac{1}{2}\nu) \end{pmatrix}, \quad \chi_-(\nu, \phi) = \begin{pmatrix} -e^{-i\phi} \sin(\frac{1}{2}\nu) \\ \cos(\frac{1}{2}\nu) \end{pmatrix} \quad (2.17)$$

where the particle's three-momentum vector is oriented with the polar angle  $\nu$  and the azimuthal angle  $\phi$ . Each spinor has a counterpart using the notation

$$\bar{U} = U^\dagger \gamma^0 \quad (2.18)$$

and similarly for  $V$ . The bar notation is used to describe outgoing particles,  $\bar{U}(p, \lambda)$ , and incoming antiparticles,  $\bar{V}(p, \lambda)$ .

The amplitudes used to calculate the GPDs involve fast moving hadrons and partons that are dominated by either the  $+$  or  $-$  light cone momentum components. The momentum component along the light cone is large compared to the transverse component, and so the three-momentum vectors have polar angles with small deviations from 0 or  $\pi$ . The terms for a spin  $\frac{1}{2}$  object with a very large momentum component along the  $+\hat{z}$  direction that is dominated by the light cone  $+$  component are given below in the small angle approximation.

$$\cos(\frac{\nu}{2}) \simeq 1, \quad \sin(\frac{\nu}{2}) \simeq \frac{|p_\perp|}{\sqrt{2}p^+}, \quad p^0 \simeq p^3 \simeq \frac{p^+}{\sqrt{2}} \quad (2.19)$$

The terms for an object with a very large momentum component in the  $-\hat{z}$  direction that is dominated by the  $-$  light cone component are given in the small angle approximation (small  $\pi - \nu$ ) by

$$\cos(\frac{\nu}{2}) \simeq \frac{|p_\perp|}{\sqrt{2}p^-}, \quad \sin(\frac{\nu}{2}) \simeq 1, \quad p^0 \simeq -p^3 \simeq \frac{p^-}{\sqrt{2}} \quad (2.20)$$

In some cases, it may be necessary to expand the small angle approximations by including higher order terms. For example, if  $X = \zeta$ , then  $k'^+ = 0$ . For an object moving in the  $+\hat{z}$  direction with a large  $+$  component ( $p^3 \simeq \frac{p^+}{\sqrt{2}}$ )

$$|\vec{p}| = \sqrt{(p^3)^2 + p_\perp^2} \rightarrow \sqrt{\frac{(p^+)^2}{2} + p_\perp^2} \quad (2.21)$$

$$\sin(\nu) = \frac{|p_\perp|}{|\vec{p}|} \rightarrow \frac{1}{\sqrt{\left(\frac{(p^+)^2}{2p_\perp^2} + 1\right)}} \quad (2.22)$$

$$\cos(\nu) = \frac{p^3}{|\vec{p}|} \rightarrow \frac{1}{\sqrt{\left(1 + \frac{2p_\perp^2}{(p^+)^2}\right)}} \quad (2.23)$$

And the half angle expressions are

$$\cos\left(\frac{\nu}{2}\right) = \sqrt{\frac{1 + \cos(\nu)}{2}}, \quad \sin\left(\frac{\nu}{2}\right) = \sqrt{\frac{1 - \cos(\nu)}{2}} \quad (2.24)$$

In the case that  $\sqrt{2}p_\perp \ll p^+$ , the expressions reduce to the form in equation (2.19)

### 2.3.2 Spin 1

The polarization vectors for spin 1 bosons are outlined in this section. For a spin 1 object with momentum  $p$  traveling in the  $+\hat{z}$  direction, the transverse polarization vectors are given by

$$\epsilon^\mu(\Lambda) = \frac{1}{\sqrt{2}}(0, -\Lambda, -i, 0) \quad (2.25)$$

where  $\Lambda = \pm 1$  is the object's helicity. For a massive spin 1 object, with mass  $M$ , the longitudinal polarization ( $\Lambda = 0$ ) is given by

$$\epsilon^\mu = \frac{1}{M}(p^3, 0, 0, p^0) \quad (2.26)$$

where these polarization vectors have the relations that  $p^\mu \epsilon_\mu = 0$  and  $\epsilon^\mu \epsilon_\mu = -1$ .

The polarization vectors above are defined in a coordinate system  $(x, y, z)$  with basis  $\mathcal{X}(\hat{x}, \hat{y}, \hat{z})$ . The polarization vectors for a spin 1 boson with  $\vec{p}$  aligned in any direction can be obtained by starting with the expressions above and applying a series of rotations. Alternatively, it is possible to define a new coordinate system  $(x', y', z')$  with the basis  $\mathcal{X}_{rotated}(\hat{x}', \hat{y}', \hat{z}')$  by rotating the original coordinate system so that  $\hat{z}'$  is aligned with  $\vec{p}$ . The new coordinate system is obtained with the three intrinsic rotations below, using the azimuthal angle  $\phi$  and the polar angle  $\theta$  of the boson's three-momentum  $\vec{p}$ . The rotations are consistent with the Jacob-Wick convention. There are a total of three rotations, so there are two intermediate coordinate systems:  $(x_1, y_1, z_1)$  with basis  $\mathcal{X}_1$  after the first rotation, and  $(x_2, y_2, z_2)$  with basis  $\mathcal{X}_2$  after the second.

$$\mathcal{X}_{rotated} = R^{z_2}(-\phi)R^{y_1}(\theta)R^z(\phi)\mathcal{X} \quad (2.27)$$

$$\mathcal{X}_{rotated} = R^{z_2}(-\phi)\mathcal{X}_2, \quad \mathcal{X}_2 = R^{y_1}(\theta)\mathcal{X}_1, \quad \mathcal{X}_1 = R^z(\phi)\mathcal{X} \quad (2.28)$$

Where the rotation matrix  $R$  rotates the coordinate basis about the axis in the

index. For any given coordinate system  $(x_i, y_i, z_i)$  with basis  $\mathcal{X}_i$ , the rotation matrices  $R^{x_i, y_i, z_i}$  that act on  $\mathcal{X}_i$  are given by

$$\begin{aligned}
R^{x_i}(\phi) &= \begin{pmatrix} 1 & 0 & 0 \\ 0 & \cos(\phi) & \sin(\phi) \\ 0 & -\sin(\phi) & \cos(\phi) \end{pmatrix}, \quad R^{y_i}(\phi) = \begin{pmatrix} \cos(\phi) & 0 & -\sin(\phi) \\ 0 & 1 & 0 \\ \sin(\phi) & 0 & \cos(\phi) \end{pmatrix}, \\
R^{z_i}(\phi) &= \begin{pmatrix} \cos(\phi) & \sin(\phi) & 0 \\ -\sin(\phi) & \cos(\phi) & 0 \\ 0 & 0 & 1 \end{pmatrix}
\end{aligned} \tag{2.29}$$

and the matrix representation for  $\mathcal{X}_i$  is

$$\mathcal{X}_i = \begin{pmatrix} \hat{x}_i \\ \hat{y}_i \\ \hat{z}_i \end{pmatrix} \tag{2.30}$$

Different conventions may vary in the orientation of the  $x'$  and  $y'$  axes in the plane perpendicular to the  $z'$  axis. A rotation about the  $z'$  axis creates a transversity state, and the transverse polarization vector in the new basis is given by

$$\mathcal{X}_T = R^{z'}(\phi) \mathcal{X}' \tag{2.31}$$

$$\vec{\epsilon}(\Lambda) \rightarrow \frac{1}{\sqrt{2}} \begin{pmatrix} -\Lambda \hat{x}_T - i \hat{y}_T \end{pmatrix} = \frac{e^{-i\Lambda\phi}}{\sqrt{2}} \begin{pmatrix} -\Lambda \hat{x}' - i \hat{y}' \end{pmatrix} \tag{2.32}$$

and the results of the three rotations convention used in this analysis can be easily compared to different conventions.

A spin 1 boson's transverse polarization vector is defined using equation (2.25) in the rotated coordinate system,  $(\hat{x}', \hat{y}', \hat{z}')$ . Next, the basis vectors for the rotated coordinate system can be expanded in terms of the original basis vectors  $(\hat{x}, \hat{y}, \hat{z})$ . The resulting expression for the transverse polarization vector is

$$\begin{aligned} \vec{\epsilon}(\Lambda_g)_{rotated} = \frac{e^{i\Lambda_g\phi}}{\sqrt{2}} & \left( [-\Lambda_g \cos(\theta) \cos(\phi) + i(\sin(\phi))] \hat{x} \right. \\ & + [-\Lambda_g \cos(\theta) \sin(\phi) - i(\cos(\phi))] \hat{y} \\ & \left. + [\Lambda_g \sin(\theta)] \hat{z} \right) \end{aligned} \quad (2.33)$$

If the object is moving with a large + light cone momentum component, and the component in the  $+\hat{z}$  direction is very large compared to the transverse component, then  $\theta$  is treated as small. The expression above simplifies as follows in the small angle approximation.

$$\cos(\theta) \simeq 1, \quad \sin(\theta) \simeq \frac{2|p_\perp|}{(\sqrt{2}p^+)} \quad (2.34)$$

$$\epsilon^\mu(\Lambda_g) = \frac{1}{\sqrt{2}}(0, -\Lambda_g, -i, \Lambda_g \frac{2|p_\perp|}{\sqrt{2}p^+} e^{i\Lambda_g\phi}) \quad (2.35)$$

Interestingly, the transverse polarization vector in the small angle approximation retains the same form as before but with an additional  $\epsilon^3$  component. In this limit, the rotation is essentially an Euler rotation on the coordinate

system that swivels the  $z$  axis to point in the direction of the  $z'$  axis directly in one rotation. Because the polar angle is small, the axes shift by a small amount.

For spin 1 bosons that travel exactly in the  $-\hat{z}$  direction, the polarization vector simplifies to the expression below after the rotations with  $\theta = \pi, \phi = 0$ . The coordinate system is rotated once by  $\pi$  about the  $y$  axis ( $\hat{x}' = -\hat{x}, \hat{y}' = \hat{y}, \hat{z}' = -\hat{z}$ ).

$$\text{if } \hat{p} = -\hat{z}, \quad \epsilon^\mu(\Lambda) = \frac{1}{\sqrt{2}}(0, \Lambda, -i, 0) \quad (2.36)$$

There is some ambiguity for the phase in the form of an overall factor  $e^{2i\Lambda\phi}$ . This convention sets  $\phi = 0$  to simplify the expression, but other conventions may select alternative phases. For example,  $\phi = \frac{\pi}{2}$  gives a factor of  $-1$ , and  $\epsilon^\mu(\Lambda)_{-\hat{z}} = \frac{1}{\sqrt{2}}(0, -\Lambda, i, 0)$ . This alternative convention is equivalent to rotating the coordinate system once by  $\pi$  about the  $x$  axis instead ( $\hat{x}' = \hat{x}, \hat{y}' = -\hat{y}, \hat{z}' = -\hat{z}$ ).

## 2.4 Factorization and the Spectator Model

Factorization is essential for the partonic interpretation of the Compton scattering process. The handbag diagram separates the soft and hard contributions to the full scattering process. The photons are treated as interacting with free partons in the hard scattering process, while the soft amplitude involves the

interactions between the protons and the free partons. The full Compton amplitude is calculated by the contributions from the hard amplitudes and combinations of the GPDs that comprise the soft amplitudes.

The Compton amplitude can also be calculated strictly from helicity amplitudes using the spectator model. The helicity amplitudes for DVCS at leading order in  $\frac{1}{Q}$  are given by

$$f_{\Lambda_\gamma, \Lambda; \Lambda'_\gamma, \Lambda'} = \epsilon_\mu^{\Lambda_\gamma} T_{\Lambda\Lambda'}^{\mu\nu} \epsilon_\nu^{*\Lambda'_\gamma} \quad (2.37)$$

where the helicities for the initial and final protons are  $\Lambda$  and  $\Lambda'$  respectively, and the initial and final photon helicities are  $\Lambda_\gamma$  and  $\Lambda'_\gamma$ .  $T_{\Lambda\Lambda'}^{\mu\nu}$  is the helicity amplitude for DVCS without the external photons.  $\epsilon_\mu^{\Lambda_\gamma}$  is the polarization vector for the incoming virtual photon, and  $\epsilon_\nu^{*\Lambda'_\gamma}$  is for the outgoing photon.

The helicity amplitudes can be decomposed into the following with a convolution integral  $\otimes \rightarrow \int_{-1+\zeta}^1 dX$

$$f_{\Lambda_\gamma, \Lambda; \Lambda'_\gamma, \Lambda'} = \sum_{\lambda, \lambda'} g_{\lambda, \lambda'}^{\Lambda_\gamma, \Lambda'_\gamma}(X, \zeta, t; Q^2) \otimes A_{\Lambda', \lambda'; \Lambda, \lambda}(X, \zeta, t) \quad (2.38)$$

where  $g_{\lambda, \lambda'}^{\Lambda_\gamma, \Lambda'_\gamma}(X, \zeta, t; Q^2)$  is the helicity amplitude for the hard partonic subprocess between the photons and the interacting partons,  $(\gamma^* + q \rightarrow \gamma + q)$  for quarks, or  $(\gamma^* + g \rightarrow \gamma + g)$  for gluons. The initial and final state partons have helicity  $\lambda$  and  $\lambda'$ , respectively.  $A_{\Lambda', \lambda'; \Lambda, \lambda}(X, \zeta, t)$  is the soft helicity amplitude involving the partons that participate in the hard subprocess and the protons.



The full partonic structure of each helicity amplitude is model dependent and will be discussed in the next chapter.

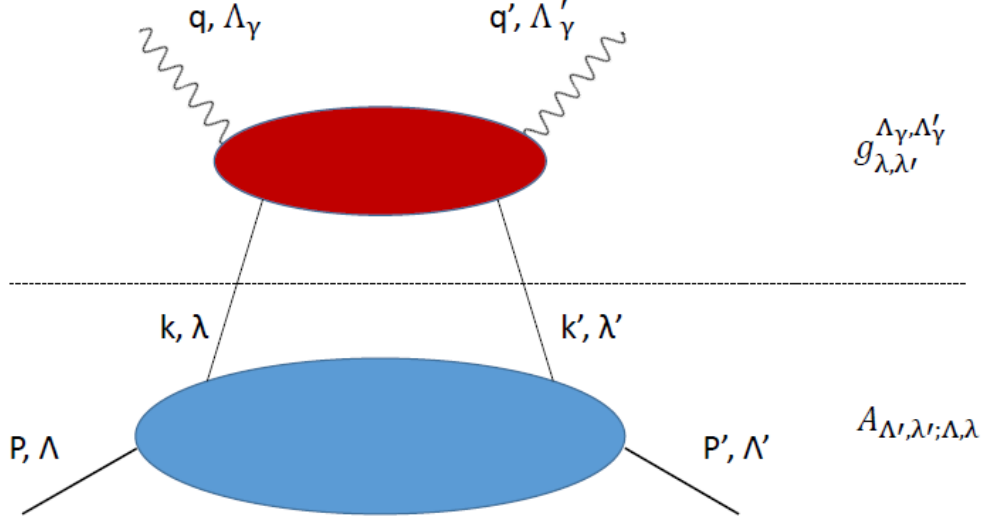


Figure 2.2: The figure above shows the momentum and helicity labels of the Compton scattering diagram. The section below the dashed line is the soft subprocess, and the section above the dashed line is the hard subprocess.

### 2.4.1 Soft Amplitude Kinematics

The soft helicity amplitudes are discussed for DVCS in the DGLAP region with  $X > \zeta$ . The proton emits and reabsorbs a parton, in this case either a quark or a gluon.

The kinematics shown below are in the Light Cone coordinate system defined with the incoming proton's momentum in the  $\hat{z}$  direction. In the asym-

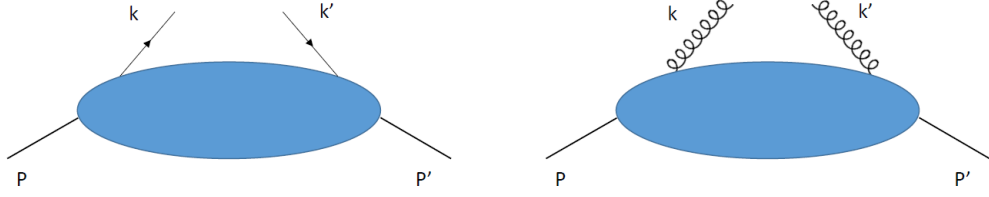


Figure 2.3: The figure above displays the soft subdiagram for quarks (left) and gluons (right) in the DGLAP region.

metric frame, the kinematics take the following form

$$P^\mu = \left( P^+, \frac{M^2}{2P^+}, 0 \right) \quad (2.39)$$

$$k^\mu = \left( XP^+, k^-, \vec{k}_\perp \right) \quad (2.40)$$

$$P'^\mu = \left( (1 - \zeta)P^+, \frac{M^2 + \Delta_\perp^2}{2(1 - \zeta)P^+}, -\vec{\Delta}_\perp \right) \quad (2.41)$$

$$k'^\mu = \left( (X - \zeta)P^+, k'^-, \vec{k}_\perp - \vec{\Delta}_\perp \right) \quad (2.42)$$

$$P_X^\mu = \left( (1 - X)P^+, P^- - k^-, -\vec{k}_\perp \right) \quad (2.43)$$

$$\Delta^\mu = \left( \zeta P^+, \frac{-(M^2\zeta + \Delta_\perp^2)}{2(1 - \zeta)P^+}, \vec{\Delta}_\perp \right) \quad (2.44)$$

Where the momentum  $P_X \equiv P - k$  will be useful in the partonic interpretation of the spectator model. The partons are not necessarily on-shell, and so the light cone components are not specified. They will be expressed later for the spectator model.

Using the relation  $t = \Delta^2$ , the invariant four-momentum transfer squared

expands to

$$t = t_0 - \frac{\Delta_\perp^2}{1 - \zeta}, \quad t_0 = \frac{-\zeta^2 M^2}{1 - \zeta} \quad (2.45)$$

For  $\zeta$  fixed,  $t_0$  serves as a bound on  $t$  in the case that  $\Delta_\perp^2 = 0$ . The contributions to  $t$  are all negative, with the condition that  $t \leq t_0$ .

### 2.4.2 Hard Amplitude Kinematics

The hard helicity amplitudes are established in the Light Cone coordinate system defined with the incoming proton's momentum in the  $+\hat{z}$  direction. The incoming virtual photon with four-momentum  $q$  travels with a large component in the  $-\hat{z}$  direction. The outgoing photon travels with four-momentum  $q' = q + \Delta$ . The hard subprocess is expanded in the usual series of Feynman diagrams. The diagrams of interest to the GPDs are the contributions in the Bjorken limit at the lowest orders of Twist and  $\alpha_s$ . The LO (Leading Order) diagrams in  $\alpha_s$  have been calculated for quarks, and the NLO (Next-to-Leading Order) diagrams are discussed by various groups for quarks and gluons [30] [29] [1].

Each diagram can be Taylor expanded in terms of the external momenta components that are small on the scale of  $Q$ . The leading contributions to the hard helicity amplitudes are evaluated with a collinear expansion that sets the external partons on shell, with small - light cone and transverse components for  $k$  and  $k'$ . The partons are approximated as having negligible mass

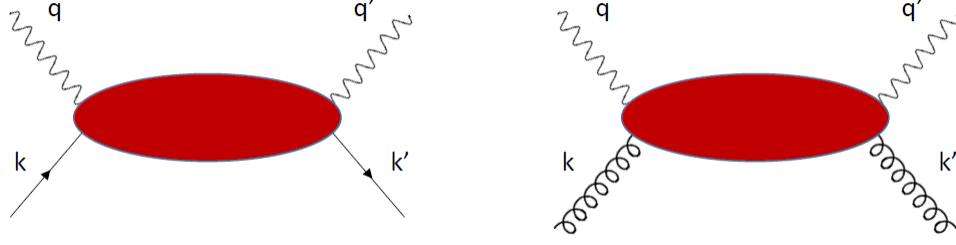


Figure 2.4: The figure above displays the hard subdiagram for quarks (left) and gluons (right) in the DGLAP region.

$m_k = 0, m_{k'} = 0$ . The hard amplitudes can be calculated in this collinear approximation [8] with the following kinematics

$$k^\mu \simeq (XP^+, 0, 0) \quad (2.46)$$

$$k'^\mu \simeq ((X - \zeta)P^+, 0, 0) \quad (2.47)$$

$$q_\perp = 0 \quad (2.48)$$

These approximations, with the additional approximation that  $\Delta_\perp = 0$ , isolate the dominant contributions to the hard helicity amplitudes on the scale of  $Q$ . The partons travel directly in the  $+\hat{z}$  direction, while the photons travel directly in the  $-\hat{z}$  direction.

The helicity conserving GPDs involve interactions for the quarks and gluons with  $\lambda = \lambda'$  in the hard and soft amplitudes. The outgoing photon is on shell, so its polarization states are purely transverse with  $\Lambda'_\gamma = \pm 1$ . For the gluon

polarization vectors in the collinear limit,

$$\epsilon_{k'}^{*\mu}(+)\epsilon_k^\nu(+) + \epsilon_{k'}^{*\mu}(-)\epsilon_k^\nu(-) = -g_T^{\mu\nu}, \quad (2.49)$$

$$\epsilon_{k'}^{*\mu}(+)\epsilon_k^\nu(+) - \epsilon_{k'}^{*\mu}(-)\epsilon_k^\nu(-) = i\epsilon_T^{\mu\nu} \quad (2.50)$$

and for photon polarization vectors in the collinear limit

$$\epsilon_{q'}^{*\mu}(+)\epsilon_q^\nu(+) + \epsilon_{q'}^{*\mu}(-)\epsilon_q^\nu(-) = -g_T^{\mu\nu}, \quad (2.51)$$

$$\epsilon_{q'}^{*\mu}(+)\epsilon_q^\nu(+) - \epsilon_{q'}^{*\mu}(-)\epsilon_q^\nu(-) = -i\epsilon_T^{\mu\nu} \quad (2.52)$$

where  $\pm$  indicates a helicity state of  $\pm 1$ .

The Mandelstam variables for the hard subprocess are given by

$$\hat{s} = (k + q)^2, \quad \hat{t} = (k' - k)^2, \quad \hat{u} = (k' - q)^2 \quad (2.53)$$

In the Bjorken limit, the incoming photon's momentum is dominated by the Light Cone component

$$q^- \simeq \frac{Q^2}{2\zeta P^+} \quad (2.54)$$

The leading contribution in  $Q^2$  for each of the Mandelstam variables are given

as

$$\hat{s} \simeq \frac{Q^2(X - \zeta)}{\zeta}, \quad (2.55)$$

$$\hat{u} \simeq -\frac{Q^2 X}{\zeta}, \quad (2.56)$$

$$\hat{t} = t \quad (2.57)$$

# Chapter 3

## GPD Models

### 3.1 Soft Helicity Amplitudes

#### 3.1.1 Quark Soft Amplitude Structure

The soft helicity amplitudes for quarks involve the following process in the DGLAP region with  $X > \zeta$ . A proton emits a quark, leaving behind a spectator object. The spectator then reabsorbs a quark and forms a proton in the final state. The helicity amplitudes can be separated based on the helicities of the quarks and protons. For valence quarks, the model for the spectator is a diquark object that has a scalar ( $S = 0$ ) and an axial-vector ( $S = 1$ ) spin configuration. The full axial-vector coupling adds complexity to the model with little benefit, so the axial-vector couplings are assumed to have a similar form as the scalar couplings in this model. The helicity amplitudes are evaluated with a scalar diquark object, and the mass parameters vary in order

to distinguish predictions for up and down quarks. The sea quark amplitudes are similarly evaluated, but with a  $(\bar{q}qqq)$  spectator for quarks. The antiquark amplitudes are not evaluated in this kinematic region. This spectator is also treated as a single scalar ( $S = 0$ ) object in this model. The current models are reasonable, but of course a fully rigorous analysis would examine the complete range of couplings and spectator configurations.

The soft amplitudes can be expressed in terms of vertex functions that describe the initial process of a proton emitting a quark, and the final process of a quark being reabsorbed. The full helicity amplitude is expressed as follows

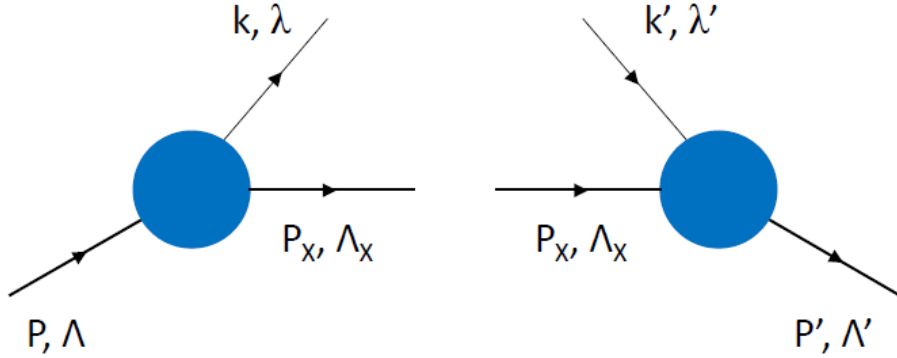


Figure 3.1: The vertex diagrams with four-momentum and helicity labels.

$$A_{\Lambda', \lambda'; \Lambda, \lambda}^q = \int dk^+ \int d^2 k_\perp \int dk^- \delta(k^+ - XP^+) \frac{i\phi_{\Lambda', \lambda'}^*(k', P') \phi_{\Lambda, \lambda}(k, P)}{P_X^2 - M_X^2} \quad (3.1)$$



The vertex structures are defined as

$$\phi_{\Lambda,\lambda}(k, P) = \Gamma^q(k) \frac{\bar{u}(k, \lambda) U(P, \Lambda)}{(k^2 - m_q^2)} \quad (3.2)$$

$$\phi_{\Lambda',\lambda'}^*(k', P') = \Gamma^q(k') \frac{\bar{U}(P', \Lambda') u(k', \lambda')}{(k'^2 - m_q^2)} \quad (3.3)$$

where the denominators of the parton propagators are absorbed in the vertex functions. The scalar coupling for the proton-quark-spectator vertex is

$$\Gamma^q(k) = g_s \frac{k^2 - m_q^2}{(k^2 - M_\Lambda^2)^n} \quad (3.4)$$

where  $n = 2$  for valence quarks and  $n = 3$  for sea quarks. For valence quarks, the form resembles the vertex functions in [16], though the form is slightly different.

### 3.1.2 Gluon Soft Amplitude Structure

The soft helicity amplitudes for gluons involve the following process in the DGLAP region with  $X > \zeta$ . A proton emits a gluon, leaving behind a spin  $\frac{1}{2}$  spectator in this model. The spectator resembles a proton in a color-octet state, as the emitted gluon carries a color charge away from the color neutral initial proton. Next, the spectator reabsorbs a gluon and forms a proton in the final state. The amplitudes can be separated based on the helicities of the protons and gluons. A fully rigorous future analysis could examine the complete range of couplings and spectator configurations.

The full helicity amplitude in the  $A^+ = 0$  gauge is expressed as follows

$$A_{\Lambda', \Lambda'_g; \Lambda, \Lambda_g}^g = \int dk^+ \int d^2 k_\perp \int dk^- \delta(k^+ - X P^+) \bar{U}(P', \Lambda') \Phi^\nu(k') \frac{i(\not{P}_X + M_X)}{P_X^2 - M_X^2} \Phi^\mu(k) U(P, \Lambda) \epsilon_{\nu, \Lambda'_g}(k') \epsilon_{\mu, \Lambda_g}^*(k) \quad (3.5)$$

where the vector coupling at the gluon-proton-spectator vertex is defined as

$$\Phi^\mu(k) = \Gamma^g(k) \frac{1}{k^2 - m_g^2} \gamma^\mu, \quad (3.6)$$

$$\Gamma^g(k) = g_s \frac{k^2 - m_g^2}{(k^2 - M_\Lambda^2)^2} \quad (3.7)$$

The scalar vertex function  $\Gamma^g$  is chosen to resemble  $\gamma NN$  coupling. It also resembles the vertex functions in [16], though the form is slightly different. The soft amplitude can also be expressed in terms of vertex functions. The vertex structures describe the initial process of proton emitting a gluon, and the final process of a gluon being reabsorbed.

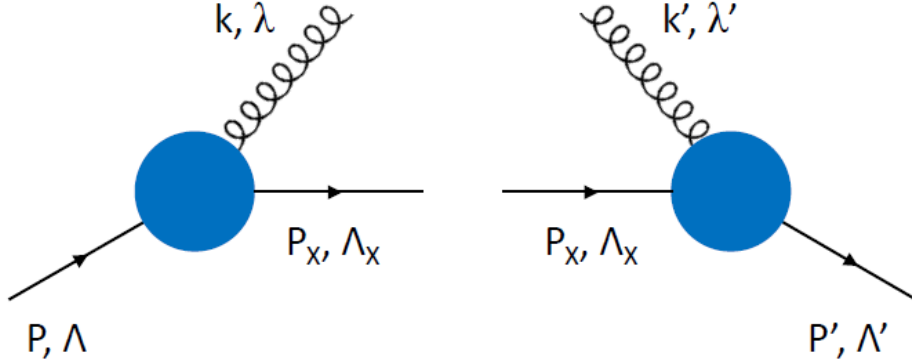


Figure 3.2: The vertex diagrams with four-momentum and helicity labels. The label  $\lambda$  is used interchangeably with  $\Lambda_g$ , and the label  $\lambda'$  is used interchangeably with  $\Lambda'_g$ .

The vertex functions are

$$\mathcal{G}_{\Lambda_X; \Lambda_g, \Lambda}(k, P) = \Gamma^g(k) \frac{\bar{U}(P_X, \Lambda_X) \not{\epsilon}_{\Lambda_g}^*(k) U(P, \Lambda)}{k^2 - m_g^2} \quad (3.8)$$

$$\mathcal{G}_{\Lambda_X; \Lambda'_g, \Lambda'}^*(k', P') = \Gamma^g(k') \frac{\bar{U}(P', \Lambda') \not{\epsilon}_{\Lambda'_g}(k') U(P_X, \Lambda_X)}{k'^2 - m_g^2} \quad (3.9)$$

After expanding the spectator term

$$\not{P}_X + M_X = \sum_{\Lambda_X} \left( U(P_X, \Lambda_X) \bar{U}(P_X, \Lambda_X) \right) \quad (3.10)$$

and integrating over  $k^+$ , the soft amplitudes can be expressed in a new form

$$A_{\Lambda', \Lambda'_g; \Lambda, \Lambda_g}^g = \int d^2 k_\perp \int dk^- \frac{i}{P_X^2 - M_X^2} \sum_{\Lambda_X} \mathcal{G}_{\Lambda_X; \Lambda'_g, \Lambda'}^*(k', P') \mathcal{G}_{\Lambda_X; \Lambda_g, \Lambda}(k, P) \Big|_{(k^+ = X P^+)} \quad (3.11)$$

The gluons are assumed to be massless in this model ( $m_g = 0$ ), and only transverse polarization states are considered.

### 3.1.3 Notes on Extra Kinematics

It is important to note that the soft amplitudes for gluons are evaluated in the  $A^+ = 0$  gauge. There is a conversion factor that relates the gauge invariant GPDs to the soft amplitudes in this particular gauge. There are other considerations as well for quark and gluon GPDs, such as a factor of  $P^+$  due to the factorization theorem. Essentially, there are extra kinematics that must be considered when solving the quark and gluon GPDs from the soft amplitudes.

These extra kinematics will be discussed in a later section. There is also a color factor, but all constants in the soft amplitude will be grouped into a normalization parameter.

## 3.2 $k^-$ Contour Integration

The soft helicity amplitudes for quarks and gluons are integrated first by  $dk^-$ . Mathematically, it is convenient to introduce a factor of  $\frac{P^+}{P^+}$  to the amplitude, so that the integral is over  $dk^- P^+$ . This integral is the simplest to perform because of the terms with poles in the denominator. There are three sources of poles:

$$(1) \quad \frac{1}{(k^2 - M_\Lambda^2 + i\epsilon)^n}, \quad (2) \quad \frac{1}{(k'^2 - M_\Lambda^2 + i\epsilon)^n}, \quad (3) \quad \frac{1}{P_X^2 - M_X^2 + i\epsilon} \quad (3.12)$$

where  $n = 3$  for sea quarks, and  $n = 2$  for valence quarks and gluons. The term of  $i\epsilon$  is introduced to bring the poles into the imaginary plane, while the final expression is evaluated with  $\epsilon \rightarrow 0$ . First, the expressions are evaluated at the poles, when the term in the denominator is 0, and solved in terms of  $k^- P^+$ .

$$[k^- P^+]_1 = \frac{M_\Lambda^2 + k_\perp^2}{2X} - \frac{i\epsilon}{2X} \quad (3.13)$$

$$[k^- P^+]_2 = \frac{M_\Lambda^2 + |\vec{k}_\perp - \vec{\Delta}_\perp|^2}{2(X - \zeta)} + \frac{t + \Delta_\perp^2}{2\zeta} - \frac{i\epsilon}{2(X - \zeta)} \quad (3.14)$$

$$[k^- P^+]_3 = \frac{(1 - X)M^2 - M_X^2 - k_\perp^2}{2(1 - X)} + \frac{i\epsilon}{2(1 - X)} \quad (3.15)$$

It can be seen that for the DGLAP region with  $X > \zeta$ , the sign of the imaginary piece is different for the third term. This means that the first two terms in equation (3.12) have double or triple poles with a negative imaginary part while the third term has a single pole with a positive imaginary part. The  $k^-P^+$  integral is carried out using countour integration over the positive imaginary region of the complex  $k^-P^+$  plane, to isolate the residue of the pole in the spectator's propagator [14].

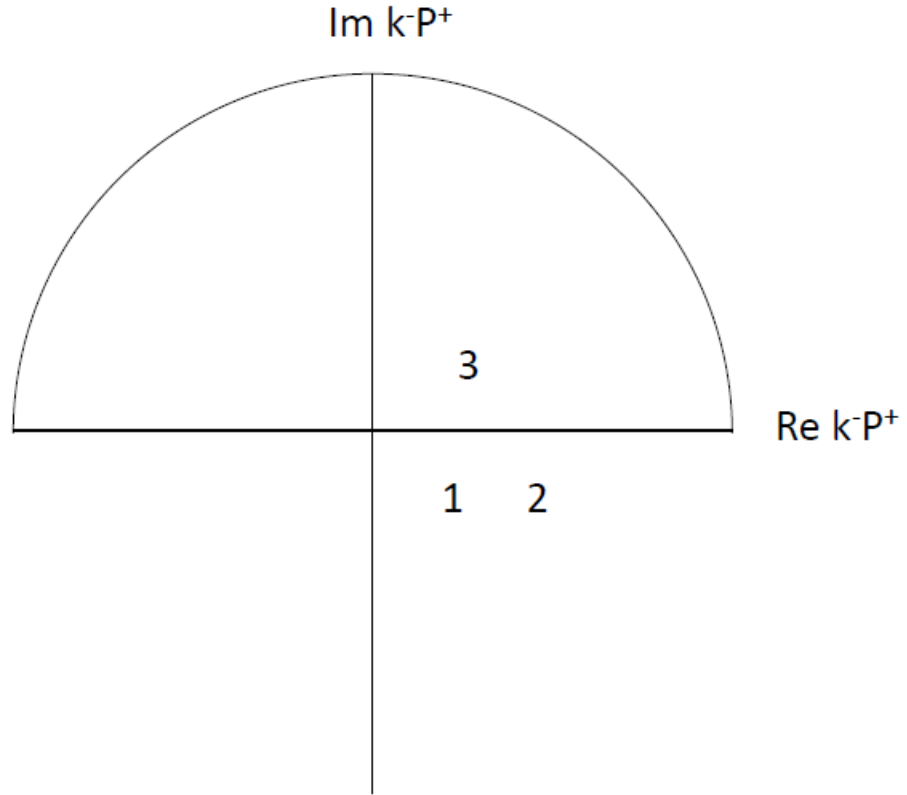


Figure 3.3: The figure above shows the contour integration in the complex plane for  $k^-P^+$ , in the DGLAP region with  $X > \zeta$ . The numbers 1, 2, and 3 indicate whether the poles in equation (3.12) are in the positive or negative imaginary region. The contour integration closes around the simple pole in the spectator's propagator.

The contour integration effectively puts the spectator on shell, as the pole occurs at  $P_X^2 - M_X^2 = 0$  as  $\epsilon \rightarrow 0$ . The integration has the following effect on the soft amplitudes. Let  $f$  represent the remainder of the soft amplitude that does not include the spectator's propagator.

$$A_{\Lambda', \lambda'; \Lambda, \lambda} = \int dk^- P^+ \frac{i}{(P_X^2 - M_X^2)} f \quad (3.16)$$

After the contour integration over the complex  $k^- P^+$  plane, the soft amplitude reduces in the following way

$$\int dk^- P^+ \frac{i}{(P_X^2 - M_X^2)} f = \frac{\pi}{(1 - X)} f|_{P_X^2 = M_X^2} \quad (3.17)$$

and the constants are absorbed into the normalization factor. A factor of  $\frac{1}{(1-X)}$  is introduced, and the soft amplitude is evaluated with the spectator on shell. The partons are off shell, and the momenta expand as follows

$$\begin{aligned} k^2 - M_\Lambda^2 &= XM^2 - \frac{X}{1-X} M_X^2 - M_\Lambda^2 - \frac{k_\perp^2}{1-X}, \\ k'^2 - M_\Lambda^2 &= \frac{X-\zeta}{1-\zeta} M^2 - \frac{X-\zeta}{1-X} M_X^2 - M_\Lambda^2 - \frac{1-\zeta}{1-X} \left( \vec{k}_\perp - \frac{1-X}{1-\zeta} \vec{\Delta}_\perp \right)^2 \end{aligned} \quad (3.18)$$

Note that the imaginary part of some of the poles change sign in different kinematic regions for  $X$ . The contour integration procedure is not the same in the ERBL region, because the pole for  $[k^- P^+]_2$  is now positive in the

imaginary plane. The contour integration now encloses a double or triple pole in the negative imaginary plane, and sets  $k^- P^+ = [k^- P^+]_1$ . The spectator is no longer on shell. The spectator model is not evaluated in the ERBL region for this analysis. Instead, a functional polynomial parametrization is applied.

### 3.3 Soft Amplitude Calculations

#### 3.3.1 Quark Soft Amplitudes

The quark vertex functions give the following results for a scalar spectator object.

$$\phi_{++}(k, P) = \frac{1}{\sqrt{X}} (m_q + XM) \frac{\Gamma^q(k)}{k^2 - m_q^2} \quad (3.20)$$

$$\phi_{-+}(k, P) = \frac{1}{\sqrt{X}} (k_1 - ik_2) \frac{\Gamma^q(k)}{k^2 - m_q^2} \quad (3.21)$$

$$\phi_{++}(k, P) = \phi_{--}^*(k, P) \quad \phi_{+-}(k, P) = -\phi_{-+}^*(k, P) \quad (3.22)$$

The vertex functions for the final vertex with  $(k, P) \rightarrow (k', P')$  will take the same form as the ones above with a few substitutions.

$$X \rightarrow X' = \frac{X - \zeta}{1 - \zeta}, \quad k_i \rightarrow \tilde{k}_i = k_i - \frac{1 - X}{1 - \zeta} \Delta_i, \quad i = 1, 2 \quad (3.23)$$

The soft helicity amplitudes are calculated by simple substitution. The vertex functions are evaluated, and then the integration is carried out in the  $k^- P^+$  complex plane. Furthermore, all constants are absorbed into a nor-

malization parameter  $\mathcal{N}$ , so that the helicity content is emphasized. In the DGLAP region with  $X > \zeta$ , with the spectator on shell after the contour integration is performed, the relevant soft helicity amplitudes take the following forms ( $n = 2$  for valence quarks,  $n = 3$  for sea quarks).

$$A_{++ , ++}^q = \int d^2 k_\perp \mathcal{A}^q(m_q + XM)(m_q + X'M) \quad (3.24)$$

$$A_{-+ , -+}^q = \int d^2 k_\perp \mathcal{A}^q(\tilde{k}_1 + i\tilde{k}_2)(k_1 - ik_2) \quad (3.25)$$

$$A_{-+ , ++}^q = \int d^2 k_\perp \mathcal{A}^q(m_q + XM)(\tilde{k}_1 + i\tilde{k}_2) \quad (3.26)$$

$$A_{++ , -+}^q = \int d^2 k_\perp \mathcal{A}^q(m_q + X'M)(k_1 - ik_2) \quad (3.27)$$

$$(3.28)$$

With the common factor

$$\mathcal{A}^q = \frac{\mathcal{N}^q}{\sqrt{XX'}P^+(1-X)} \frac{1}{(k^2 - M_\Lambda^2)^n (k'^2 - M_\Lambda^2)^n} \quad (3.29)$$

The soft amplitudes have useful relations based on equation (3.22), so all parton helicity conserving amplitudes can be calculated using the four given above. The two relevant relations for the GPDs are

$$A_{-- , +-}^q = -A_{++ , -+}^{*q} \quad (3.30)$$

$$A_{+- , +-}^q = A_{-+ , -+}^{*q} \quad (3.31)$$



### 3.3.2 Gluon Soft Amplitudes

The gluon vertex functions give the following results for a spin  $\frac{1}{2}$  spectator object.

$$\mathcal{G}_{+++}(k, P) = -\sqrt{\frac{2}{(1-X)}} \frac{(k_1 - ik_2)}{X} \frac{\Gamma^g(k)}{k^2 - m_g^2} \quad (3.32)$$

$$\mathcal{G}_{-++}(k, P) = -\sqrt{\frac{2}{(1-X)}} \left( M(1-X) - M_X \right) \frac{\Gamma^g(k)}{k^2 - m_g^2} \quad (3.33)$$

$$\mathcal{G}_{++-}(k, P) = 0 \quad (3.34)$$

$$\mathcal{G}_{-+-}(k, P) = -\sqrt{\frac{2}{(1-X)}} (1-X) \frac{(k_1 - ik_2)}{X} \frac{\Gamma^g(k)}{k^2 - m_g^2} \quad (3.35)$$

With the relations

$$\mathcal{G}_{---}(k, P) = -\mathcal{G}_{+++}^*(k, P) \quad (3.36)$$

$$\mathcal{G}_{+--}(k, P) = \mathcal{G}_{-++}^*(k, P) \quad (3.37)$$

$$\mathcal{G}_{--+}(k, P) = \mathcal{G}_{++-}^*(k, P) \quad (3.38)$$

$$\mathcal{G}_{+-+}(k, P) = -\mathcal{G}_{-+-}^*(k, P) \quad (3.39)$$

The vertex functions for the final vertex with  $(k, P) \rightarrow (k', P')$  will take the same form as the ones above with a few substitutions.

$$X \rightarrow X' = \frac{X - \zeta}{1 - \zeta}, \quad k_i \rightarrow \tilde{k}_i = k_i - \frac{1 - X}{1 - \zeta} \Delta_i, \quad i = 1, 2 \quad (3.40)$$

The soft helicity amplitudes are calculated in a similar way to the soft amplitudes for the quarks. The vertex functions are evaluated and combined by summing over the spectator's helicity states, and then the integration is carried out first in the  $k^- P^+$  complex plane. Furthermore, all constants are absorbed into a normalization constant  $\mathcal{N}$ , so that the helicity content is emphasized in the expression. In the DGLAP region with  $X > \zeta$ , with the spectator on shell after the contour integration is performed, the relevant soft helicity amplitudes take the following forms

$$\begin{aligned}
A_{++ , ++}^g &= \int d^2 k_\perp \mathcal{A}^g \left[ \left( (1-X)M - M_X \right) \left( (1-X')M - M_X \right) + \frac{(k_1 - ik_2)(\tilde{k}_1 + i\tilde{k}_2)}{XX'} \right] \\
A_{-+ , -+}^g &= \int d^2 k_\perp \mathcal{A}^g \left[ \frac{(1-X)(1-X')}{XX'} (k_1 - ik_2)(\tilde{k}_1 + i\tilde{k}_2) \right] \\
A_{-+ , ++}^g &= \int d^2 k_\perp \mathcal{A}^g \left[ \frac{(1-X')}{X'} \left( (1-X)M - M_X \right) (\tilde{k}_1 + i\tilde{k}_2) \right] \\
A_{++ , -+}^g &= \int d^2 k_\perp \mathcal{A}^g \left[ \frac{(1-X)}{X} \left( (1-X')M - M_X \right) (k_1 - ik_2) \right]
\end{aligned}$$

With the common factor

$$\mathcal{A}^g = \frac{\mathcal{N}^g}{\sqrt{1-X}\sqrt{1-X'}(1-X)P^+} \frac{1}{(k^2 - M_\Lambda^2)^2 (k'^2 - M_\Lambda^2)^2} \quad (3.41)$$

As with the soft helicity amplitudes for quarks, the remaining four gluon helicity conserving amplitudes can be related to the four helicity amplitudes above by using the gluon vertex function relations in equations (3.36)-(3.39).

### 3.4 Hard Helicity Amplitudes

The hard helicity amplitudes involve the subprocess  $(\gamma^* + q \rightarrow \gamma + q)$  for quarks, or  $(\gamma^* + g \rightarrow \gamma + g)$  for gluons. The factorized Compton Amplitude takes the following contribution in terms of the hard and soft subprocesses [8].

$$\int dXP^+ [Hard] \Big|_{\substack{k^-=0, k_\perp=0, \\ k'^-=0, k'_\perp=0}} \int d^2k_\perp \int dk^- [Soft] \quad (3.42)$$

where the soft and hard subprocesses are evaluated with  $k^+ = XP^+$ . This expression relates to the convolution integral of the soft and hard helicity amplitudes in the spectator model, and the connection will be discussed in section 3.5.

The hard helicity amplitudes are evaluated in the collinear limit with several approximations as discussed in chapter 2. The partons are evaluated on shell with no transverse or - light cone momentum components. The photons are also approximated as traveling exactly in the  $-\hat{z}$  direction. These approximations in the collinear limit give the dominant contribution to the hard helicity amplitudes, particularly for momentum components that are small on the order of  $Q$ . Also, with these approximations the hard helicity amplitudes have the following relations because of Parity conservation. For either quarks or gluons, all of the hard amplitudes used in this analysis have the following relations.

$$g_{++}^{++} = g_{--}^{--}, \quad g_{+-}^{--} = g_{-+}^{++} \quad (3.43)$$

### 3.4.1 Quark Hard Amplitudes LO

The hard subprocess ( $\gamma^* + q \rightarrow \gamma + q$ ) is solved in the DGLAP region with  $X > \zeta$ , in the Bjorken limit. As usual, the full expression for the scattering amplitude can be expanded into contributions from a series of Feynman diagrams. The leading contributions in terms of  $\alpha_s$  come at the Born level. In the  $\hat{s}$ -channel, the incoming virtual photon interacts with the incoming parton, which then emits the outgoing photon. In the crossed  $\hat{u}$ -channel, the interacting parton emits the outgoing photon, and then absorbs the incoming virtual photon.

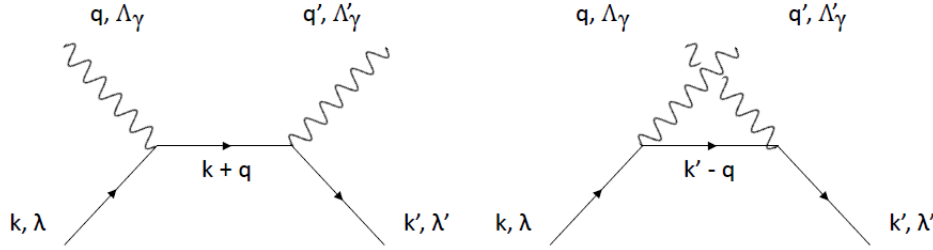


Figure 3.4: The LO amplitudes for the subprocess ( $\gamma^* + q \rightarrow \gamma + q$ ).

The full Compton amplitude expression for  $if_{\Lambda_\gamma, \Lambda; \Lambda'_\gamma, \Lambda'}$  is obtained by calculating soft and hard amplitudes strictly from Feynman rules and convoluting them according to the factorization theorem. In order to be consistent with equation (2.38), the hard helicity amplitudes are constructed by obtaining an expression entirely from standard Feynman rules, and then multiplying them

by a factor of  $-i$  by convention. The hard amplitude is given by

$$g_{\lambda,\lambda'}^{\Lambda_\gamma,\Lambda'_\gamma}(X,\zeta) = (-e^2 e_q^2) \left[ \bar{u}(k', \lambda') \gamma^\mu \gamma^+ \gamma^\nu u(k, \lambda) \right] q^- \left( \frac{\epsilon_\nu^{\Lambda_\gamma} \epsilon_\mu^{*\Lambda'_\gamma}}{\hat{s} + i\epsilon} - \frac{\epsilon_\nu^{*\Lambda'_\gamma} \epsilon_\mu^{\Lambda_\gamma}}{\hat{u} + i\epsilon} \right) \quad (3.44)$$

as the intermediate parton momentum is dominated in the Bjorken limit by

$$k + q \simeq q^- \gamma^+ \quad (3.45)$$

$$k' - q \simeq -q^- \gamma^+ \quad (3.46)$$

In the collinear limit, the photons will have the same helicity, and only parton helicity conserving amplitudes are considered. The only surviving terms are  $g_{++}^{++}$  because of the  $\hat{s}$ -channel, and  $g_{++}^{--}$  because of the  $\hat{u}$ -channel, along with their counterparts from equation (3.43). The hard amplitudes are combined in symmetric and antisymmetric combinations of the photon helicities. The subscript label  $(q, 0)$  indicates that the hard helicity amplitudes are associated with incoming and outgoing quarks, and that the amplitude is of order  $(\alpha_s)^0$ . In general, the letter in the label indicates the type of incoming and outgoing partons, with  $q$  for quarks,  $g$  for gluons, and  $\bar{q}$  for antiquarks. The number in the label indicates the order in  $\alpha_s$  for the amplitude.

$$g_{++}^S = g_{++}^{++} + g_{++}^{--} \quad g_{++}^A = g_{++}^{++} - g_{++}^{--} \quad (3.47)$$

The helicity amplitudes solve to the following:

$$g_{++(q,0)}^{++} \pm g_{++(q,0)}^{--} = \left( -e^2 e_q^2 \right) 2\sqrt{X(X-\zeta)} \left( \frac{1}{X-\zeta+i\epsilon} \pm \frac{1}{X-i\epsilon} \right) \quad (3.48)$$

The calculated hard helicity amplitudes involve on shell partons, and the full Compton amplitudes convolute the hard helicity amplitudes with the soft helicity amplitudes. This is in contrast to another method which calculates the Compton amplitudes from the handbag diagrams by using off-forward correlation functions [33]. In other words, the use of external quark spinors rather than a correlation function introduces kinematical factors to the hard helicity amplitudes that will need to be considered when calculating the GPDs. These extra kinematical factors will be discussed in section 3.5.

The next contributions to the hard subprocess  $(\gamma^* + q \rightarrow \gamma + q)$  are the amplitudes at NLO in  $\alpha_s$ . These will be discussed in the section 3.4.2, along with the NLO amplitudes for the subprocess  $(\gamma^* + g \rightarrow \gamma + g)$ .

### 3.4.2 NLO Quark and Gluon Hard Amplitudes

The next contributions to the hard subprocess  $(\gamma^* + q \rightarrow \gamma + q)$  after the Born level LO amplitudes are the NLO amplitudes at  $O(\alpha_s)$ . These NLO amplitudes involve one-loop corrections to the Born level amplitudes, and they are associated with eight Feynman diagrams. Four of the diagrams are displayed in figure 3.5, and the remaining four are identical to the four diagrams in the figure except that the outgoing photon is emitted from the initial vertex in-

stead of the incoming virtual photon being absorbed, and the incoming virtual photon is absorbed at the final vertex instead of the outgoing photon being emitted. Further symmetries reduce the total number of relevant diagrams from eight to six.

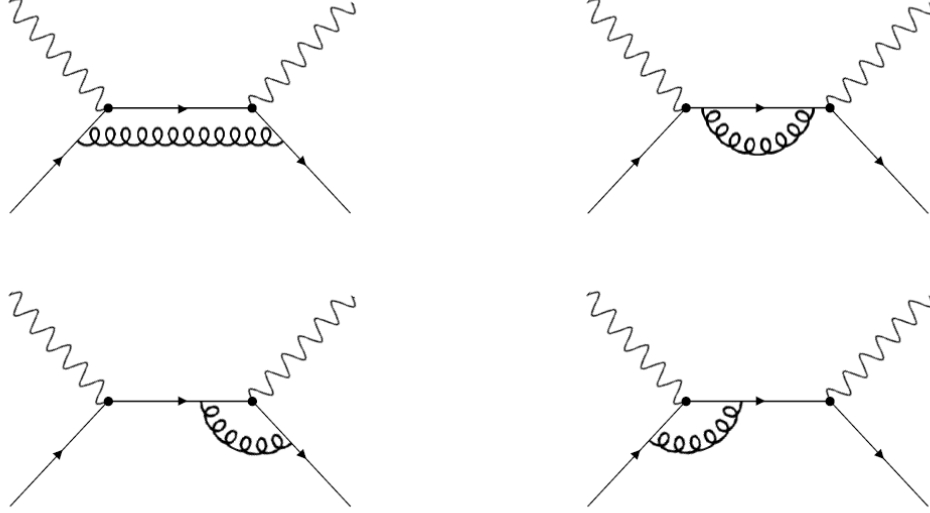


Figure 3.5: Four out of the eight NLO amplitudes for the subprocess  $(\gamma^* + q \rightarrow \gamma + q)$

There is no need to evaluate the quark one-loop amplitudes in the spectator model, because the GPDs can be solved for quarks using the LO hard amplitudes and the soft amplitudes. The NLO corrections to the handbag diagram for the Compton amplitude have also been evaluated by several groups, and the connection between the quark GPDs and the Compton Form Factors have been solved up to NLO. See [1], [21], and [30] for more details.

The subprocess  $(\gamma^* + g \rightarrow \gamma + g)$  has no corresponding LO amplitudes, but there are amplitudes at  $O(\alpha_s)$ . The gluons cannot interact directly with the photons, but instead they transition through an intermediate state involving a

quark-antiquark pair. The amplitudes at one-loop order are represented by six diagrams. Three of the diagrams are displayed in figure 3.6, and the remaining three are obtained by reversing the momentum flow in the intermediate loop for each of the three diagrams in the figure.

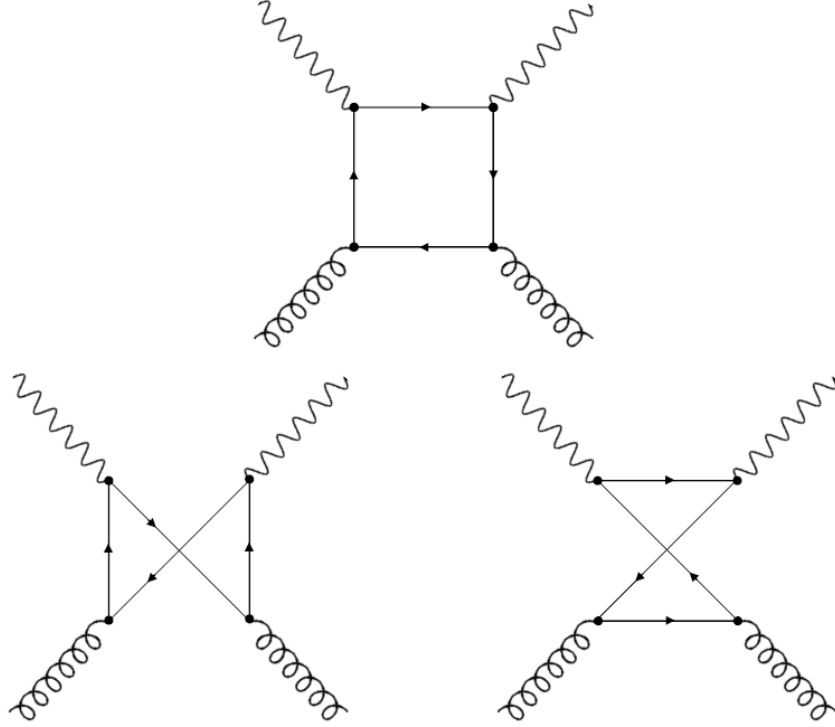


Figure 3.6: Three out of six NLO amplitudes for the subprocess  $(\gamma^* + g \rightarrow \gamma + g)$ . The remaining three are identical but with reversed momentum flow for the internal loop.

There is no need to evaluate the gluon one-loop amplitudes for the spectator model, but for different reasons than for quarks. Several groups have evaluated the gluon hard amplitudes at one-loop order. See references [1] and [29] for detailed explanations, keeping in mind their particular conventions. Rather than using external polarization vectors for the gluons and photons, they contract the indices for the photon-quark-antiquark vertices in symmetric and anti-



symmetric combinations, and similarly for gluons. For example, [29] discusses the evaluation of the symmetric part of one of the diagrams,  $g_T^{\mu\nu} g_T^{\alpha\beta} \mathcal{M}_{(1)\mu\nu\alpha\beta}$ , where  $\mathcal{M}_{(1)\mu\nu\alpha\beta}$  is the hard amplitude without external polarization vectors. The subscript (1) indicates that the amplitude is associated with the diagram labeled as (1) in [29]. The indices  $\mu$  and  $\nu$  are for the photon-quark-antiquark vertices, while  $\alpha$  and  $\beta$  are the indices for the gluon-quark-antiquark vertices. The resulting expressions are well documented.

For each of the diagrams for the subprocess  $(\gamma^* + g \rightarrow \gamma + g)$ , the symmetric and antisymmetric combinations of the hard parton helicity conserving amplitudes evaluated using the spectator model in the collinear limit give identical results to those using the methods in [29]. The gluons and photons are approximated as having no transverse momentum. The hard helicity amplitudes evaluated using the spectator model are defined as

$$g_{\Lambda_g, \Lambda'_g}^{\Lambda_\gamma, \Lambda'_\gamma}(X, \zeta) = \mathcal{M}_{(m)\mu\nu\alpha\beta} \epsilon_{\Lambda_g}^\alpha \epsilon_{\Lambda'_g}^{*\beta} \epsilon^{*\mu, \Lambda'_\gamma} \epsilon^{\nu, \Lambda_\gamma} \quad (3.49)$$

$(m)(g,1)$

where  $\mathcal{M}_{(m)\mu\nu\alpha\beta}$  can be any of the six amplitudes ( $m = 1, \dots, 6$ ) before contracting the vertices with the external polarization vectors. Recall the discussion in section 2.4.2 for more details about the symmetric and antisymmetric tensors  $g_T^{\mu\nu}$  and  $i\epsilon_T^{\mu\nu}$ , and their connection to the combinations of polarization vectors for quarks and gluons in the collinear limit. The combinations  $g_{\Lambda_g, \Lambda'_g}^{+,+} \pm g_{\Lambda_g, \Lambda'_g}^{-,-}$  will contract the indices  $\mu$  and  $\nu$  for  $\mathcal{M}_{(m)\mu\nu\alpha\beta}$  in symmetric or antisymmet-

$(m)(g,1)$        $(m)(g,1)$

ric combinations, just the same as the symmetric or antisymmetric tensors would up to a potential difference in the sign (+ or -). The combinations

$g_{+,+}^{\Lambda_\gamma, \Lambda'_\gamma} \pm g_{-,-}^{\Lambda_\gamma, \Lambda'_\gamma}$  will contract the indices  $\alpha$  and  $\beta$  in similar ways.

As a result, after combining hard parton helicity conserving amplitudes in the collinear limit and taking advantage of parity relations, it can be shown that the hard helicity amplitudes  $g_{++}^S$  can be solved for using the expressions in [29]. The amplitudes  $g_{++}^A$  could also be solved by repeating the analysis in [29] but with antisymmetric tensors replacing the appropriate symmetric tensors. Because of this, it is not necessary to calculate the hard amplitudes in the spectator model from scratch. Instead, it is simpler to start with the coefficient functions defined in [21], and to make the appropriate conversions in order to solve for the relevant combinations of the hard parton helicity conserving amplitudes in the spectator model.

There are two complications to consider. First, there is a kinematical factor that connects the gauge invariant gluon GPDs to the amplitudes in the  $A^+ = 0$  gauge. This will be discussed in the section 3.5. The next complication is that quark and gluon one-loop diagrams diverge. Essentially, the GPDs and the hard scattering amplitudes must be renormalized. Also, a factorization scale is introduced, and QCD (Quantum Chromodynamics) evolution becomes relevant.

### 3.5 Extra Kinematics

Recall from chapter 2 that the helicity amplitudes for DVCS at leading order in  $\frac{1}{Q}$  can be expressed as

$$f_{\Lambda_\gamma, \Lambda; \Lambda'_\gamma, \Lambda'} = \epsilon_\mu^{\Lambda_\gamma} T_{\Lambda\Lambda'}^{\mu\nu} \epsilon_\nu^{*\Lambda'_\gamma} \quad (3.50)$$

The amplitudes  $T_{\Lambda\Lambda'}^{\mu\nu}$  can be expanded, again at leading order in  $\frac{1}{Q}$ , in terms of symmetric and antisymmetric contributions with respect to the Lorentz indices. For photon helicity conserving interactions, neglecting photon helicity-flip terms and terms with longitudinal photon polarization, the amplitudes are expanded by the following expression.

$$T_{\Lambda\Lambda'}^{\mu\nu} = g_T^{\mu\nu} \mathcal{F}_{\Lambda, \Lambda'}^S + i \epsilon_T^{\mu\nu} \mathcal{F}_{\Lambda, \Lambda'}^A \quad (3.51)$$

The Compton Form Factors are expanded with the following coefficients

$$\mathcal{F}_{\Lambda, \Lambda'}^S = \int_{-1+\zeta}^1 \frac{dX}{1-\frac{\zeta}{2}} \left[ \sum_q F_{\Lambda, \Lambda'}^q (C_0^q + C_1^q + \dots) + F_{\Lambda, \Lambda'}^g (C_1^g + \dots) \right] \quad (3.52)$$

$$\mathcal{F}_{\Lambda, \Lambda'}^A = \int_{-1+\zeta}^1 \frac{dX}{1-\frac{\zeta}{2}} \left[ \sum_q \tilde{F}_{\Lambda, \Lambda'}^q (\tilde{C}_0^q + \tilde{C}_1^q + \dots) + \tilde{F}_{\Lambda, \Lambda'}^g (\tilde{C}_1^g + \dots) \right] \quad (3.53)$$

Where the subscript  $n$  in the coefficients  $C_n^{q(g)}$  and  $\tilde{C}_n^{q(g)}$  indicates that the coefficient is of the order  $O(\alpha_s^n)$ . The distributions  $F_{\Lambda, \Lambda'}^{q(g)}$  and  $\tilde{F}_{\Lambda, \Lambda'}^{q(g)}$  are the generalized distributions for quarks (gluons), with specified helicity states for the initial and final state hadrons. See [21] for a discussion of the coefficients

at up to NLO, keeping in mind any differences in convention from the one used in this analysis. Conventions may differ in many ways. In particular, the sign (+ or  $-$ ) in front of each term might vary between conventions. Conventions may also differ in which terms contain powers of the elementary charge ( $e$ ), as well as in which terms contain powers of the quark charges ( $e_q$ ).

The Compton scattering helicity amplitudes can be expressed either in terms of combinations of ordinary helicity amplitudes, or in terms of GPDs. This creates a connection between the ordinary helicity amplitudes evaluated using the spectator model and the GPDs. The GPDs can be solved from these helicity amplitudes at  $O(\alpha_s^n)$ , for any particular order  $n$ . For example, in the case that the initial and final state hadrons have helicities indicated by the labels ( $\Lambda = +$ ) and ( $\Lambda' = +$ ), the following expressions relate the helicity amplitudes to the GPDs.

$$f_{+,+}^S = g_{+,+}^S \otimes \left( A_{+,+,++}^{q(g)} + A_{+,-,+}^{q(g)} \right) = -2 \int_{-1+\zeta}^1 \frac{dX}{1-\frac{\zeta}{2}} F_{+,+}^{q(g)} C_n^{q(g)} \quad (3.54)$$

$$f_{+,+}^A = g_{+,+}^A \otimes \left( A_{+,+,++}^{q(g)} - A_{+,-,+}^{q(g)} \right) = -2 \int_{-1+\zeta}^1 \frac{dX}{1-\frac{\zeta}{2}} \tilde{F}_{+,+}^{q(g)} \tilde{C}_n^{q(g)} \quad (3.55)$$

for quarks of flavor  $q$  (or for gluons), where the order of  $\alpha_s$  is implicit wherever it is not labeled. There are similar expressions involving other combinations of helicities for the initial and final state hadrons.

Essentially, there are two methods for evaluating each Compton amplitude, and both methods involve an integral in  $X$  over the same range. The integrand of one method can be compared to the integrand of the other, so that factors

in common can be identified. Furthermore, the  $C_n^{q(g)}$  and  $\tilde{C}_n^{q(g)}$  coefficients can be chosen to match the expressions defined by other groups, such as the expressions in [21], after adjusting for differences between conventions. This ensures that the GPDs solved for in this analysis correspond to the GPDs as defined by these other groups. After removing the factors in common from the integrands, the generalized quark and gluon distributions, and with them the GPDs, can be expressed in terms of combinations of the soft ordinary helicity amplitudes along with any remaining kinematical factors.

In this analysis, the extra kinematical factors for quarks and gluons are proportional to

$$\begin{aligned} [\text{E.K.}]^q &\sim \sqrt{X(X-\zeta)}P^+ \\ [\text{E.K.}]^g &\sim \frac{X(X-\zeta)P^+}{1-\frac{\zeta}{2}} \end{aligned} \tag{3.56}$$

where constant factors are omitted because they will be absorbed into the normalization parameters of the GPDs. New soft helicity amplitudes are defined by absorbing the extra kinematical factors into the original soft helicity amplitudes. These new amplitudes are labeled as  $A'_{\Lambda',\lambda';\Lambda,\lambda}{}^q$  for any quark flavor  $q$ , with similar expressions for gluons using a superscript label of  $g$  instead of  $q$ . For any single quark flavor,  $q$ , or for gluons, these new soft amplitudes are

expressed in terms of the GPDs in the following way.

$$\begin{aligned}
A'_{++,++} &= \frac{\sqrt{1-\zeta}}{1-\frac{\zeta}{2}} \left( \frac{H^{(sp)} + \tilde{H}^{(sp)}}{2} - \frac{\zeta^2}{4(1-\zeta)} \frac{E^{(sp)} + \tilde{E}^{(sp)}}{2} \right) \\
A'_{-+,-+} &= \frac{\sqrt{1-\zeta}}{1-\frac{\zeta}{2}} \left( \frac{H^{(sp)} - \tilde{H}^{(sp)}}{2} - \frac{\zeta^2}{4(1-\zeta)} \frac{E^{(sp)} - \tilde{E}^{(sp)}}{2} \right) \\
A'_{++,-+} &= \frac{\Delta_1 - i\Delta_2}{4M\sqrt{1-\zeta}} \left( E^{(sp)} - \frac{\zeta}{2(1-\frac{\zeta}{2})} \tilde{E}^{(sp)} \right) \\
A'_{-+,,} &= \frac{\Delta_1 + i\Delta_2}{4M\sqrt{1-\zeta}} \left( -E^{(sp)} - \frac{\zeta}{2(1-\frac{\zeta}{2})} \tilde{E}^{(sp)} \right) \tag{3.57}
\end{aligned}$$

where the GPDs have the label  $(sp)$  to indicate that these are not the final GPD expressions, but rather they are the contributions from the spectator model amplitudes. All quark and gluon labels ( $q$  or  $g$ ) have been omitted for simplicity. These expressions were evaluated in the asymmetric frame. In this frame, the initial proton has no transverse momentum. The phase of the azimuthal angle of the vector  $D$  is just the phase of the azimuthal angle of  $P'$ . It is convenient to rework the expressions above into the following expressions.

$$A'_{++,++} - A'_{-+,-+} = \frac{\sqrt{1-\zeta}}{1-\frac{\zeta}{2}} \tilde{H}^{(sp)} + \frac{-\frac{\zeta^2}{4}}{(1-\frac{\zeta}{2})\sqrt{1-\zeta}} \tilde{E}^{(sp)} \tag{3.58}$$

$$A'_{++,++} + A'_{-+,-+} = \frac{\sqrt{1-\zeta}}{1-\frac{\zeta}{2}} H^{(sp)} + \frac{-\frac{\zeta^2}{4}}{(1-\frac{\zeta}{2})\sqrt{1-\zeta}} E^{(sp)} \tag{3.59}$$

$$-\frac{\Delta_1 - i\Delta_2}{\Delta_\perp^2} A'_{-+,,} - \frac{\Delta_1 + i\Delta_2}{\Delta_\perp^2} A'_{++,-+} = \frac{\zeta}{2(1-\frac{\zeta}{2})\sqrt{1-\zeta}} \frac{1}{2M} \tilde{E}^{(sp)} \tag{3.60}$$

$$-\frac{\Delta_1 - i\Delta_2}{\Delta_\perp^2} A'_{-+,,} + \frac{\Delta_1 + i\Delta_2}{\Delta_\perp^2} A'_{++,-+} = \frac{1}{\sqrt{1-\zeta}} \frac{1}{2M} E^{(sp)} \tag{3.61}$$

where all quark and gluon labels have again been omitted for simplicity. The final GPD models are evaluated starting with these expressions. The final

GPD expressions also involve the inclusion of normalization parameters, as well as the inclusion of a Regge term that will be discussed in section 3.6.

### 3.6 Regge Term

The GPDs derived from the spectator model each require an additional Regge term in order to adequately fit DIS data. The Regge term impacts the low  $X$  region most significantly, although it still has contributions at mid to high  $X$  values. The Reggeized GPDs are obtained by multiplying the expressions obtained from the spectator model by a Regge term of the general form

$$R = X^{-[\alpha + \alpha'(1-X)^p t + \beta(\zeta)t]} \quad (3.62)$$

where the parameters  $\alpha$ ,  $\alpha'$ , and  $p$  can vary for each GPD. For this analysis,  $\beta(\zeta)$  is set to 0. In the forward limit, the term takes the desired form  $X^{-\alpha}$ . The  $t$ -dependent term with  $\alpha'$  is included so that after a Fourier transformation in  $\vec{\Delta}_\perp$ , the nucleon radius is finite as  $X \rightarrow 1$ . See [13] for a discussion of GPD properties as they evolve in  $Q^2$ .

The inclusion of the Regge term is motivated by a generalization of the spectator model, in which the spectator's mass has a spectral distribution instead of a single fixed value. In the forward limit, it can be shown that if a GPD without the Regge term is multiplied by an appropriate spectral distribution  $\rho(M_X^2)$  and then an integral is performed over all possible  $M_X^2$ ,

the result will have the desired low  $X$  behavior. The purpose of the Regge term is to influence the  $X$  behavior of the GPDs in a way that is consistent with what would be obtained by instead applying the spectral distribution and integrating over all possible  $M_X^2$  values. See [34] for a more detailed discussion.

### 3.7 GPDs

The full GPD expressions are listed in this section. It is convenient to first create yet another set of distributions

$$F_q^{(sp)} = \mathcal{N}^q N^q F_q^{(h)}, \quad F_g^{(sp)} = \mathcal{N}^g N^g F_g^{(h)} \quad (3.63)$$

where  $F = H, E, \tilde{H}$ , or  $\tilde{E}$ , and  $\mathcal{N}^q$  is the constant in equation 3.29 while  $\mathcal{N}^g$  is the constant in equation 3.41. There are constant factors from other sources, such as the hard amplitudes or the extra kinematical factors, that were not absorbed into  $\mathcal{N}^q$  or  $\mathcal{N}^g$ . For a particular quark flavor,  $q$ , all remaining constants that the four parton helicity conserving GPDs have in common are gathered into the constant  $N^q$ . Similarly, all remaining constants that the four parton helicity conserving gluon GPDs have in common are gathered into the constant  $N^g$ . The  $F^{(sp)}$  distributions are the GPDs in equations 3.58 to 3.61. The  $F^{(h)}$  distributions are created to emphasize the variable content of the GPDs, separated from any constant factors that each of the four parton helicity conserving GPDs have in common for a particular parton type and



flavor.

The expressions for the soft helicity amplitudes and GPDs involve integrals in terms of the transverse components of the four-momentum  $k$ . The transverse part of  $k$  forms the transverse vector  $\vec{k}_\perp$ , which has an azimuthal angle of  $\phi_k$  and a magnitude of  $k_\perp$ . The following notation is used for the integrals.

$$\int d^2k_\perp f(k_\perp, \phi_k) = \int_0^{2\pi} d\phi_k \int_0^\infty k_\perp dk_\perp f(k_\perp, \phi_k) \quad (3.64)$$

where  $f(k_\perp, \phi_k)$  is any function of these two variables. It should be noted that, while the GPDs are real distributions, the integrands may contain imaginary terms resulting from the following expressions

$$(k_1 \pm ik_2)(\Delta_1 \mp i\Delta_2) = k_\perp \Delta_\perp \cos(\phi) \pm ik_\perp \Delta_\perp \sin(\phi) \quad (3.65)$$

where  $\phi \equiv \phi_k - \phi_\Delta$  is the azimuthal angle between  $\vec{k}_\perp$  and  $\vec{\Delta}_\perp$ , with  $\phi_\Delta$  as the azimuthal angle of the four-momentum  $\Delta$ . For fixed  $\phi_\Delta$ , or simply by defining  $\Delta_2 = 0$  with no loss in generality, the integral over  $\phi_k$  in equation 3.64 can be replaced by

$$\int_0^{2\pi} d\phi_k \rightarrow \int_0^{2\pi} d\phi \quad (3.66)$$

with no change in the result. It can be shown that the terms proportional to  $i \sin(\phi)$  integrate to 0. In this way, the imaginary terms drop out after integration, and only the real terms remain.

The quark GPDs are given by

$$H_q^{(h)} = \frac{\zeta^2}{4(1-\zeta)} E_q^{(h)} + \int d^2 k_\perp \frac{(1-\frac{\zeta}{2})}{1-X} \frac{[(m_q + MX)(m_q + M \frac{X-\zeta}{1-\zeta}) + \vec{k}_\perp \cdot \vec{\tilde{k}}_\perp]}{(k^2 - M_\Lambda^2)^n (k'^2 - M_\Lambda^2)^n}$$

$$E_q^{(h)} = \int d^2 k_\perp \frac{(-2M)(1-\zeta)}{1-X} \frac{[(m_q + MX) \frac{\vec{k}_\perp \cdot \vec{\tilde{\Delta}}_\perp}{\Delta_\perp^2} - (m_q + M \frac{X-\zeta}{1-\zeta}) \frac{\vec{k}_\perp \cdot \vec{\tilde{\Delta}}_\perp}{\Delta_\perp^2}]}{(k^2 - M_\Lambda^2)^n (k'^2 - M_\Lambda^2)^n}$$

$$\tilde{H}_q^{(h)} = \frac{\zeta^2}{4(1-\zeta)} \tilde{E}_q^{(h)} + \int d^2 k_\perp \frac{(1-\frac{\zeta}{2})}{1-X} \frac{[(m_q + MX)(m_q + M \frac{X-\zeta}{1-\zeta}) - \vec{k}_\perp \cdot \vec{\tilde{k}}_\perp]}{(k^2 - M_\Lambda^2)^n (k'^2 - M_\Lambda^2)^n}$$

$$\tilde{E}_q^{(h)} = \int d^2 k_\perp \frac{2(1-\frac{\zeta}{2})}{\zeta} \frac{(-2M)(1-\zeta)}{1-X} \frac{[(m_q + MX) \frac{\vec{k}_\perp \cdot \vec{\tilde{\Delta}}_\perp}{\Delta_\perp^2} + (m_q + M \frac{X-\zeta}{1-\zeta}) \frac{\vec{k}_\perp \cdot \vec{\tilde{\Delta}}_\perp}{\Delta_\perp^2}]}{(k^2 - M_\Lambda^2)^n (k'^2 - M_\Lambda^2)^n}$$

where  $n = 2$  for valence quarks, and  $n = 3$  for sea quarks. The full GPD expressions include a Regge term and a normalization factor. For any valence or sea quark GPD labeled as  $F$ , the full form is given by

$$F = \mathcal{N}_F R_F F^{(h)} \quad (3.67)$$

where  $\mathcal{N}_F$  is a new parameter that scales the GPD,  $R_F$  is the Regge term with the form defined in section 3.6, the label  $F = H, E, \tilde{H}$ , or  $\tilde{E}$ , and the quark labels have been omitted for simplicity.

The gluon GPDs are given by

$$H_g^{(h)} = \frac{\zeta^2}{4(1-\zeta)} E_g^{(h)} + \int d^2 k_\perp \frac{1}{(1-X)^2} \\ \times \frac{[X(X-\zeta)\left((1-X)M - M_X\right)\left(\left(\frac{1-X}{1-\zeta}\right)M - M_X\right) + (1-\zeta)\left(1 + \frac{(1-X)^2}{1-\zeta}\right)\vec{k}_\perp \cdot \vec{k}_\perp]}{(k^2 - M_\Lambda^2)^2(k'^2 - M_\Lambda^2)^2}$$

$$E_g^{(h)} = \int d^2 k_\perp \frac{(-2M)(1-\zeta)}{(1-X)} \frac{1}{(1-\zeta/2)} \\ \times \frac{[X\left((1-X)M - M_X\right)\frac{\vec{k}_\perp \cdot \vec{\Delta}_\perp}{\Delta_\perp^2} - (X-\zeta)\left(\left(\frac{1-X}{1-\zeta}\right)M - M_X\right)\frac{\vec{k}_\perp \cdot \vec{\Delta}_\perp}{\Delta_\perp^2}]}{(k^2 - M_\Lambda^2)^2(k'^2 - M_\Lambda^2)^2}$$

$$\tilde{H}_g^{(h)} = \frac{\zeta^2}{4(1-\zeta)} \tilde{E}_g^{(h)} + \int d^2 k_\perp \frac{1}{(1-X)^2} \\ \times \frac{[X(X-\zeta)\left((1-X)M - M_X\right)\left(\left(\frac{1-X}{1-\zeta}\right)M - M_X\right) + (1-\zeta)\left(1 - \frac{(1-X)^2}{1-\zeta}\right)\vec{k}_\perp \cdot \vec{k}_\perp]}{(k^2 - M_\Lambda^2)^2(k'^2 - M_\Lambda^2)^2}$$

$$\tilde{E}_g^{(h)} = \int d^2 k_\perp \frac{2}{\zeta} \frac{(-2M)(1-\zeta)}{(1-X)} \\ \times \frac{[X\left((1-X)M - M_X\right)\frac{\vec{k}_\perp \cdot \vec{\Delta}_\perp}{\Delta_\perp^2} + (X-\zeta)\left(\left(\frac{1-X}{1-\zeta}\right)M - M_X\right)\frac{\vec{k}_\perp \cdot \vec{\Delta}_\perp}{\Delta_\perp^2}]}{(k^2 - M_\Lambda^2)^2(k'^2 - M_\Lambda^2)^2}$$

The full GPD expressions include a Regge term and a normalization factor.

For any gluon GPD labeled as  $F$ , the full form is given by

$$F = \mathcal{N}_F R_F F^{(h)} \quad (3.68)$$

where  $\mathcal{N}_F$  is a new parameter that scales the GPD,  $R_F$  is the Regge term with the form defined in section 3.6,  $F = H, E, \tilde{H}$ , or  $\tilde{E}$ , and the gluon labels have been omitted for simplicity.

### 3.7.1 Parametrization

The leading twist, helicity conserving GPD expressions in the DGLAP region with  $X > \zeta$  have been defined for valence quarks, sea quarks, and gluons. In this analysis, we have included three quark flavors ( $q = u, d, s$ ) as well as gluons ( $g$ ). It should be noted that, depending on the  $x$  region, the partonic interpretation for a given full quark GPD expression of a particular flavor involves interacting quarks and antiquarks in different combinations. The label  $q_V$  represents the contribution from terms involving interacting valence quarks to the full GPD of flavor  $q$ . Similarly, the  $q_{sea}$  and  $\bar{q}$  labels indicate the contributions from the terms involving interacting sea quarks (not including sea antiquarks) and antiquarks, respectively, to the full GPD of flavor  $q$ .

For example,  $H_u$  has contributions from the  $H_{u_V}$ ,  $H_{u_{sea}}$ , and  $H_{\bar{u}}$  distributions.  $H_{u_V}$  and  $H_{u_{sea}}$  contribute in the DGLAP region with  $x > \xi$ , while  $H_{\bar{u}}$  contributes in the DGLAP region with  $x < -\xi$ . The ERBL region is more complicated, because the partonic interpretation for the GPD expressions involves an interacting antiquark and an interacting quark. In this analysis, it is sufficient to use a parametrization for the full GPD expression in the ERBL region without separating the contributions from quarks and antiquarks.

Assuming there are no strange valence quarks, this analysis has six relevant parton types ( $u_V$ ,  $d_V$ ,  $u_{sea}$ ,  $d_{sea}$ ,  $s_{sea}$ , and  $g$ ) with four GPDs each in the DGLAP region with  $X > \zeta$ , not counting the antiquark distributions which are all 0 over this region. Each of these 24 total distributions has its own unique set of values for the following parameters:

$$m, M_X, M_\Lambda, \alpha, \alpha', p, \mathcal{N} \quad (3.69)$$

where the parameter  $m$  represents the quark mass  $m_q$  for quark GPDs and the gluon mass  $m_g$  for gluon GPDs. The gluon mass has been set to  $m_g = 0$  for this analysis. The parameter  $\mathcal{N}$  represents the parameters labeled by  $\mathcal{N}_F$  in equations 3.67 and 3.68. The parametric forms of the GPDs allow for flexibility when fitting to data.

### 3.8 ERBL and DGLAP ( $x < -\xi$ ) Regions

The quark and gluon GPDs have been evaluated in the DGLAP region with  $X > \zeta$ , or  $x > \xi$ . The full GPDs extend all the way down to  $x = -1$ , and so the GPDs must be evaluated in the remaining  $x$  regions. The quark GPDs are simple to evaluate using the spectator model in the DGLAP region with  $x < -\xi$ . The soft amplitudes in this region involve two interacting antiquarks. It is not necessary to calculate the helicity amplitudes in the DGLAP region with  $x < -\xi$  from scratch using the framework of the spectator model. The

quark GPDs in the region  $x < -\xi$  can be evaluated by relating them to the sea quark amplitudes that are calculated in the region  $x > \xi$ . The gluon GPDs are each either entirely odd or even in  $x$ , so it is simple to evaluate the gluon GPDs in one DGLAP region if they have already been evaluated in the other.

The quark and gluon GPDs could potentially be modeled in the ERBL region using the spectator model, with  $(0 < X < \zeta)$  or equivalently  $(-\xi < x < \xi)$ . The amplitudes associated with the quark GPDs would involve an interacting quark and an interacting antiquark in the ERBL region, as opposed to two quarks in the DGLAP region with  $X > \zeta$ . Also, contour integration puts a parton on shell and the spectator off shell in the ERBL region. At the moment, the quark GPDs in the ERBL region are modeled instead by a functional polynomial parametrization. The functional forms preserve the property of polynomiality, as well as continuity at the crossover points of  $X = 0$  and  $X = \zeta$ .

For any quark GPD,  $F_q = H_q, E_q, \tilde{H}_q, \text{ or } \tilde{E}_q$ , it is useful to define a symmetric and an antisymmetric function about  $x = 0$  or  $X = \frac{\zeta}{2}$  with the properties

$$\begin{aligned} F_q^-(x, \xi, t) &= F_q^-(-x, \xi, t) \\ F_q^+(x, \xi, t) &= -F_q^+(-x, \xi, t) \end{aligned}$$

Note that these functions are not to be confused with the "singlet" and "nonsinglet" distributions defined in section 1.5. The symmetric and antisymmetric functions are presented in the asymmetric frame with the following forms based

on [31]

$$F^-(X, \zeta, t) = a^-(\zeta, t)X^2 - a^-(\zeta, t)\zeta X + b(\zeta, t) \quad (3.70)$$

$$F^+(X, \zeta, t) = a^+(\zeta, t)X^3 - \frac{3}{2}a^+(\zeta, t)\zeta X^2 + c(\zeta, t)X + d(\zeta, t) \quad (3.71)$$

where the quark labels have been omitted for simplicity. The  $\pm$  superscript labels for the functions  $F^\pm$  indicate whether each function is symmetric or antisymmetric in the  $X$  coordinate about  $X = \frac{\zeta}{2}$ . These are not the same as the  $(\pm)$  "singlet" and "nonsinglet" GPD combinations, although it is possible to relate the different schemes. For fixed  $\zeta$  and  $t$ , the functions  $b$  and  $d$  are obtained by considering the GPDs evaluated in the DGLAP regions at the boundaries of  $F_q(0, \zeta, t)$  and  $F_q(\zeta, \zeta, t)$ . Next, some of the other terms can be evaluated in a sequential process. For example, the function  $a^-$  for the full GPD  $H_q$  can be evaluated by integrating the GPD with respect to  $x$ . The resulting expression, which will be in terms of  $a^-$ , can then be related to the form factor  $\mathcal{F}_1^q(t) = \int_{-1}^1 dx H_q(x, \zeta, t)$  to solve for  $a^-$ . Other terms are not fit, but are instead left as free parameters which depend on  $\zeta$  and  $t$ . The gluon GPDs could also be expressed in the ERBL region by using functional polynomial forms. The functional forms could be similar to the forms used for quarks, with the additional constraint that each gluon GPD is either even or odd in  $x$ .

At this point, the full gluon GPDs as well as the full quark GPDs for the flavors  $q = u, d, s$  have been modeled over the entire region from  $x = -1$  to

$x = 1$ . The parameters for the up and down valence quark GPDs have been fit previously [33] [34]. Using these fit results, many parameters for the sea quark, antiquark, and gluon GPDs can be fit as well. Chapter 4 describes the procedure for fitting several parameters, and presents the results of the initial fits.



# Chapter 4

## GPD Fit Results

### 4.1 Fit Results

The full recursive fit procedure involves many steps. The full set of parameters is not obtained all at once. Instead, a subset of parameters is obtained in the first step, then they are held fixed while another subset is obtained in the second step, and so on until all parameters are set. This section describes the first step of the recursive fit procedure. For this stage, the GPDs are reduced to their PDF functional forms by setting  $t = 0, \zeta = 0$  in our GPDs' model equations. The PDF forms were evolved from their initial scales to a final  $Q^2$  value using perturbative QCD (pQCD) evolution equations, as elaborated in more detail below, and then fit to an established PDF parametrization.

First, our PDF forms for up and down valence quarks were fitted at  $Q_0^2 = 0.09362 \text{ GeV}^2$  using the parameters in [31]. The valence distributions were used as input values for the DGLAP evolution equations at leading order (LO) in

x-space and evolved up to the initial scale for the sea quark and gluon PDFs,  $Q_{0sea}^2$ . We then included our up, down, and strange sea quark PDFs as well as our gluon PDF at this scale and evolved all distributions to the final scale of  $Q^2 = 25 \text{ GeV}^2$  by solving the LO DGLAP evolution equations.

At the evolved scale of  $25 \text{ GeV}^2$ , the sea quark and gluon distributions are fit to PDF parametrizations for Alekhin 2002 (set a02m\_lo). We fit expressions for  $X$  times our evolved PDF forms to Alekhin's distributions for  $X\bar{u}(X)$ ,  $X\bar{d}(X)$ ,  $X\bar{s}(X)$ , and  $Xg(X)$ . This was achieved by selecting a set of  $X$  points, and comparing our expressions to Alekhin's distributions at those points. We fit each of the four distributions separately, using the same set of  $X$  values for each distribution. We included error values for Alekhin's distributions equal to half of the error provided in set a02m\_lo in order to weigh the fit, and emphasize different  $X$  regions. If any of these error values (half of the error for a02m\_lo) were below 0.005, we used the value 0.005 instead. There is a separate  $\chi^2$  contribution from each distribution, and the total  $\chi^2$  is minimized.

The initial scale for the sea quark and gluon PDFs,  $Q_{0sea}^2$ , is an additional parameter. We chose to perform two separate fits, one using a value of  $0.5 \text{ GeV}^2$  and the other using  $0.7 \text{ GeV}^2$ . Each fit resulted in values for  $m_q$  for the antiquark H distributions, as well as  $M_X$ ,  $M_\Lambda$ ,  $\alpha$ , and the normalization factors,  $\mathcal{N}$ , for the antiquark and gluon H distributions. The tables below list the parameter values for each fit. The tables also list the  $\chi^2/N_{points}$  values for each parton, where  $N_{points}$  is the number of  $X$  points for each separate contribution to the fit.

Parameter	$\bar{u}$	$\bar{d}$	$\bar{s}$	gluon
$m_q$ (GeV)	0.78931	0.61690	1.2428	—
$\mathcal{N}$	0.41874	0.30094	0.70544	0.51936
$\alpha$	1.1243	1.1435	0.48488	-0.91492
$M_X$ (GeV)	1.7644	1.2136	2.4789	1.0043
$M_\Lambda$ (GeV)	1.0067	1.0059	1.0597	0.52322
$\chi^2/N_{points}$	0.066	0.333	0.119	1.769

Table 4.1: Parameter Values  $Q_{0sea}^2 = 0.5 \text{ GeV}^2$

Parameter	$\bar{u}$	$\bar{d}$	$\bar{s}$	gluon
$m_q$ (GeV)	0.74765	0.84101	0.46183	—
$\mathcal{N}$	0.32504	1.1107	0.71087	2.5721
$\alpha$	1.1685	1.1831	1.0291	-0.73921
$M_X$ (GeV)	1.6797	1.2499	1.6861	1.7040
$M_\Lambda$ (GeV)	0.99735	1.2311	1.2188	0.61225
$\chi^2/N_{points}$	0.030	0.048	0.008	0.185

Table 4.2: Parameter Values  $Q_{0sea}^2 = 0.7 \text{ GeV}^2$

## 4.2 Plots with $\zeta = 0, t = 0$

The results of the fit are discussed below. In the next few sections of this chapter, the GPDs are reduced to their functional PDF forms by setting  $\zeta = 0, t = 0$ . First, the results are discussed at the initial scale for the sea quarks and gluons. Next, the results are discussed at a scale of  $Q^2 = 25 \text{ GeV}^2$  and compared with Alekhin's distributions that were used in the fit procedure. The discussion shows that there is good agreement between the fit results and Alekhin's distributions. Finally, the results are discussed at a range of intermediate  $Q^2$  values.

### 4.3 Distributions at the Initial Scale

Here is a discussion of the fit results at the initial scale for sea quarks and gluons. Recall that there are two sets of parameters, one with  $Q_{0sea}^2 = 0.5$  GeV<sup>2</sup> and the other with  $Q_{0sea}^2 = 0.7$  GeV<sup>2</sup>. One set of distributions is obtained at  $Q_{0sea}^2 = 0.5$  GeV<sup>2</sup> by inserting the parameters in Table 4.1 into the model equations for the PDF functional forms of the gluons and the up, down, and strange antiquarks. Another set of distributions is obtained at  $Q_{0sea}^2 = 0.7$  GeV<sup>2</sup> by using the parameters in Table 4.1 instead. Figure 4.1 shows the two sets of distributions for  $XH_u(X, 0, 0)$ ,  $XH_{\bar{d}}(X, 0, 0)$ ,  $XH_{\bar{s}}(X, 0, 0)$ , and  $H_g(X, 0, 0)$ . Each distribution is shown at its own initial scale, so that every parton has a distribution at  $Q^2 = 0.5$  GeV<sup>2</sup> and another at  $Q^2 = 0.7$  GeV<sup>2</sup>.

As a reminder, the GPDs reduce to PDF functional forms in slightly different ways for quarks and gluons.

$$H_q(X, 0, 0) \rightarrow q(X) \tag{4.1}$$

$$H_g(X, 0, 0) \rightarrow Xg(X) \tag{4.2}$$

for  $X > 0$ . Note the power of  $X$  difference for gluons. Also, the sea quark distributions for quarks and antiquarks of the same flavor are treated as equal.

Using asymmetric coordinates:

$$q_{sea}(X) = \bar{q}(X), \quad q = u, d, s \tag{4.3}$$

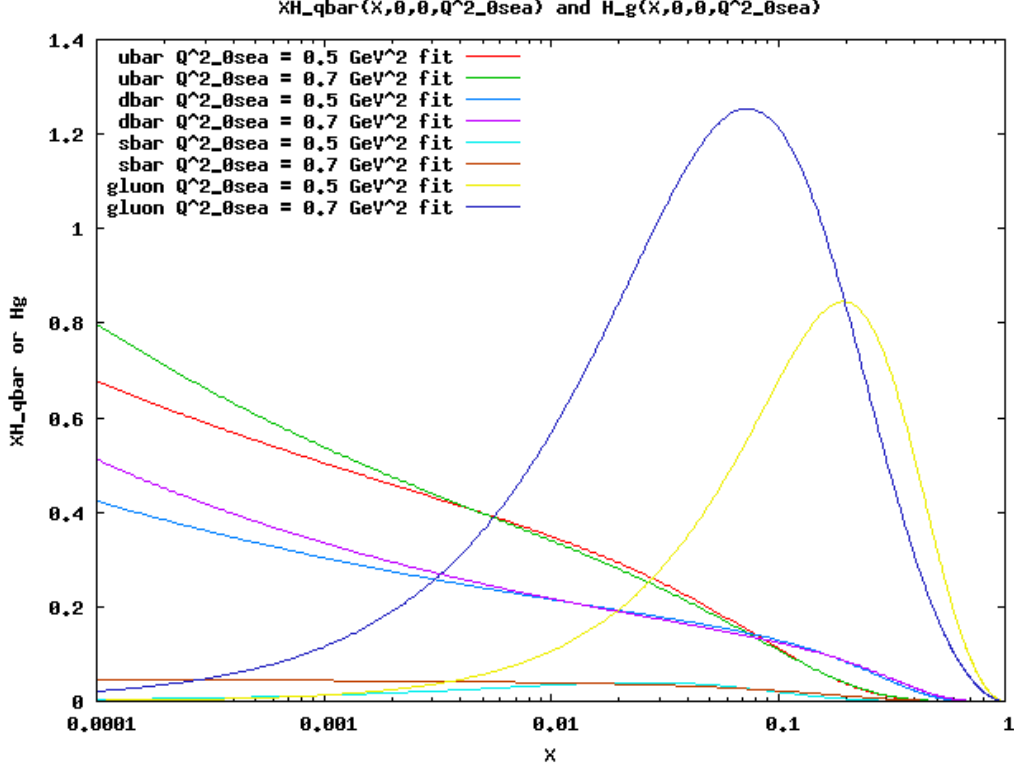


Figure 4.1: The plot above shows the PDF functional forms for the two sets of fit distributions at their initial scales. There are two sets of parameters, one with  $Q_{0sea}^2 = 0.5 \text{ GeV}^2$  and the other with  $Q_{0sea}^2 = 0.7 \text{ GeV}^2$ . Each distribution is plotted at the  $Q^2$  value listed in the legend, corresponding to the initial scale for sea quarks and gluons used in the fit procedure.

Figure 4.1 shows many key features of the antiquark and gluon distributions  $Xf(X)$ , where  $f(X)$  is the PDF functional form of the GPDs ( $f(X) = \bar{q}(X)$ ,  $g(X)$ ). At these low scales, the up and down antiquark distributions rise as  $X$  decreases towards 0, indicating that the up and down antiquarks are more likely to carry a smaller fraction of the proton's momentum along the light cone. These distributions are roughly comparable in size and shape, with a slight bump at mid  $X$  and a drop to 0 as  $X$  approaches 1. The strange antiquark distributions have lower values than the other antiquarks at most  $X$  values, indicating that there is less of a chance of observing a strange antiquark

with those fractions of the proton's momentum along the light cone than for up and down antiquarks.

The gluon distributions peak at mid  $X$  values, and then decrease again towards lower  $X$  values, indicating that at these  $Q^2$  values the gluons are most likely to carry a low to moderate fraction of the proton's momentum along the light cone. The curves are valence-like, in a sense that they have similar overall shapes and trends as up and down valence quark distributions do at low  $Q^2$  values. This is not wholly unexpected, and there will be a detailed discussion later in this chapter about the gluon distributions at higher scales. For now, it is worthwhile to discuss the trends at very low  $Q^2$ . At the initial scale for valence quarks, ideally the valence quark PDFs will dominate and the sea quark PDFs will be low or zero. In other words, the proton interacts as if it was entirely composed of three valence quarks and no sea quarks. As the scale rises, the proton interacts as if it was composed of valence quarks and an increasing number of sea quark-antiquark pairs and gluons, and the PDFs shift in shape accordingly. At the initial scales used in the fit procedures, up and down antiquarks and gluons are more abundant, and strange antiquarks are beginning to contribute. Charm, bottom, and top quarks do not contribute at these scales, but could potentially at higher scales past the appropriate thresholds.

The fit distributions also show good variation with  $Q^2$ . PDFs have  $Q^2$  dependence, and shift in particular ways as the scale changes. For each parton, the fit distribution at  $Q_{0sea}^2 = 0.7 \text{ GeV}^2$  resembles what the  $Q_{0sea}^2 = 0.5 \text{ GeV}^2$

curve would look like if shifted to a slightly higher scale. The reader should note that the two sets of parameters were obtained in separate fits, and that if one set of distributions was brought to the initial  $Q^2$  scale of the other set they would not match exactly. The  $Q^2$  dependence of the fit distributions will be explored in more detail in section 4.5.

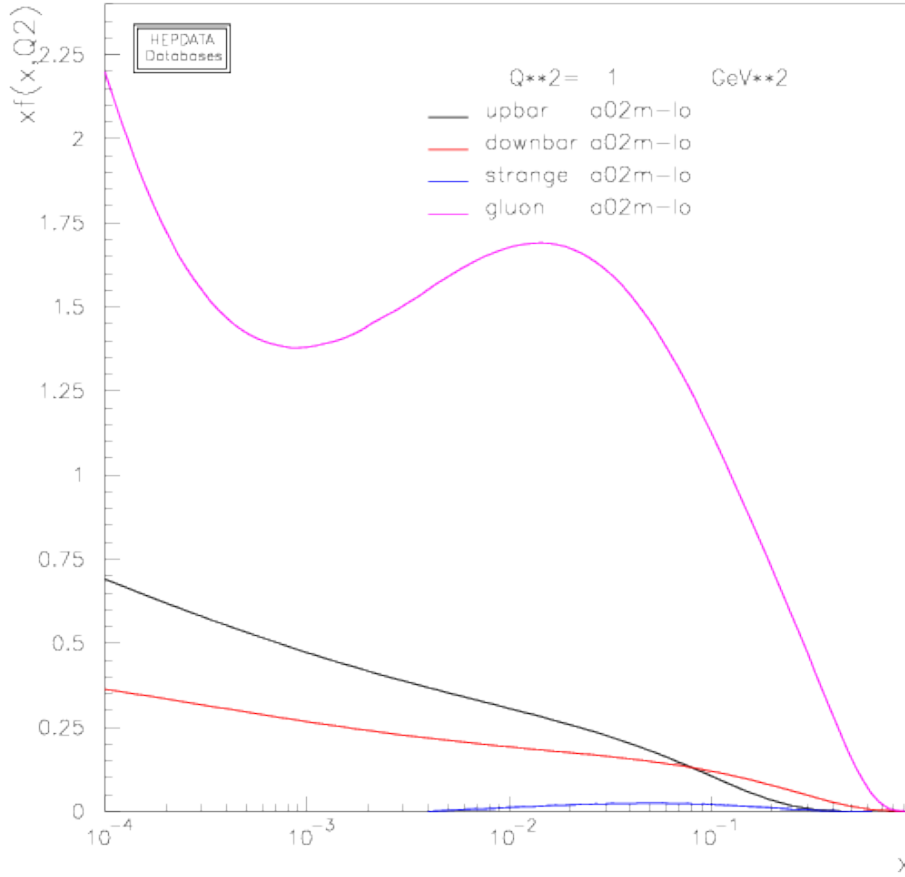


Figure 4.2: The plot above shows the distributions  $Xf(X)$  from set a02m.lo for gluons as well as up, down, and strange antiquarks. The distributions are shown at  $Q^2 = 1 \text{ GeV}^2$ . The plot was produced using the PDF plotter by Durham University, available online at <http://hepdata.cedar.ac.uk/pdf/pdf3.html>

For comparison, a plot of Alekhin's distributions are presented at the

nearby scale of  $Q^2 = 1 \text{ GeV}^2$ . The distributions are not directly provided at the low initial scales for the sea quark and gluon GPDs. The value of  $Q^2 = 1 \text{ GeV}^2$  is safely above the lowest scale provided, and can still illuminate the important trends in the PDFs at such low scales. The relative shapes and values of each curve are compared to the distributions in figure 4.1, taking careful consideration of the separate  $Q^2$  values. See section 4.4 for a direct comparison of all distributions at the same energy scale.

The resemblance between the overall relative shapes of the curves is immediately apparent. Alekhin's strange antiquark distribution has very low values, peaking at low to mid  $X$ . The up and down antiquark distributions show similar relative proportions at low  $X$  and mid  $X$  to those in figure 4.1, with the up antiquark PDF crossing below the down antiquark PDF. The gluon distribution requires more of an explanation.

One notable feature of the gluon distribution in Figure 4.2 is the low  $X$  behavior. As  $X$  decreases from about 0.1, there is a local maximum, followed by a local minimum, and then the gluon distribution rises again towards the left end of the plot. The rise at low  $X$ , indicating divergent behavior as  $X$  approaches 0, is characteristic of the gluon distribution at moderate  $Q^2$  values. This is in contrast to the low  $X$  behavior for the gluon distributions in figure 4.1. Later sections in this chapter will show that the fit gluon distributions will gain this rising behavior at low  $X$  as they evolve to higher  $Q^2$  values, and that they will transition through a shape that resembles the curve in Figure 4.2. There will be a more in depth discussion in section 4.5, where the GPDs



are examined at a variety of  $Q^2$  values.

## 4.4 Distributions at 25 GeV<sup>2</sup>

After the PDF functional forms are filled at their initial scales, they can be evolved to other  $Q^2$  values using pQCD evolution equations. The evolution procedure is the same as the one used to obtain the fit results. To summarize briefly, first the PDF forms for up and down valence quarks are obtained at their initial scale,  $Q_0^2$ . These distributions are evolved up to the initial scale for the sea quark and gluon PDFs,  $Q_{0sea}^2$ , by using the LO DGLAP evolution equations. The PDFs for the sea quarks (up, down, and strange) and gluons are filled at this scale, and all distributions are then evolved together to the final  $Q^2$  scale.

The plots below show the distributions for  $XH_{\bar{u}}(X, 0, 0)$ ,  $XH_{\bar{d}}(X, 0, 0)$ ,  $XH_{\bar{s}}(X, 0, 0)$ , and  $H_g(X, 0, 0)$  evolved to the final scale of  $Q^2 = 25 \text{ GeV}^2$ . Each plot contains one distribution from the fit with  $Q_{0sea}^2 = 0.5 \text{ GeV}^2$  and one from the fit with  $Q_{0sea}^2 = 0.7 \text{ GeV}^2$ . The plots also include Alekhin's corresponding distributions from the set a02m\_lo. Error bands for Alekhin's distributions, equal to half of the error provided in set a02m\_lo, are included as well to give an indication of the error values used in the fit procedure. The X points used in the fit procedure are also indicated in the plots so that the fit distributions can be evaluated at these X points.

The fit distributions are evaluated based on how well they match the central

value curves for Alekhin's distributions over the range of  $X$  values. An ideal fit distribution would match the central value curve exactly over the entire  $X$  region. The farther a fit distribution deviates from the central value curve in a certain  $X$  region, the worse the fit is considered in that particular region. Preferably, the fit distributions should deviate by an amount comparable to or less than the error values used in the fit procedure for Alekhin's distributions. In other words, the fit distributions in the plots below should not stray far outside the displayed error bands. The distributions tend to be small at higher  $X$  values, and the interesting behavior occurs at low  $X$ . A log scale in  $X$  is used to emphasize the low  $X$  behavior.

Figure 4.3 shows good agreement between both fit distributions and Alekhin's distribution for up antiquarks. Both fit distributions nearly overlap Alekhin's central value curve over the entire low  $X$  region. Upon close inspection, both distributions stray just above the error band for the mid to high  $X$  region. However, if the error for Alekhin's distribution in the fit procedure dropped below an imposed minimum value of 0.005, then 0.005 was used instead. Both fit distributions stay within this minimum error band in the mid to high  $X$  region. There is reasonably good agreement between Alekhin's distribution and the fit distributions at the  $X$  points used in the fit, as well as for the rest of the  $X$  region between 0.0001 and 1.

Figure 4.3 also displays the typical features of the up antiquark distribution at 25 GeV<sup>2</sup>. The distribution approaches 0 as  $X$  approaches 1. As  $X$  decreases from 1, the distribution gradually begins to rise more rapidly. There

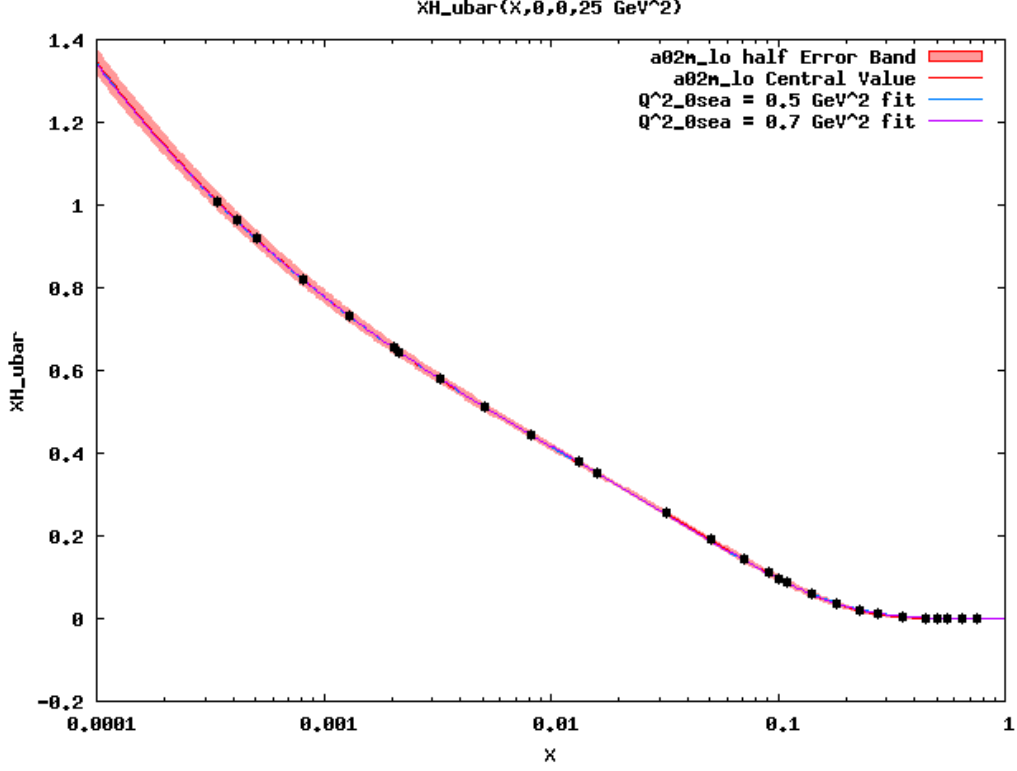


Figure 4.3: The plot above shows the distribution  $XH_{\bar{u}}(X, 0, 0, 25 \text{ GeV}^2)$  for the two fits. Alekhin's distribution  $X\bar{u}(X)$  used in the fit procedure is included with an error band of one half of the error for the set a02m\_lo. The X points used in the fit procedure are indicated by black dots.

is a characteristic small bump at about  $X = 0.02$ , and then the distribution continues to rise more rapidly as  $X$  decreases to 0.0001. The up antiquark fit distributions show the expected rising behavior towards low  $X$ , the small bump at mid  $X$ , and the gradual drop to 0 at high  $X$  values.

Figure 4.4 shows good agreement between both fit distributions and Alekhin's distribution for down antiquarks. Both fit distributions stay close to Alekhin's central value over the entire  $X$  region, with a few minor exceptions. In the very low  $X$  region below  $X = 0.001$ , both fit distributions rise a bit high, and the distribution with  $Q_{0sea}^2 = 0.5 \text{ GeV}^2$  passes just outside the error band.

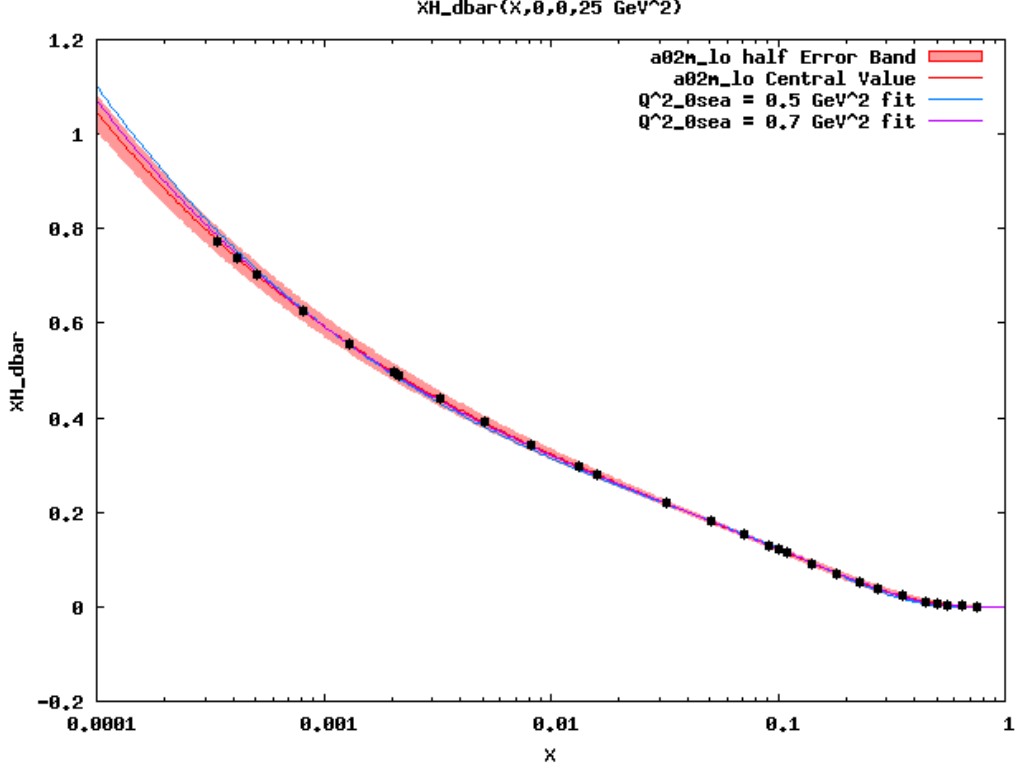


Figure 4.4: The plot above shows the distribution  $XH_{\bar{d}}(X, 0, 0, 25 \text{ GeV}^2)$  for the two fits. Alekhin's distribution  $X\bar{d}(X)$  used in the fit procedure is included with an error band of one half of the error for the set a02m\_lo. The X points used in the fit procedure are indicated by black dots.

The distributions still match reasonably well, especially around the X points used in the fit for this region. The fit distribution with  $Q_{0sea}^2 = 0.7 \text{ GeV}^2$  stays within the error bands until very near  $X = 1$ , where the distribution is well within the minimum error bands of 0.005. It stays close to Alekhin's central value curve, until it dips low at high X. The fit distribution with  $Q_{0sea}^2 = 0.5 \text{ GeV}^2$  wavers above and below the central value curve until it passes just below the error band at mid X values, and again at X close to 1. All things considered, both distributions show reasonably good agreement with Alekhin's distribution at the X points used in the fit as well as for the rest of the X

region between 0.0001 and 1.

Figure 4.4 also displays the typical features of the down antiquark distribution at 25 GeV<sup>2</sup>. The distribution approaches 0 as  $X$  approaches 1. As  $X$  decreases from 1, the distribution gradually begins to rise more rapidly. There is a characteristic bump that is more drawn out than for up antiquarks at around  $X = 0.1$ , and then the distribution continues to rise more rapidly as  $X$  decreases to 0.0001. The down antiquark fit distributions show the expected rising behavior towards low  $X$ , the long drawn out bump at mid  $X$ , and the gradual drop to 0 at high  $X$  values.

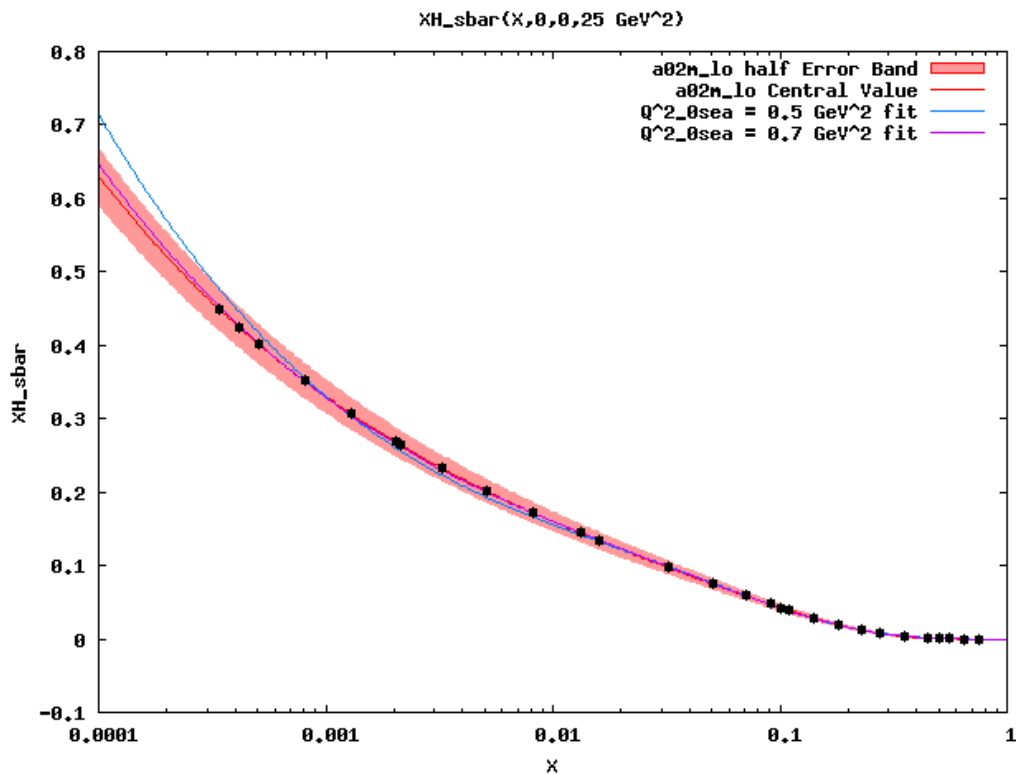


Figure 4.5: The plot above shows the distribution  $XH_{\bar{s}}(X, 0, 0, 25 \text{ GeV}^2)$  for the two fits. Alekhin's distribution  $X\bar{s}(X)$  used in the fit procedure is included with an error band of one half of the error for the set a02m\_lo. The  $X$  points used in the fit procedure are indicated by black dots.

Figure 4.5 shows good agreement between both fit distributions and Alekhin's distribution for strange antiquarks. Both fit distributions stay close to Alekhin's central value over the entire  $X$  region, with a few minor exceptions. The plot shows that the fit with  $Q_{0sea}^2 = 0.5 \text{ GeV}^2$  diverges too rapidly at very low  $X$ , and passes above the error band. There is still reasonably good agreement with Alekhin's distribution, especially close to the  $X$  points used in the fit procedure. Both fit distributions then stay close to Alekhin's distribution, within the error bands, until mid to high  $X$ . Both fit distributions pass just above the error band at mid to high  $X$ , but they stay well within the minimum error band of 0.005. There is good agreement between Alekhin's distribution and the fit distributions at the  $X$  points used in the fit. There is also good agreement over the entire  $X$  region, except that the fit with  $Q_{0sea}^2 = 0.5 \text{ GeV}^2$  diverges more rapidly at very low  $X$  compared to Alekhin's distribution.

Figure 4.5 displays the typical features of the strange antiquark distribution at  $25 \text{ GeV}^2$ . The distribution approaches 0 as  $X$  approaches 1. As  $X$  decreases, the distribution rises very gradually. As with the other antiquark distributions, there is a bump at mid  $X$ , though for strange quarks it is very mild and drawn out. The distribution rises more rapidly until it displays divergent behavior at low  $X$ , as  $X$  approaches 0. The strange antiquark fit distributions show the expected rising behavior towards low  $X$ , the mild, drawn out bump at mid  $X$ , and the gradual drop to 0 at high  $X$  values.

Figure 4.6 shows good agreement, overall, between both fit distributions and Alekhin's distribution for gluons. The most notable exception is in the

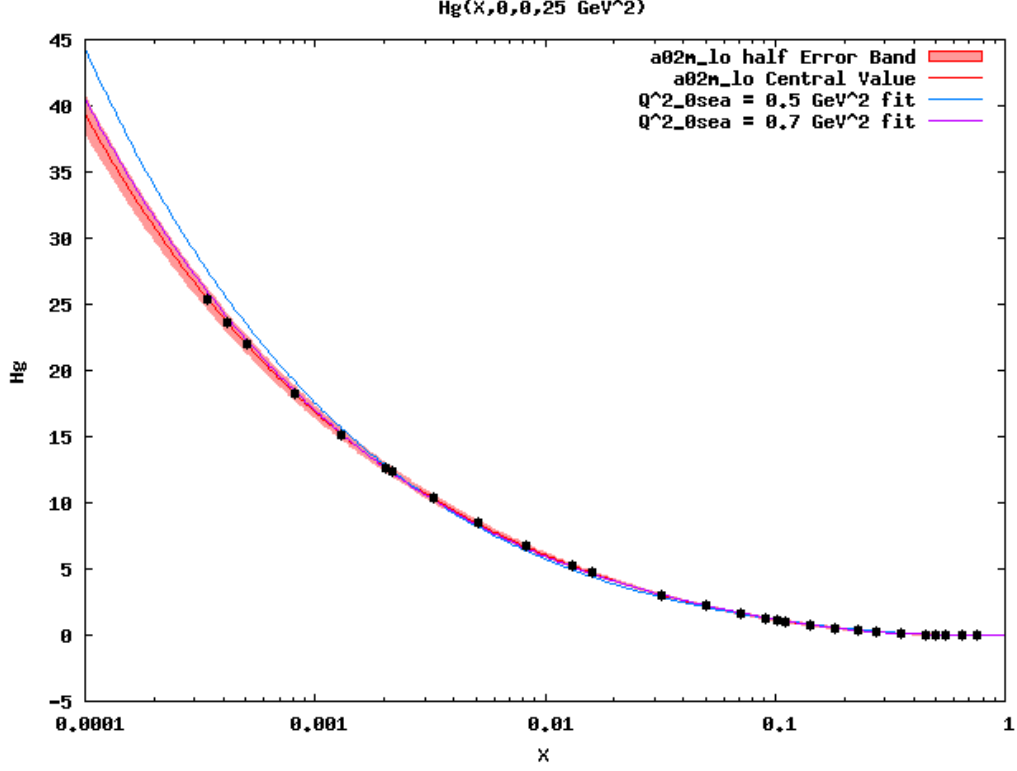


Figure 4.6: The plot above shows the distribution  $H_g(X, 0, 0, 25 \text{ GeV}^2)$  for the two fits. Alekhin's distribution  $Xg(X)$  used in the fit procedure is included with an error band of one half of the error for the set a02m\_lo. The X points used in the fit procedure are indicated by black dots.

very low  $X$  region below roughly  $X = 0.001$ . The fit distribution with  $Q_{0sea}^2 = 0.5 \text{ GeV}^2$  diverges more rapidly than Alekhin's distribution as  $X$  decreases, and passes beyond the error band by a significant amount. There is a difference on the order of 10% between the fit distribution and the central value curve at  $X = 0.0001$ . The curve also passes above the error bands at the first few  $X$  points used in the fit. This fit distribution may overestimate the low  $X$  behavior of the gluons compared to Alekhin's distribution, but there is comparable variation of the gluon PDF parametrizations between other groups as well at low  $X$ . Considering this, the fit distribution is reasonably large at low  $X$ , and can

acceptably contribute to calculations of DVCS observables, for example.

The fit distribution with  $Q_{0sea}^2 = 0.5 \text{ GeV}^2$  visibly dips just below the error band at low  $X$ , passing below a few  $X$  points used in the fit, and skims just above the error band when the band pinches slightly around  $X = 0.3$ . Otherwise, the fit stays within the error bands except at high  $X$  close to  $X = 1$ , when it is within the minimum error bands of 0.005. Overall, there is good agreement between the fit distribution with  $Q_{0sea}^2 = 0.5 \text{ GeV}^2$  and Alekhin's distribution for a majority of the  $X$  points used in the fit, as well as a majority of the total  $X$  region. At very low  $X$  and again at low  $X$ , the fit is reasonable, especially considering the variation of gluon PDFs between groups at very low  $X$ . The fit with  $Q_{0sea}^2 = 0.7 \text{ GeV}^2$ , on the other hand, stays within the error bands over the entire  $X$  region except for very high  $X$  close to  $X = 1$ , where it is within the minimum error bands. There is good agreement between the fit distribution with  $Q_{0sea}^2 = 0.7 \text{ GeV}^2$  and Alekhin's distribution at all  $X$  points used in the fit, as well as the entire  $X$  region.

Figure 4.6 displays typical features of the gluon distribution. The distribution approaches 0 as  $X$  approaches 1. The distribution rises gradually as  $X$  decreases, until it rises more quickly at low  $X$ . The gluon distribution shows divergent behavior at very low  $X$ , as  $X$  decreases towards 0. Both gluon fit distributions show the expected behavior over the entire  $X$  range. The distributions rise rapidly as  $X$  decreases towards  $X = 0.0001$ , and both distributions gradually level out as  $X$  increases until they approach 0 as  $X$  approaches 1.

The distributions at  $Q^2 = 25 \text{ GeV}^2$  show good agreement with Alekhin's



distributions. They also show the trends expected of PDFs at this moderate  $Q^2$  scale. At this energy scale, the proton interacts as if, in addition to valence quarks, it had an abundance of up, down, and strange quark-antiquark pairs as well as gluons. This is especially true at low LC momentum fractions, meaning that it is unlikely for a single sea quark or gluon to carry a majority of the proton's momentum along the light cone, but there may be numerous partons carrying very low fractions. There are even a significant amount of strange quarks contributing. The valence quark PDFs were not included in this discussion. Charm, bottom, and top quark distributions were also not included, because they were not included in the fit procedure. All three distributions were set to zero at the low initial scale for sea quarks and gluons, and although they may become nonzero as a result of the pQCD evolution equations, they were not included in the  $\chi^2$  fit procedure. The current fit procedure should be sufficient, but there are many intricacies regarding pQCD evolution that could potentially be adjusted and explored further in future fit procedures.

## 4.5 $Q^2$ Dependence

This section explores the  $Q^2$  dependence of the fit distributions, with a focus on the distributions with  $Q_{0sea}^2 = 0.7 \text{ GeV}^2$ . The evolution procedure is the same as the one used to obtain the fit results. The PDF forms for up and down valence quarks are obtained at their initial scale,  $Q_0^2$ , and then evolved using the LO DGLAP evolution equations to the initial scale for the sea quark and

gluon PDFs,  $Q_{0sea}^2$ . The PDFs for the sea quarks (up, down, and strange) and gluons are filled at this scale, and the LO DGLAP evolution equations bring all distributions to the final  $Q^2$  scale. See below for a discussion of the strange antiquark and gluon distributions evolved to various  $Q^2$  values. For the sake of brevity, only one antiquark distribution is presented in this section. The strange antiquark distribution is a useful example because the curve at the initial scale has low values, and serves as a useful reference for comparison as the distribution evolves. The up and down antiquark distributions have already been discussed at the initial and final  $Q^2$  values used in the fit procedure, and the distributions show the expected  $Q^2$  dependence between these scales.

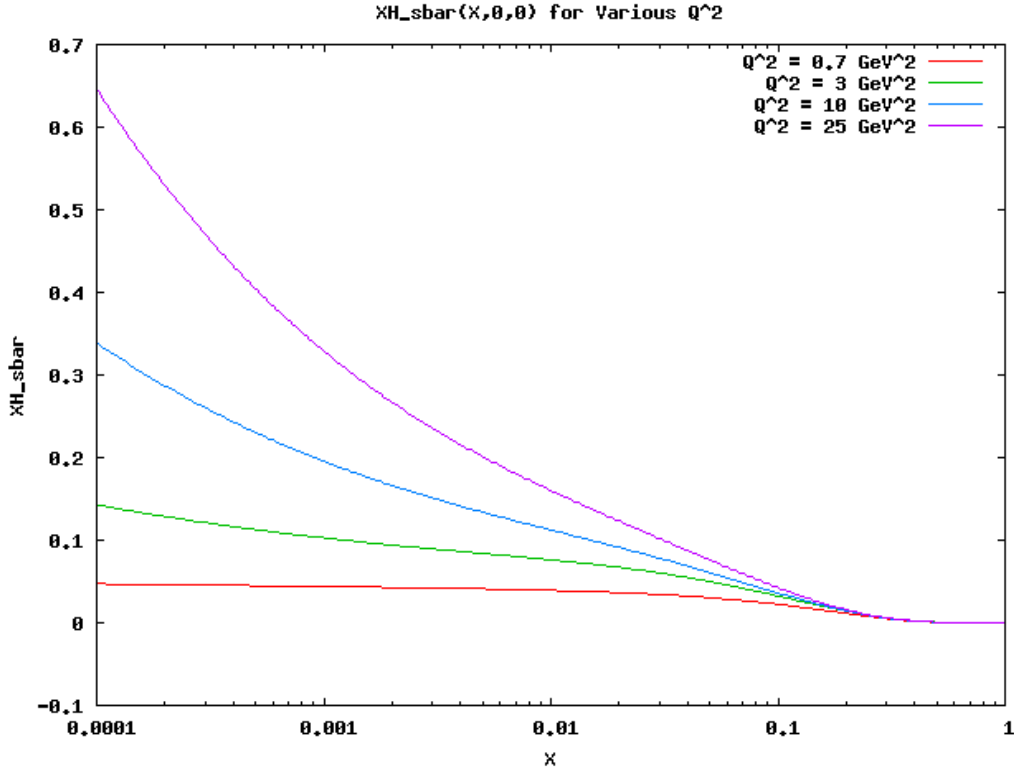


Figure 4.7: The plot above shows the fit distribution  $XH_{\bar{s}}(X,0,0)$  at various  $Q^2$  values. The fit distributions all use  $Q_{0sea}^2 = 0.7 \text{ GeV}^2$

Figure 4.7 shows the  $Q^2$  dependence of the strange antiquark distribution  $XH_{\bar{s}}(X,0,0)$ . As expected, the strange antiquark distribution shows the most dramatic changes at low  $X$ . The curves at higher  $Q^2$  values have much larger values at low  $X$ . Mathematically, this is a consequence of the LO DGLAP evolution equations' cumulative contributions as the scale rises, but it is consistent with the theoretical interpretation as well. As the  $Q^2$  scale rises, a probing photon's resolution of the proton changes, and the likelihood of interacting with strange sea quarks carrying a low fraction of the proton's momentum along the light cone increases. It is unlikely that a strange quark would carry a large portion of the proton's momentum along the light cone at any of the  $Q^2$  scales displayed. Overall, the strange antiquark distribution shows the expected  $Q^2$  dependence over a range of values.

Figure 4.8 shows the  $Q^2$  dependence of the gluon distribution  $H_g(X,0,0)$ . There is a slight shift at mid  $X$  values as the scale varies, and the gluon distribution changes dramatically at low  $X$  as expected. As discussed earlier in this chapter, the gluon distribution at the initial scale shows valence-like behavior. As the scale rises, the gluon distribution at  $Q^2 = 1 \text{ GeV}^2$  resembles the curve in Alekhin's distribution in figure 4.2 more closely. At higher scales, the gluon distributions more prominently show divergent behavior as  $X$  decreases towards 0. Although the very low  $Q^2$  behavior of the gluons is valence-like, the gluon distribution shows the expected  $Q^2$  dependence as the scale rises, and also compares roughly in shape to Alekhin's gluon distribution at  $Q^2 = 1 \text{ GeV}^2$  and  $25 \text{ GeV}^2$ .

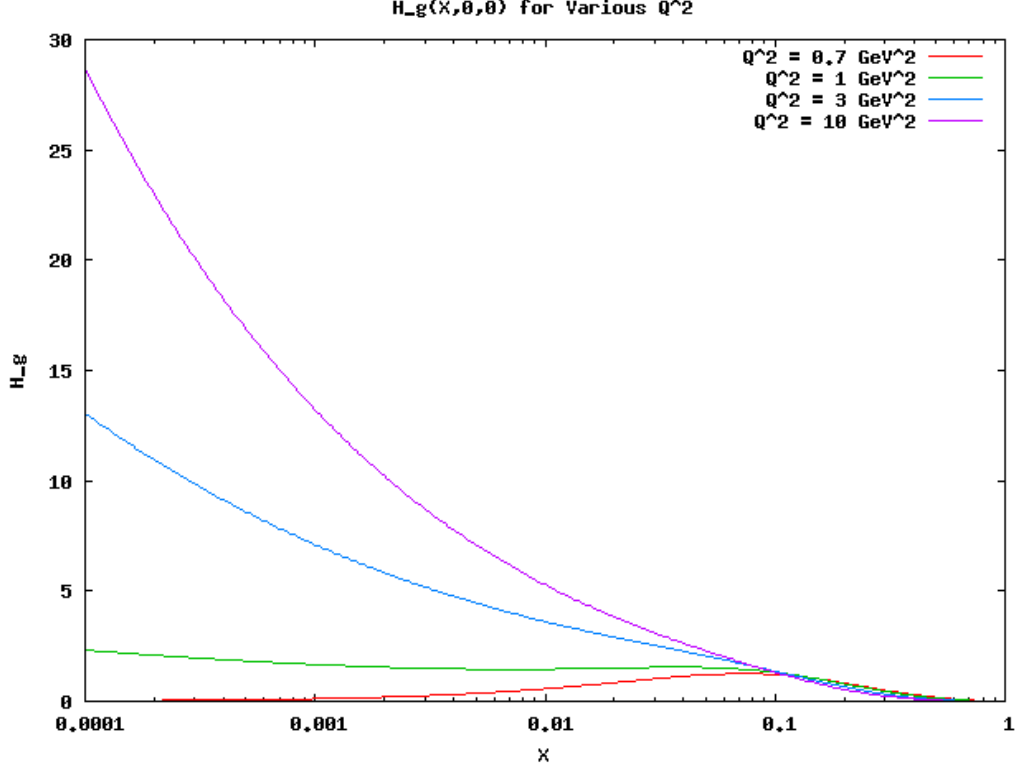


Figure 4.8: The plot above shows the fit distribution  $H_g(X,0,0)$  at various  $Q^2$  values. The fit distributions all use  $Q_{0sea}^2 = 0.7 \text{ GeV}^2$

The  $Q^2$  dependence of the gluon distributions is a consequence of the cumulative structure of the LO DGLAP evolution equations. In addition, there are contributions from the splitting functions for quarks and gluons ( $P_{qq}$  and  $P_{gg}$ ) as the scale rises, so the quark distributions influence the gluon distribution as they all evolve together. Similarly, the gluon distribution influences the strange antiquark distribution above because of contributions from the splitting function  $P_{qg}$ . As the  $Q^2$  scale rises, a probing photon's resolution of the proton changes. The likelihood of interacting with gluons that carry a low fraction of the proton's momentum along the light cone becomes much larger, and the likelihood of interacting with gluons that carry a moderate fraction

of the proton's momentum along the light cone becomes slightly reduced. It is unlikely that a gluon would carry a large portion of the proton's momentum along the light cone at any of the scales displayed. Overall, the gluon distribution shows the expected  $Q^2$  dependence at a variety of  $Q^2$  values.

## 4.6 Plots with $\zeta \neq 0$ , $t \neq 0$

The results discussed in the previous sections involved the PDF functional forms of the GPD expressions, by setting  $\zeta = 0$  and  $t = 0$ . The PDF functional forms are appropriate for describing an interaction, such as DVCS, in the case that the proton does not experience any net momentum transfer. The initial and final state protons have identical four-momenta. The full GPD expressions are advantageous because they are capable of describing interactions where there is a net four-momentum transfer,  $\Delta$ , and the initial and final state protons have different four-momenta. They even distinguish between the scale of the transfer ( $t = \Delta^2$ ) and the  $+$  component along the light cone, which involves the variables  $\xi$  or  $\zeta$ . In the next section, the gluon GPD results are explored in more detail by varying  $t$  and keeping  $\zeta = 0$ . The full gluon GPD expressions, with nonzero skew ( $\zeta > 0$ ), will be discussed in the section after.

## 4.7 $t$ Dependence

In this section, the gluon GPD  $H$  is presented at a variety of  $t$  values, while keeping  $\zeta = 0$ . As a reminder, the full GPD expression involves a term obtained from the spectator model multiplied by a Regge term with the basic form  $X^{-\alpha}$ . The Regge term has additional terms in the exponent proportional to  $t$ , and it is also possible to include terms in the exponent proportional to both  $\zeta$  and  $t$ . For now, the parameters in these additional terms are set to 0 for the gluon GPDs so that the terms do not contribute. This is done to explore the  $\zeta$  and  $t$  dependence of the gluon GPDs inherent in the spectator model. In the future, these parameters in the Regge term can be set by devising a fit procedure that includes  $\zeta$  and  $t$ , such as a global fit to DVCS data. It may be possible to use an iterative fit procedure to fit a few parameters at a time to select observables, but if not it's certainly possible to fit to DVCS data using brute force.

Figure 4.9 shows the dependence of the gluon GPD  $H$  on the variable  $t$ , at the various  $t$  values between 0 and -1. Overall, the distribution reduces in value as  $t$  becomes more negative, and the shape of the curve can be seen to shift gradually as  $t$  varies. There is always a peak at low  $X$  values, though the exact  $X$  point shifts sideways slightly. The valence-like shape of the gluon GPD  $H$  at the initial scale is preserved at all of the  $t$  values displayed, and the gluons involved in a process such as DVCS are most likely to carry a low fraction of the proton's momentum along the light cone.

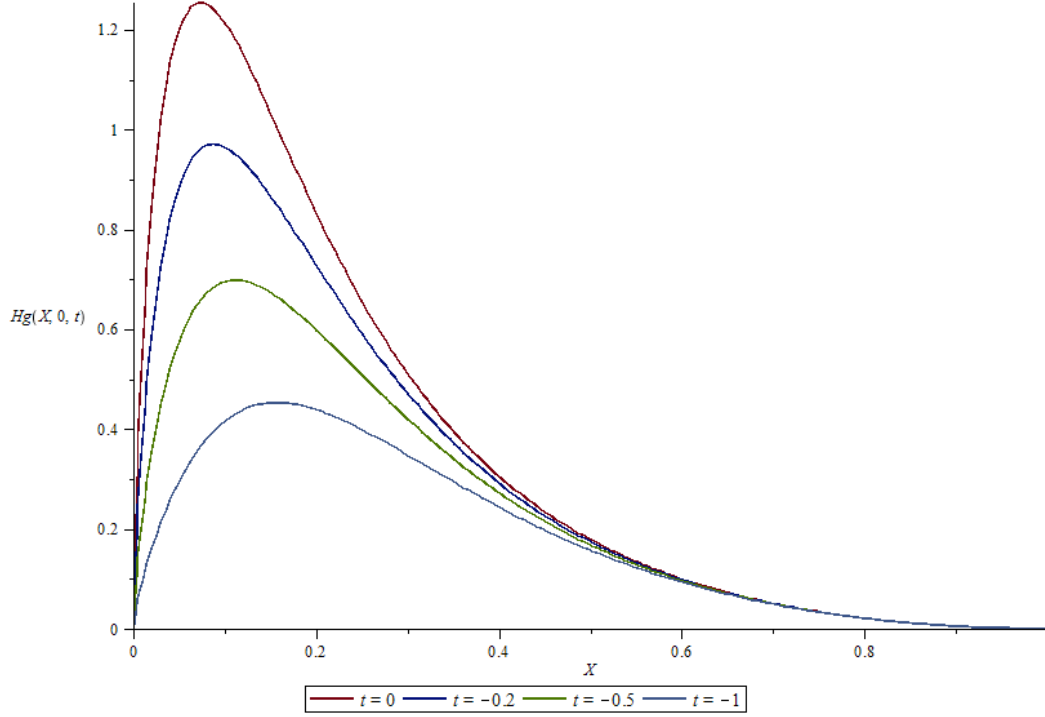


Figure 4.9: The plot above displays the distribution  $H_g(X,0,t)$  for a range of  $t$  values. The distributions all use the parameters for the fit with  $Q_{0sea}^2 = 0.7 \text{ GeV}^2$  and are displayed at the initial scale.

Figure 4.10 shows the gluon GPD  $H$  at fixed  $X$  points, with  $t$  ranging from 0 to -1. There is an emphasis on low  $X$  points because the gluon distributions are very sensitive in this region, especially as the  $Q^2$  scale evolves. The plot shows that the distributions show falling behavior as  $t$  becomes more negative, at all of the  $X$  points included. Overall, the gluon GPD  $H$  shows reasonable  $t$  dependence inherent in the spectator model, even without the  $t$ -dependent Regge term contributions. In a process such as DVCS, the gluon distributions generally reduce as  $t$  becomes more negative, favoring interactions with lower momentum transfers.

It is also worth considering the positivity constraints [23] on the gluon GPD

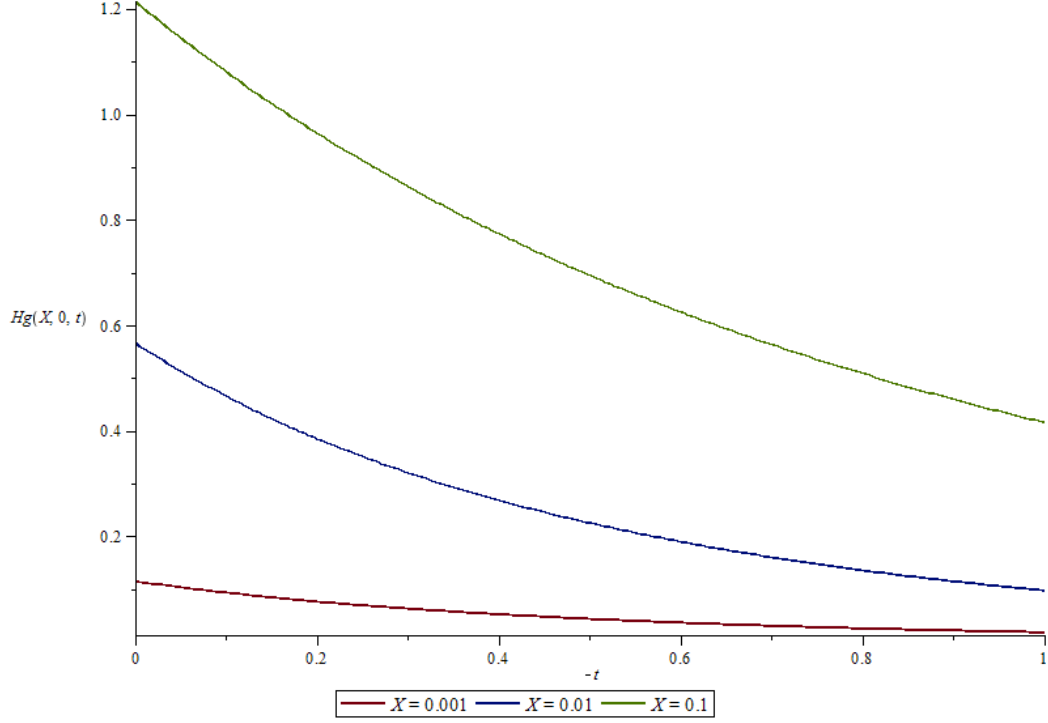


Figure 4.10: The plot above displays the distribution  $H_g(X,0,t)$  as a function of  $t$ , for several fixed  $X$  points. The distributions all use the parameters for the fit with  $Q_{0sea}^2 = 0.7 \text{ GeV}^2$  and are displayed at the initial scale.

H. In the case that  $\zeta = 0$ , one set of positivity bounds with weak constraints reduces to the simplified form:

$$|H_g(X, 0, t)| \leq |H_g(X, 0, 0)| \quad (4.4)$$

Where the form  $H_g(X, 0, 0)$  is equivalent to the PDF functional form of  $Xg(X)$ .

It can be seen from the figures in this section that the gluon GPD  $H$  appears to obey the positivity constraints at a first glance. A more rigorous analysis would examine the full range of  $X$  and  $t$  values more closely, with careful attention to the rate at which the distribution changes. It may be necessary to incorporate any additional parameters in the model before the full analysis.



As discussed earlier, the Regge term has additional terms in the exponent that have not been included in the initial results.

## 4.8 $\zeta > 0$

In this section, the gluon GPDs are expressed in the most general form by including nonzero  $t$  and  $\zeta$ . In this case, the GPDs describe a process with a difference in four-momentum between the initial and final state protons, including a difference in the  $+$  component along the light cone. The results for the gluon GPDs  $H$  and  $E$  are discussed in this section with  $\zeta > 0$  for a range of  $t$  values. As before, the Regge term has several parameters set to 0 so that it takes the basic form of  $X^{-\alpha}$ . The dependence on  $\zeta$  and  $t$  in the plots below is inherent to the spectator model.

Figure 4.11 shows the gluon GPD  $H$  for  $\zeta > 0$  and a variety of  $t$  values. The plot is shown in the DGLAP region for  $X > \zeta$ . The distributions indicate a gradual shift in shape as the  $t$  value varies, with more dramatic changes at the lower  $X$  values. The distributions also indicate a shift in shape from the distributions with  $\zeta = 0$ , without any significant new features. The distributions look as though they rise up towards a peak, similar to the features in figure 4.9, until they abruptly cut off at the boundary  $X = \zeta$ . At fixed  $\zeta$ ,  $t$  varies primarily because of the transverse component of the momentum transfer,  $\Delta_{\perp}$ . As the transverse momentum transfer becomes larger in magnitude and  $t$  becomes more negative, the GPD generally reduces in value, favoring

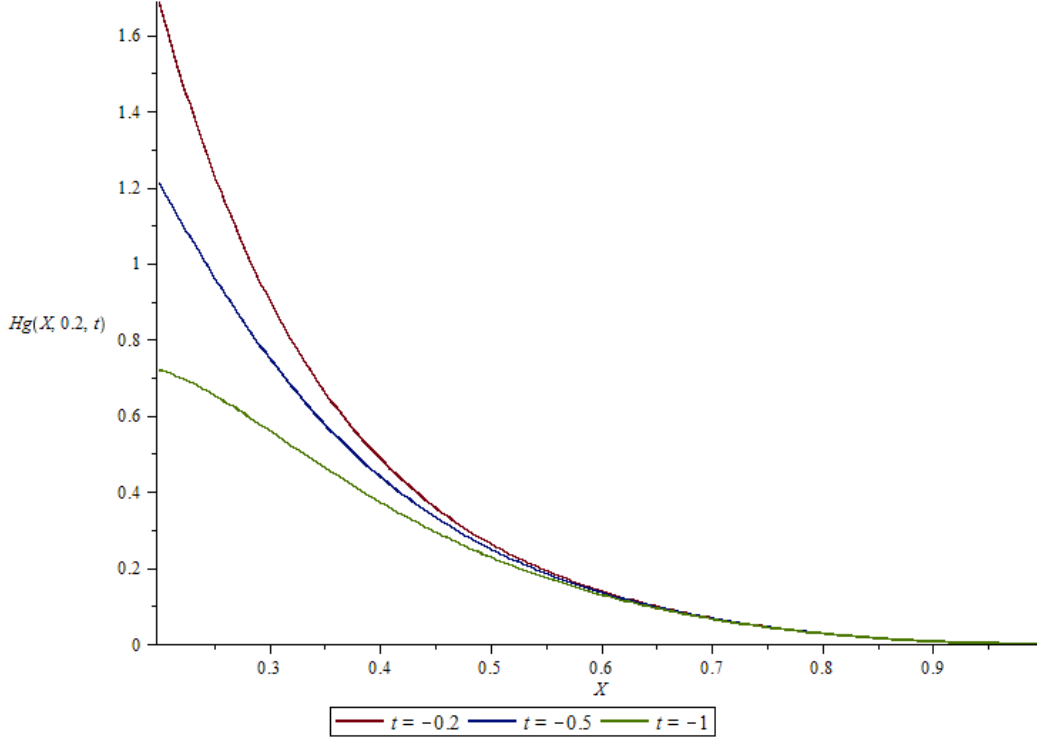


Figure 4.11: The plot above displays the distribution  $H_g(X, \zeta, t)$  for  $\zeta = 0.2$  and various  $t$  values. The distributions all use the parameters for the fit with  $Q_{0sea}^2 = 0.7 \text{ GeV}^2$  and are displayed at the initial scale.

interactions with smaller momentum transfer.

Figure 4.12 shows the gluon GPD  $E$  for  $\zeta > 0$  and a variety of  $t$  values. The gluon GPD  $E$  currently uses the same parameters obtained for the GPD  $H$ . Again, the plot is shown in the DGLAP region for  $X > \zeta$ . As with the GPD  $H$ , the GPD  $E$  shows a gradual shift in shape as the  $t$  value varies, with the more dramatic changes in the lower  $X$  region. Each distribution tapers off as  $X$  approaches 1, and has a smooth dip at low  $X$  that gets cut off at the boundary  $X = \zeta$ . As the value for  $t$  becomes more negative, primarily because of an increase in the magnitude of  $\Delta_\perp$  when  $\zeta$  is fixed, the GPD  $E$  generally reduces to less negative values. The distribution has more significant values

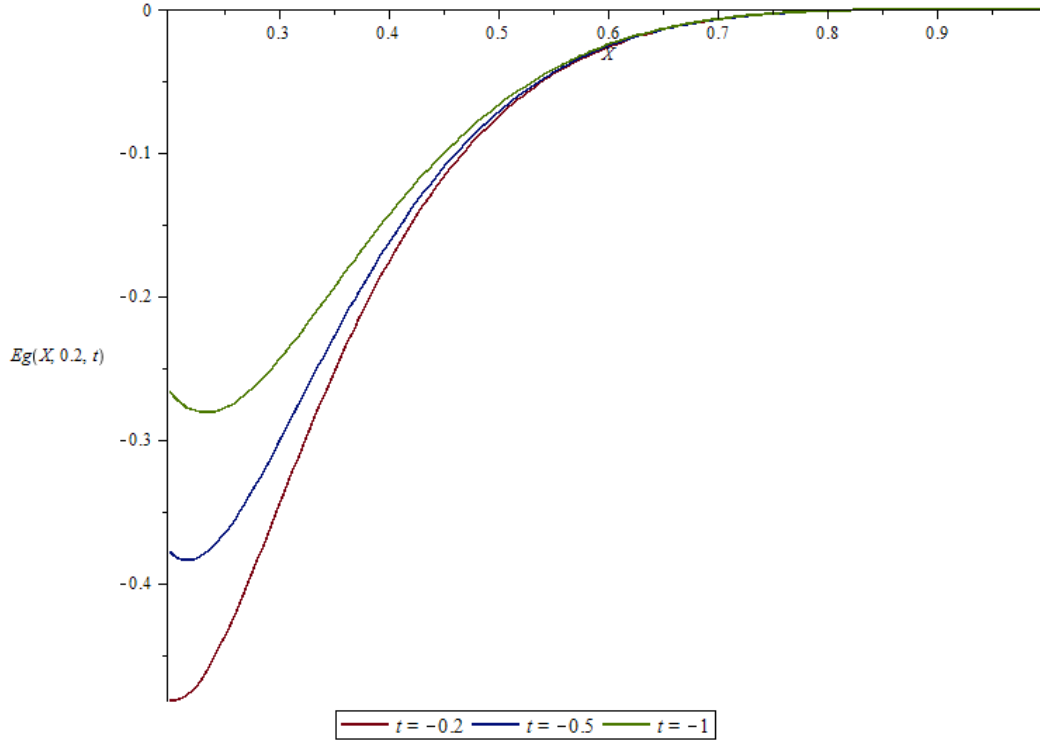


Figure 4.12: The plot above displays the distribution  $E_g(X, \zeta, t)$  for  $\zeta = 0.2$  and various  $t$  values. The distributions all use the parameters for the fit with  $Q_{0sea}^2 = 0.7 \text{ GeV}^2$  and are displayed at the initial scale.

at smaller momentum transfers.

The remaining figures show the distribution  $H_g(X, \zeta, t, Q^2)$  for a variety of  $\zeta$ ,  $t$ , and  $Q^2$  values. Figure 4.13 shows the distributions at the initial scale. For each fixed value in  $\zeta$ , the plots show the expected shifts as  $t$  begins at  $t_{\min}$  and becomes more negative.

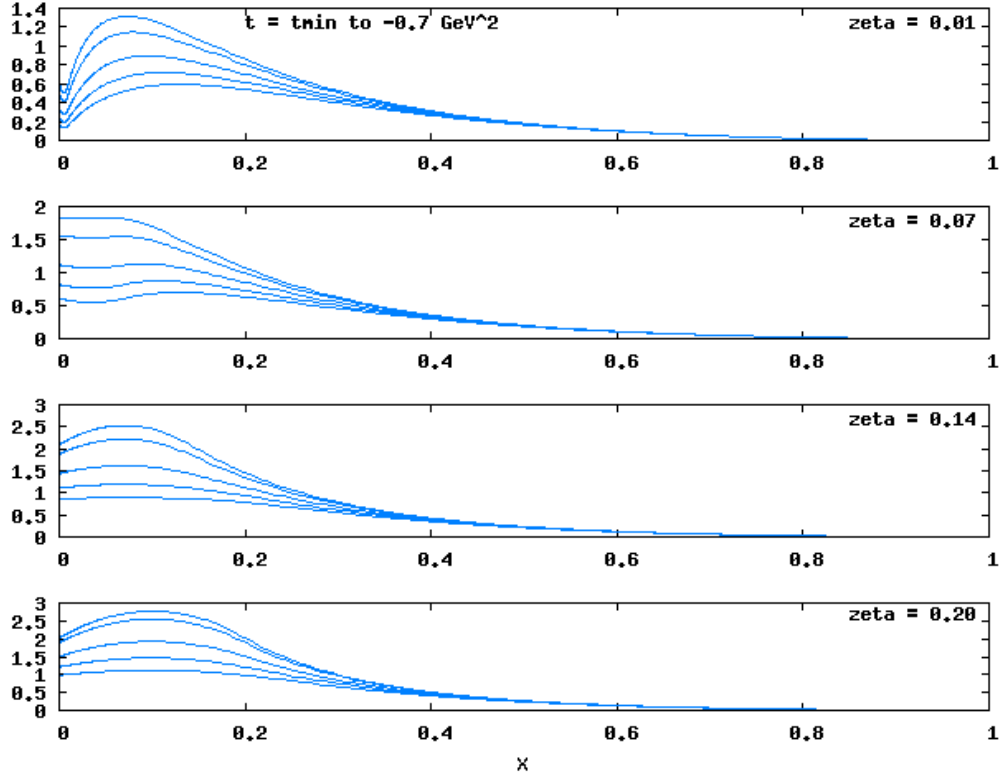


Figure 4.13: The distribution  $H_g(X, \zeta, t)$  at the initial scale of  $Q^2 = 0.7 \text{ GeV}^2$ , for a variety of  $\zeta$  and  $t$  values.

The gluon distributions are presented at higher scales below. The quark and gluon distributions are all fitted at their own initial scales, and are all brought up together to the final scale during the evolution process. The  $t$ -dependent Regge terms have not been fit yet for the sea quark or gluon distributions. The  $t$ -dependent Regge parameters for the up valence quark distributions are used for the up sea quark distributions as well, and similarly

the  $t$ -dependent Regge parameters for the down valence quark distributions are used for the down sea quark distributions. All  $t$ -dependent Regge parameters for the strange quark and gluon distributions are kept at 0, so that all of the  $t$ -dependence for these particular distributions at the initial scale is inherent to the spectator model. For each fixed  $\zeta$  value in figures 4.14 and 4.15, the plots show the expected shifts as  $t$  begins at  $t_{\min}$  and becomes more negative. A more rigorous analysis would examine the distributions more thoroughly, to ensure that the distributions obey the constraints of the positivity bounds for a variety of  $\zeta$ ,  $t$ , and  $Q^2$  values.

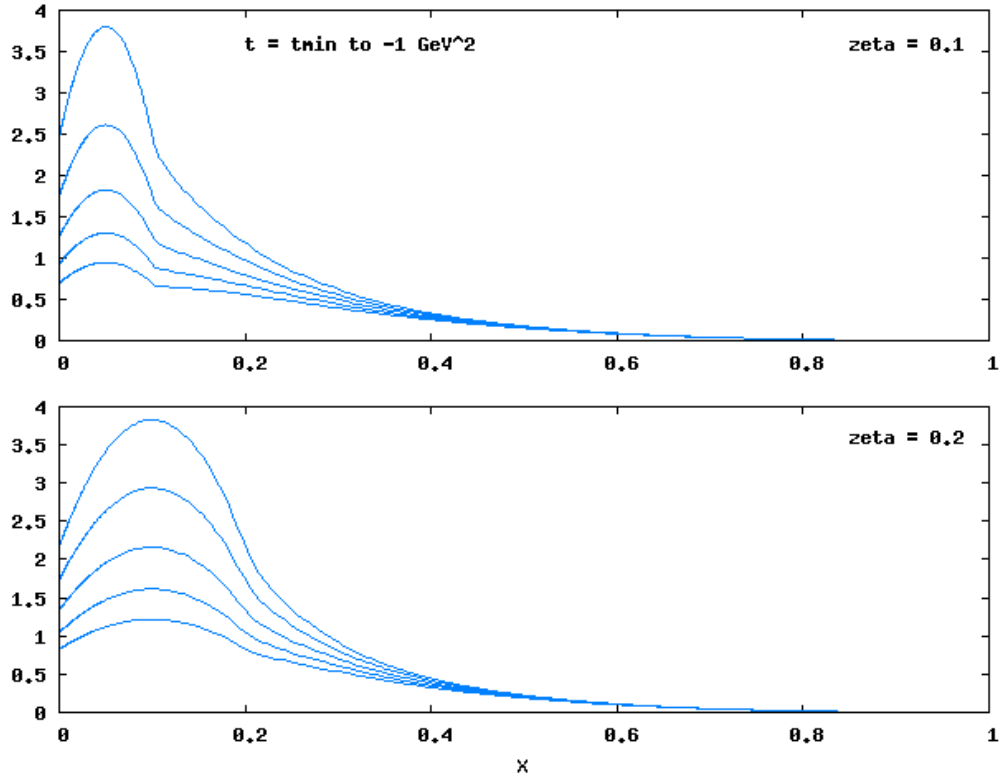


Figure 4.14: The distribution  $H_g(X, \zeta, t)$  at  $Q^2 = 1 \text{ GeV}^2$ , for a variety of  $\zeta$  and  $t$  values.

The plots in this section were discussed in the DGLAP region. The ERBL

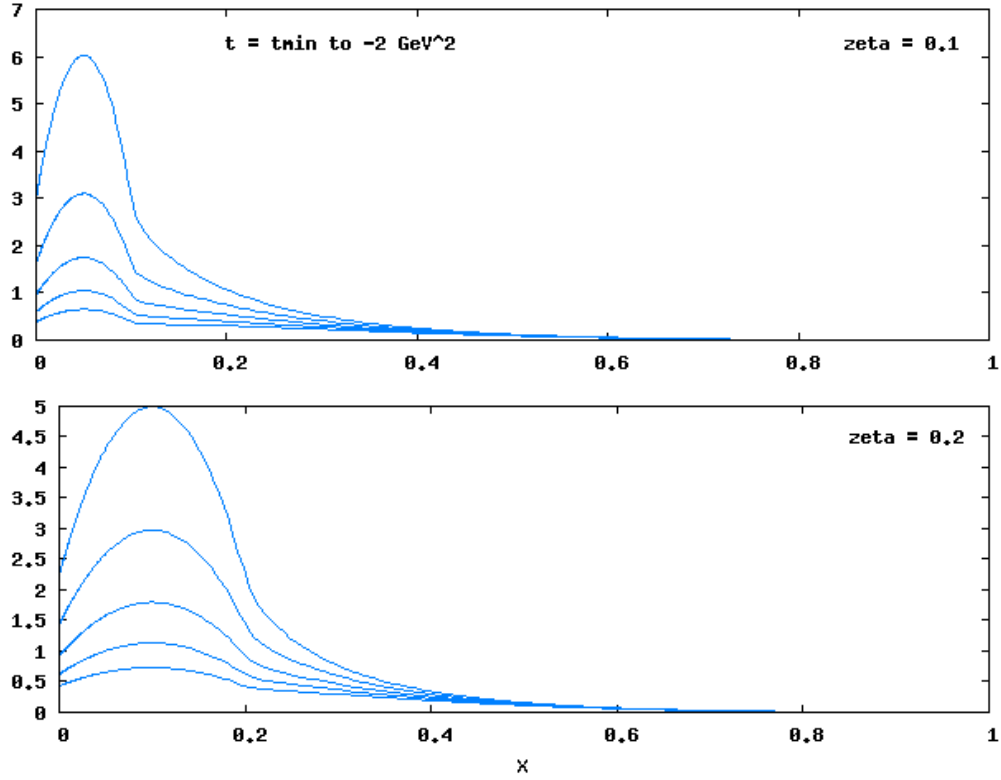


Figure 4.15: The distribution  $H_g(X, \zeta, t)$  at  $Q^2 = 2 \text{ GeV}^2$ , for a variety of  $\zeta$  and  $t$  values.

region with  $0 < X < \zeta$  involves a different model and a different partonic interpretation than the DGLAP region. The gluon GPDs obey symmetry and antisymmetry relations in the ERBL region, and so do the "singlet" and "non-singlet" combinations of each quark GPD [11]. In the ERBL region, each distribution can be expressed with functional polynomial parametrizations that fulfill several properties of the GPDs [31].

The distributions in figures 4.13, 4.14, and 4.15 use a particular functional form in the ERBL region. For each distribution, the curve was evaluated at the final  $Q^2$  scale in the DGLAP region first, and afterwards the curve was evaluated in the ERBL region. The functional form in the ERBL region is

given by the following:

$$H_g(X, \zeta, t) = a_1 \left( X - \frac{\zeta}{2} \right)^2 + a_2 \quad (4.5)$$

where  $a_1$  and  $a_2$  are constants. These two constants are uniquely chosen for each distribution such that they preserve continuity at the crossover point  $X = \zeta$ , and that they preserve continuity of  $H'_g(X, \zeta, t)$ , the derivative of  $H_g(X, \zeta, t)$  with respect to  $X$ , at the crossover point as well. The computational methods used to produce the distributions in the DGLAP regions for the three figures above used a rigid array of  $X$  points, which did not include the point  $X = \zeta$  for any of the distributions. The values of  $H_g(\zeta, \zeta, t)$  and  $H'_g(\zeta, \zeta, t)$  were instead extrapolated from the first four points in the DGLAP region by using Lagrange polynomials. This model for the ERBL region of the gluon GPDs is not fully established and is subject to change. A full analysis would establish models for the GPDs in the ERBL region and find procedures to constrain and fit the parameters.

## 4.9 Predictions of the Polarized Gluon PDF

In the forward limit, with  $\zeta = 0$  and  $t = 0$ , the gluon distribution  $\tilde{H}_g(X, 0, 0)$  reduces to  $X\Delta g(X)$ , for  $X > 0$ . In order to make a preliminary prediction for the polarized gluon PDF, parameters are chosen for the  $\tilde{H}_g$  distribution. The parameters are currently chosen to match the fit results for  $H_g$  with the initial

scale for sea quarks and gluons of  $Q_{0sea}^2 = 0.7 \text{ GeV}^2$ . A future fit could find a unique set of parameters for  $\tilde{H}_g$ , rather than using the same set of parameters as for  $H_g$ . The resulting plot of  $\tilde{H}_g(X, 0, 0)$  at its initial scale is displayed in figure 4.16.

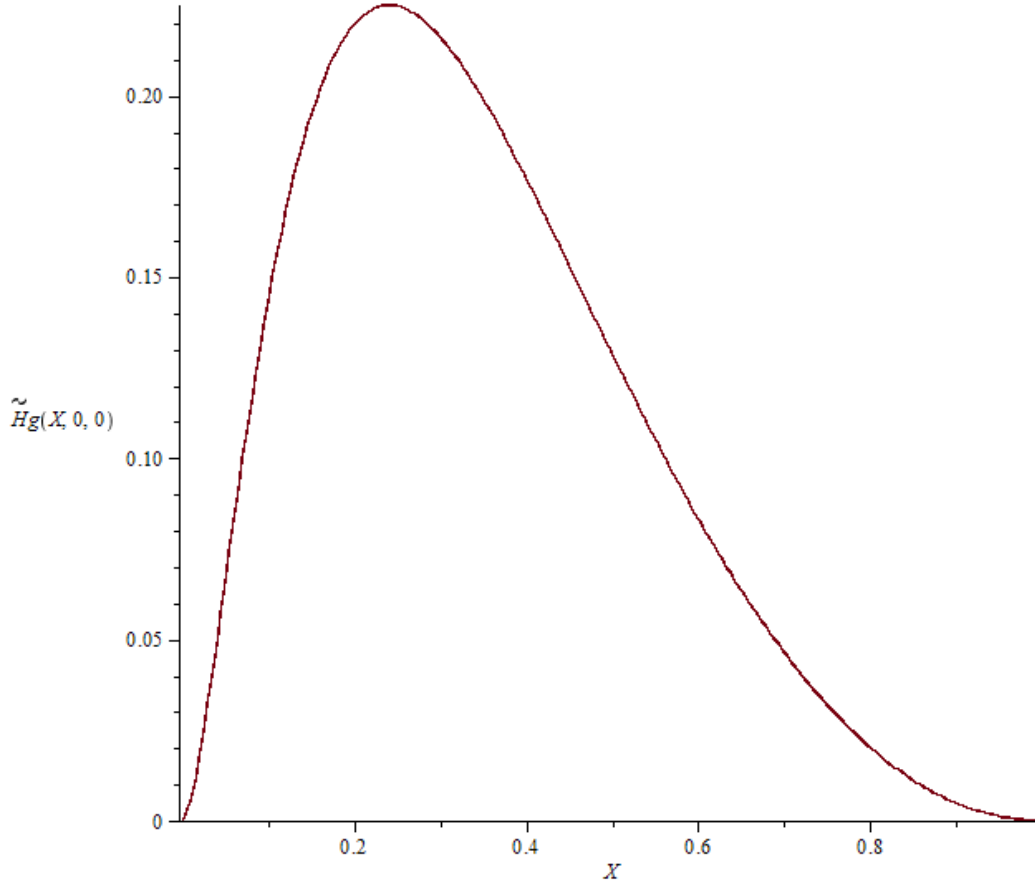


Figure 4.16: The distribution  $\tilde{H}_g(X, 0, 0)$  at its initial scale of  $Q_{0sea}^2 = 0.7 \text{ GeV}^2$ .

As expected, the distribution drops towards 0 as  $X$  approaches 1. The peak value is much smaller than for the unpolarized PDF, as the polarized PDF involves the difference of gluon polarization states rather than a sum. Overall, the shape of the distribution  $X\Delta g(X)$  is reasonable with the current parameters.



## 4.10 Applications of GPDs

The initial fits for the sea quark and gluon GPDs in this chapter look promising. The GPDs display a range of behaviors over various kinematic regions that are consistent with expectations. There are several ways in which future fit procedures could expand on the initial set of parameters. For instance, the parameters in the initial fit are obtained for the sea quark and gluon  $H$  distributions. The current analysis uses these same parameter values in the corresponding  $E$  distributions. A future fit may find new values for some or all of the parameters in the  $E$  distributions. Similarly, future fits may find a new set of parameters for each of the  $\tilde{H}$  and  $\tilde{E}$  distributions. There are also additional parameters in the Regge terms and the ERBL parametrizations. There are many parameters left to fit, but the initial results can still offer insight. The helicity conserving GPDs have many useful applications, including contributions to DVCS observables. The next chapter will discuss the role of the GPDs in DVCS, as well as other general properties of the distributions.

# Chapter 5

## Applications and Outlook

### 5.1 Applications of GPDs

The GPDs modeled in this analysis play a crucial role in describing DVCS interactions. The soft hadronic subprocesses can be defined in terms of the GPDs, and so the total Compton amplitudes are expressed in terms of the GPDs as well. In this way, the GPDs contribute to predictions for observables. If the GPDs have been modeled previously, they can be used to make predictions on the expected values for the observables. If the GPDs have not been fit previously, then many parameters for several of them can be fit simultaneously to DIS and DVCS data in a global fit procedure. The advantage of GPDs is that they can describe interactions with a four-momentum exchange between the initial and final state hadrons, while the PDFs only apply to interactions in the forward limit. One convenient way to generate DVCS interactions is by electron-proton scattering processes, or more specifically,  $(e + P \rightarrow e + P + \gamma)$

processes. The cross sections and beam asymmetries for these interactions can be expressed in terms of the GPDs, as discussed in section 5.2.

As previously discussed, the GPDs have a connection to Dirac, Pauli, axial, and pseudoscalar form factors. Several groups have parametrized various form factors. For example, see [7] for a parametrization of Dirac and Pauli form factors, and [19] for a parametrization of electric and magnetic form factors. The GPDs can be used to make predictions for the form factors, and these predictions can be compared to the available parametrizations. See section 5.4 for a more detailed discussion.

## 5.2 Electron-Proton and Positron-Proton Scattering

Electron-proton scattering experiments are ideal for generating DVCS interactions. Specifically, the process  $(e + P \rightarrow e + P + \gamma)$  involves contributions from interactions with a DVCS subprocess. The amplitudes for  $(e + P \rightarrow e + P + \gamma)$  have contributions from both DVCS and Bethe-Heitler (BH) processes [12]. In both cases, the incoming electron emits a virtual photon that gets absorbed by the proton. In the case of DVCS, the proton emits the real outgoing photon, while in the case of BH, the the real outgoing photon is emitted by the leptonic subprocess instead. See figure 5.1 for a diagram with contributions from DVCS, and figure 5.2 for diagrams of the BH contributions. The initial

lepton and proton have momentum  $k$  and  $p$  respectively, while the final state lepton and proton have momentum  $k'$  and  $p'$  respectively. The virtual photon has momentum  $q$ , and the outgoing real photon has momentum  $q'$ .

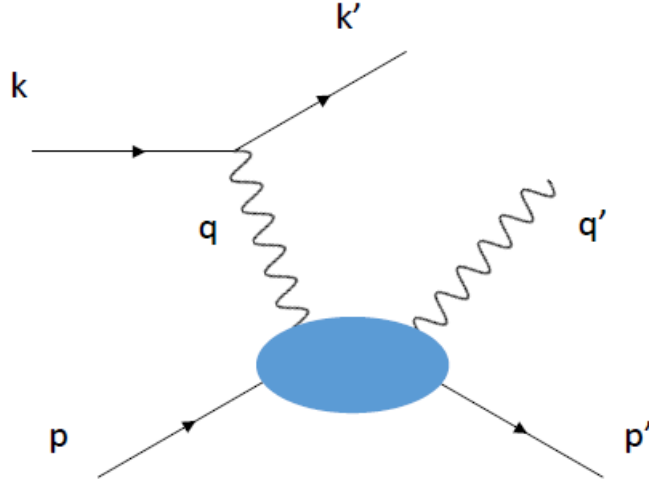


Figure 5.1: The diagram for electron-proton scattering amplitudes with a contribution from DVCS. Corresponding diagrams for positron-proton scattering amplitudes are obtained by replacing the initial and final state electrons with positrons.

The full  $(e + P \rightarrow e + P + \gamma)$  amplitude  $\mathcal{T}$  can be expressed in terms of amplitudes involving DVCS and BH processes,  $\mathcal{T}_{DVCS}$  and  $\mathcal{T}_{BH}$ . The amplitude squared is expressed as follows, along with an interference term  $\mathcal{I}$ .

$$\begin{aligned}\mathcal{T}^2 &= |\mathcal{T}_{DVCS}|^2 + |\mathcal{T}_{BH}|^2 + \mathcal{I} \\ \mathcal{I} &= \mathcal{T}_{DVCS}\mathcal{T}_{BH}^* + \mathcal{T}_{DVCS}^*\mathcal{T}_{BH}\end{aligned}\tag{5.1}$$

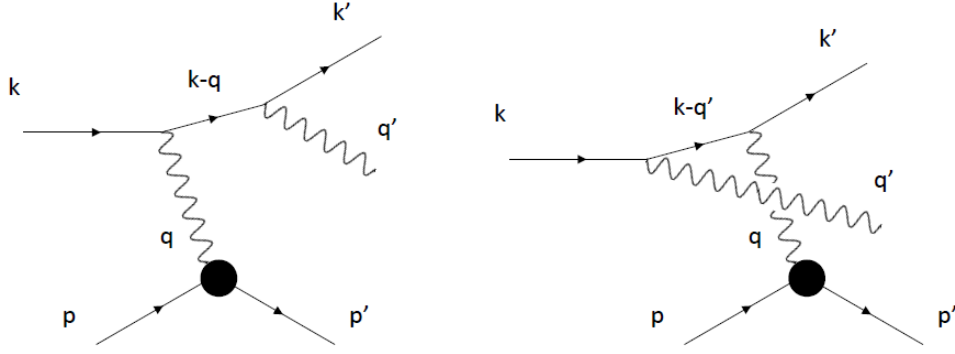


Figure 5.2: The diagrams for the electron-proton scattering amplitudes with contributions from BH processes with four-momentum labels. Left: The initial electron emits the virtual photon, and afterwards the intermediate electron emits the outgoing real photon. Right: The initial electron emits the outgoing real photon first, and afterwards the intermediate electron emits the virtual photon. In both cases, the corresponding diagrams for positron-proton scattering amplitudes are obtained by replacing the initial state, final state, and intermediate electrons with positrons.

Experiments often involve an electron beam focused on a proton beam or on a target that contains stationary protons. In the laboratory frame, the interactions involve fast moving electrons interacting with stationary target protons. The charge of the leptons can be reversed by substituting the electron beam with a positron beam. It is beneficial to collect data using an electron beam and a positron beam separately, because there are plenty of observables that are sensitive to beam charge asymmetries.

Experiments can assume the kinematics of the initial proton and the initial electron or positron in a given interaction, based on the controlled beam and target configurations. It is sufficient to select events with a detected photon in the final state as well as a single electron or positron, though some experiments

are able to detect the final state proton. Several filters can be imposed based on the kinematics in order to isolate kinematic regions that are more likely to be associated with DVCS events than background events. For example, it may be beneficial to filter events by requiring that the squared mass value for  $(q + p - q')^2$  is close to the squared proton mass. The virtual photon's momentum is not observed, but it can be evaluated for DVCS as  $q = k - k'$ . If the final state proton is not detected, its kinematics may be deduced in the case of a properly filtered exclusive event.

The kinematics are chosen to match closely with the conventions in [27]. The kinematics are defined in a frame with the target nucleon at rest at the origin, with the virtual photon moving directly in the  $-\hat{z}$  direction along the  $z$ -axis. The lepton scattering plane is defined by the three-momenta of the initial and final leptons,  $\vec{k}$  and  $\vec{k}'$ , and the hadron scattering plane is defined by the three-momenta of the recoiled proton and the outgoing photon,  $\vec{p}'$  and  $\vec{q}'$ . The angle between the lepton and hadron scattering planes is  $\phi = \phi_N - \phi_l$  where  $\phi_l$  is the azimuthal angle of the scattered lepton and  $\phi_N$  is the azimuthal angle of the recoiled proton.  $S_\perp$  is the transverse part of the nucleon polarization vector, and it has an azimuthal angle of  $\Phi$ . By definition, the angle  $\varphi = \Phi - \phi_N$  is the difference of the azimuthal angle of the transverse part of the nucleon polarization vector and the azimuthal angle of the recoiled proton. The four-momentum of the initial proton at rest is  $p = (M, 0, 0, 0)$ . The momentum transfer between the initial and final state hadrons will be defined by  $\Delta = p - p'$  for this discussion. In addition,  $Q^2 = -q^2$ ,  $t = \Delta^2$ , and  $W^2 = (p + q)^2$  for this

discussion.

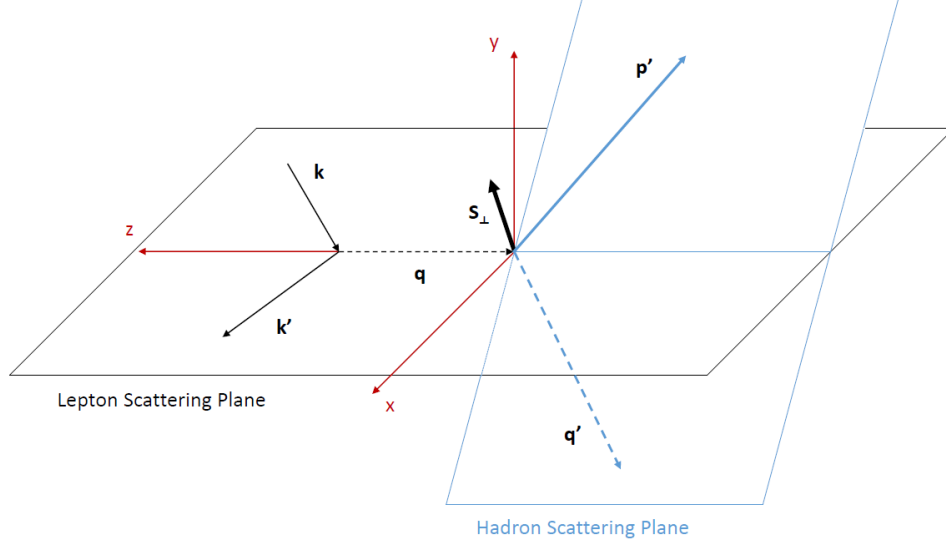


Figure 5.3: The kinematics in the target proton's rest frame, according to the convention in [27]. In this diagram, the scattered lepton's momentum vector has an azimuthal angle of  $\phi_l = 0$ , and  $\phi = \phi_N$  is the azimuthal angle between the lepton scattering plane and the recoiled proton's momentum.

The five-fold differential cross section for the  $(e + P \rightarrow e + P + \gamma)$  process is given by

$$\frac{d^5\sigma}{dx_B dy d|t| d\phi d\varphi} = \frac{\alpha^3 x_B y}{16\pi^2 Q^2 \sqrt{1+\epsilon^2}} \left| \frac{\mathcal{T}}{e^3} \right|^2 \quad (5.2)$$

where  $e$  is the elementary charge,  $\alpha$  is the fine structure constant, and the following variables are defined as

$$x_B \equiv \frac{Q^2}{2p \cdot q}, \quad y \equiv \frac{p \cdot k - p \cdot k'}{p \cdot k}, \quad \epsilon \equiv 2x_B \frac{M}{\sqrt{Q^2}} \quad (5.3)$$

The term  $|\mathcal{T}|^2$  is expanded in terms of the DVCS, BH, and interference term

contributions. In the chosen frame, these terms each can be expressed as sums of Fourier harmonics. The expansions are given by

$$\begin{aligned}
|\mathcal{T}_{BH}|^2 &= \frac{e^6}{x_B^2 y^2 (1 + \epsilon^2)^2 t \mathcal{P}_1(\phi) \mathcal{P}_2(\phi)} \left[ c_0^{BH} + \sum_{n=1}^2 \left( c_n^{BH} \cos(n\phi) \right) + s_1^{BH} \sin(\phi) \right] \\
|\mathcal{T}_{DVCS}|^2 &= \frac{e^6}{y^2 Q^2} \left[ c_0^{DVCS} + \sum_{n=1}^2 \left( c_n^{DVCS} \cos(n\phi) + s_n^{DVCS} \sin(n\phi) \right) \right] \\
\mathcal{I}^\mp &= \frac{\pm e^6}{x_B y^3 \mathcal{P}_1(\phi) \mathcal{P}_2(\phi) t} \left[ c_0^\mathcal{I} + \sum_{n=1}^3 \left( c_n^\mathcal{I} \cos(n\phi) + s_n^\mathcal{I} \sin(n\phi) \right) \right] \quad (5.4)
\end{aligned}$$

where the sign in the label  $\mathcal{I}^\mp$  stands for the charge of the lepton beam. For example,  $\mathcal{I}^+$  could result from a positron beam. The terms  $\mathcal{P}_1(\phi)$  and  $\mathcal{P}_2(\phi)$  are defined as

$$\mathcal{P}_1 \equiv \frac{(k - q')^2}{Q^2}, \quad \mathcal{P}_2 \equiv \frac{(k + \Delta)^2}{Q^2} \quad (5.5)$$

See reference [27] for a discussion on these two terms, particularly on their expanded forms and their dependence on  $Q^2$  and  $\phi$ .

The contributions to  $|\mathcal{T}|^2$  can also be evaluated in the usual way from helicity amplitudes, and the resulting expressions can be compared to the expansions in terms of Fourier harmonics. The helicity amplitudes for  $\mathcal{T}_{BH}$  introduce electromagnetic form factors from the soft subprocess, while the helicity amplitudes for  $\mathcal{T}_{DVCS}$  introduce the GPDs. Because of this, the coefficients for the BH term in equation 5.4 are parametrized in terms of electromagnetic form factors. The coefficients for the DVCS term are parametrized in terms of



the GPDs, or more specifically they are parametrized in terms of the Compton form factors (CFFs) evaluated from the GPDs. The coefficients in the interference term are parametrized in terms of electromagnetic form factors and the CFFs evaluated from the GPDs.

For each of the experimental events involving DVCS and the GPDs, it is possible to evaluate the kinematic values for  $Q^2$ ,  $t$ ,  $x_B$ , and  $W^2$  from the initial state and detected final state kinematics. The GPDs involve the momentum fraction  $X = \frac{k \cdot q}{p \cdot q}$  and the skewness variable  $\zeta = \frac{\Delta \cdot q}{p \cdot q}$ , as well as  $Q^2$  and  $t$ . Events can be selected to isolate values for  $Q^2$  and  $t$ . The skewness variable  $\zeta$  can be solved from  $x_B$ , where  $\zeta \simeq x_B$  for DVCS in the Bjorken limit. The momentum fraction  $X$  is not discernable experimentally, so theoretical expressions involving the GPDs are integrated over  $X$  to obtain the CFFs. Compton amplitudes are then evaluated in terms of these CFFs. It is worth noting that the LO contributions from the quark GPDs to the imaginary parts of the CFFs involve the GPDs at the point  $X = \zeta$ , rather than integrals over a range of  $X$  values. In other words, for a LO analysis, the quark GPDs at the point  $X = \zeta$  are accessible through some experimentally discernable quantities.

### 5.2.1 Observables

The theoretical expressions for the electron-proton or positron-proton scattering processes discussed in section 5.2 can be evaluated by comparing theo-

retical predictions to experimental data. Alternatively, parametric forms for the theoretical expressions can be fit to the experimental data. The DVCS experiments are not able to measure GPDs directly, but they are able to determine quantities and observables that receive contributions from the GPDs. The differential cross section from equation 5.2 is a useful observable, as is the equivalent expression for the positron-proton scattering process.

A separate amplitude can be calculated for each configuration of beam helicities, beam charges, and target polarization states, and so differential cross sections can be evaluated for each unique configuration. Experimental data can be gathered while using different beam and target configurations in order to obtain experimental values for these observables. The differential cross sections can then be combined in certain ways to form other observables, which include various cross sections and asymmetries. An asymmetry can be evaluated for any quantity that can take two opposite values, such as beam charge or beam helicity. These asymmetries are typically obtained by taking the difference between the differential cross section for one configuration and the differential cross section for the other configuration, and dividing the result by the sum of these two differential cross sections. There are some asymmetries that are a bit more complicated, as will be shown in section 5.2.2. Overall, asymmetries essentially quantify imbalances.

Recall that the total amplitude squared expressions for the electron-proton and positron-proton scattering processes involve contributions from a BH term, a DVCS term, and an interference term. For this analysis, the BH term is of

less interest than the DVCS and interference terms. This is because the BH term is calculable from known electromagnetic form factors, and does not involve the GPDs. Although both the DVCS and interference terms are beneficial for accessing the GPDs, it is worthwhile to note that the interference term allows for more direct access to the GPDs compared to the DVCS term. This is due to the fact that the interference term is linear in CFFs. The advantage of evaluating various observables is that some of them involve contributions from the DVCS term, the interference term, or both, without any contributions from the BH term. For example, the beam charge asymmetry isolates contributions from the interference term. This happens because the DVCS and BH amplitudes squared are proportional to even powers of the lepton charge, while the interference term is proportional to an odd power of the lepton charge. Taking the difference between the differential cross sections with opposite beam charges isolates contributions from the interference term.

It is also worthwhile to note that, for a spin  $\frac{1}{2}$  proton target, any single-spin asymmetry will not get contributions from the BH term. A single-spin asymmetry is an asymmetry that either involves different spin states for the beam, such as a beam helicity asymmetry, or different spin states for the target, such as a target polarization asymmetry. In contrast, a double-spin asymmetry involves different spin states for both the beam and the target. The BH terms do not contribute to any of the single-spin asymmetries because of constraints from parity and time reversal invariance. See [11] for a more detailed discussion, as well as a consideration of angular dependence.

Experimental data for other processes besides DVCS, such as DVMP, can also provide a connection to the GPDs. Experimentally determined values for DVMP observables, for example, are obtained in a similar way as for DVCS. Certain properties of the initial and final state particles involved in the experimental interactions can have multiple configurations. Differential cross sections can be evaluated from experimental data that is gathered while using various configurations for these properties. These differential cross sections can then be combined to form new cross sections and asymmetries. Theoretical predictions for observables can be evaluated and compared to the experimentally determined values. Observables for processes such as DVCS and DVMP are very useful for evaluating theoretical GPD models.

### 5.2.2 DVCS Observables

The following label scheme is used to indicate the beam charge, the beam helicity, and the target polarization. The charge of the lepton beam is indicated by the superscript label  $+$ ( $-$ ) indicating a positively (negatively) charged beam. For example,  $d\sigma^+$  is the cross section resulting from a positron beam. The superscript label  $\uparrow$  ( $\downarrow$ ) indicates a positive (negative) beam helicity. For example,  $d\sigma^\uparrow$  indicates that the beam has positive helicity. If either of these labels are omitted, it means that the different configurations for that label have been summed over.

In this convention, the target nucleon has a spin vector  $S = (S^0, \vec{S})$  that

has a polar angle  $\theta$  and an azimuthal angle  $\Phi$ . The spin vector is defined in terms of  $S_{LP} = (S_{LP}^0, \vec{S}_{LP})$ , the longitudinal part of the nucleon polarization vector, and  $S_{\perp} = (S_{\perp}^0, \vec{S}_{\perp})$ , the transverse part of the nucleon polarization vector, by the expression

$$S = \cos(\theta)S_{LP}(\Lambda) + \sin(\theta)S_{\perp}(\Phi) \quad (5.6)$$

In this convention,  $S_{LP}(\Lambda) = (0, 0, 0, \Lambda)$ , where  $\Lambda = \pm 1$  denotes a longitudinal polarization in the  $\pm z$  direction. The subscript label  $\uparrow$  ( $\downarrow$ ) indicates that the longitudinal part of the target polarization is in the positive (negative)  $z$  direction. In other words, the label  $\uparrow$  ( $\downarrow$ ) corresponds to  $\Lambda = +1$  ( $-1$ ). For example,  $d\sigma_{\downarrow}$  indicates that the longitudinal part of the target polarization is in the  $-z$  direction. In this convention,  $S_{\perp}(\Phi) = (0, \cos(\Phi), \sin(\Phi), 0)$ . It should be noted that there are other conventions that can also be used to define the kinematics and frame for the electron-proton and positron-proton scattering processes discussed in this section. In addition, different conventions may define the target spin vector differently. For the sake of convenience in comparing the target polarization between conventions, two additional terms are defined here. Using the convention established in this section,  $\vec{S}_L = \cos(\theta)\vec{S}_{LP}(\Lambda)$  and  $\vec{S}_T = \sin(\theta)\vec{S}_{\perp}(\Phi)$  to represent the longitudinal and transverse components of the spin vector  $\vec{S}$ .

One alternative convention is the Trento convention [28]. The angles and axes defined in the convention used in this section convert readily to the angles

and axes defined in the Trento convention. Using the frames and kinematics of the Trento convention, observables involving transverse target polarizations are associated with an angle  $\phi_S$ . This analysis uses the subscript label  $\Leftarrow$  ( $\Rightarrow$ ) to indicate the direction of the transverse part of the target polarization vector. The subscript label  $\Leftarrow$  indicates that there is an angle of  $\phi_S$  between the lepton scattering plane and the transverse part of the target polarization vector, while the subscript label  $\Rightarrow$  indicates that there is an angle of  $\phi_S + \pi$  between the lepton scattering plane and the transverse part of the target polarization vector. These angles defined based on the kinematics and frame of the Trento convention can be transformed into a corresponding set of angles that are defined with respect to the kinematics and frame of the original convention used in this section, and so this analysis will switch back to the original convention from here on. As before, if a label is omitted then it means the different configurations for that label have been summed over.

The observables can be given a labeling scheme that distinguishes which beam and target polarizations are involved. Each observable can take a subscript with two letters. The first letter can be  $L$ , to indicate that the observable isolates longitudinal beam polarizations,  $T$ , to indicate that the observable isolates transverse beam polarizations, or  $U$  for unpolarized, to indicate that the observable does not isolate beam polarization states. Similarly, the second letter can be  $L$ , to indicate that the observable isolates longitudinal target polarizations,  $T$ , to indicate that the observable isolates transverse target polarizations, or  $U$  for unpolarized, to indicate that the observable does not

isolate target polarization states. For example, the observable  $A_{LT}$  involves longitudinal beam polarizations and transverse target polarizations.

See reference [27] for a comprehensive list of the Fourier coefficients, in terms of electromagnetic form factors and the CFFs evaluated from the GPDs. For each of the coefficients associated with the CFFs, the level of twist, or levels of twist, of the contributing GPDs may vary. For example, the coefficient  $c_0^{\mathcal{I}}$  is given in terms of twist-two GPDs, while  $c_1^{DVCS}$  has contributions from twist-three GPDs. In this way, the GPDs with the desired level or levels of twist could potentially be isolated by considering only the relevant coefficients.

Several experimental groups have collected data for the  $(e + P \rightarrow e + P + \gamma)$  processes, as well as the corresponding processes with positrons in place of electrons. Collaborations such as HERMES, CLAS, H1, and others have conducted experiments and fit observables to their gathered data. The observables are often expanded in terms of their angular dependence, and so they are expressed in terms of Fourier harmonics. For example, in reference [39] the HERMES collaboration defines

$$\mathcal{A}_{LU}^I(\phi_{(tr)}) \simeq \sum_{n=1}^2 A_{LU,I}^{\sin(n\phi_{(tr)})} \sin(n\phi_{(tr)}) \quad (5.7)$$

where the angle  $\phi_{(tr)}$  represents what [39] labels as the angle  $\phi$  defined using the Trento convention, and the label  $I$  is interchangeable with the usual label  $\mathcal{I}$  to indicate contributions to the interference term. Keep in mind that the labeling scheme for the observable and the harmonic in equation 5.7 follow the

schemes in reference [39].

The observables are expanded in terms of Fourier harmonics, and experimental groups have obtained experimental values for several of these harmonics. These experimental values can then be related to the coefficients in equation 5.4, and by doing so they can be expressed in terms of electromagnetic form factors, GPDs, or both. Sample observables relevant to the GPDs are presented as the following expressions

$$\begin{aligned}
\frac{d\sigma}{d\Psi} &= \frac{1}{2} \left[ \frac{d^4\sigma^\uparrow}{d\Psi} + \frac{d^4\sigma^\downarrow}{d\Psi} \right] \\
A_{LU} &= \frac{\frac{d^4\sigma^\uparrow}{d\Psi} - \frac{d^4\sigma^\downarrow}{d\Psi}}{\frac{d^4\sigma^\uparrow}{d\Psi} + \frac{d^4\sigma^\downarrow}{d\Psi}} \\
A_C &= \frac{\frac{d^4\sigma^+}{d\Psi} - \frac{d^4\sigma^-}{d\Psi}}{\frac{d^4\sigma^+}{d\Psi} + \frac{d^4\sigma^-}{d\Psi}} \\
A_{UT}^{DVCS} &= \frac{1}{S_T} \frac{\left( \frac{d^4\sigma_{\Leftarrow}^+}{d\Psi} - \frac{d^4\sigma_{\Rightarrow}^+}{d\Psi} \right) + \left( \frac{d^4\sigma_{\Leftarrow}^-}{d\Psi} - \frac{d^4\sigma_{\Rightarrow}^-}{d\Psi} \right)}{\frac{d^4\sigma^+}{d\Psi} + \frac{d^4\sigma^-}{d\Psi}} \\
A_{UT}^I &= \frac{1}{S_T} \frac{\left( \frac{d^4\sigma_{\Leftarrow}^+}{d\Psi} - \frac{d^4\sigma_{\Rightarrow}^+}{d\Psi} \right) - \left( \frac{d^4\sigma_{\Leftarrow}^-}{d\Psi} - \frac{d^4\sigma_{\Rightarrow}^-}{d\Psi} \right)}{\frac{d^4\sigma^+}{d\Psi} + \frac{d^4\sigma^-}{d\Psi}} \tag{5.8}
\end{aligned}$$

where  $d\Psi = dQ^2 dx_B dt d\phi_{(tr)}$  and the  $S_T$  in the denominators denotes the magnitude of the transverse target polarization [38]. The observable  $A_C$  is the asymmetry associated with beam charge.



### 5.2.3 Experimental Data and Observables

Theoretical models for the GPDs can be evaluated by using experimental data. Predictions for the desired observables can be made from the GPD models and compared to the experimental values. Alternatively, the GPDs can be fit to the experimental data in a global fit procedure. Data can be collected for a number of observables, and the relevant GPDs can be fit simultaneously to the experimental data. It may be beneficial to obtain as much data for as many observables as possible in order to fit many GPDs together at the same time, or it may be useful to isolate a few GPDs at a time and sequentially fit subsets of parameters. In any case, the GPDs play an important role in the evaluation of observables for the  $(e + P \rightarrow e + P + \gamma)$  processes, as well as the corresponding processes with positrons in place of electrons.

In this section, values from experimental data are compared to predictions from theoretical models for several observables in different kinematic regions. Figure 5.4 displays the asymmetry  $A_{LU}$ . Figure 5.5 displays coefficients that contribute to the beam charge asymmetry  $A_C$ . Figure 5.6 displays coefficients that contribute to the asymmetries  $A_{UT}^{DVCS}$  and  $A_{UT}^I$ . Figure 5.7 displays the observable  $\frac{d\sigma}{d\Psi}$  from equation 5.8, as well as a corresponding observable that takes the difference between the helicity-dependent differential cross sections. These figures are taken directly from [33], and they showcase the theoretical models developed for that analysis.

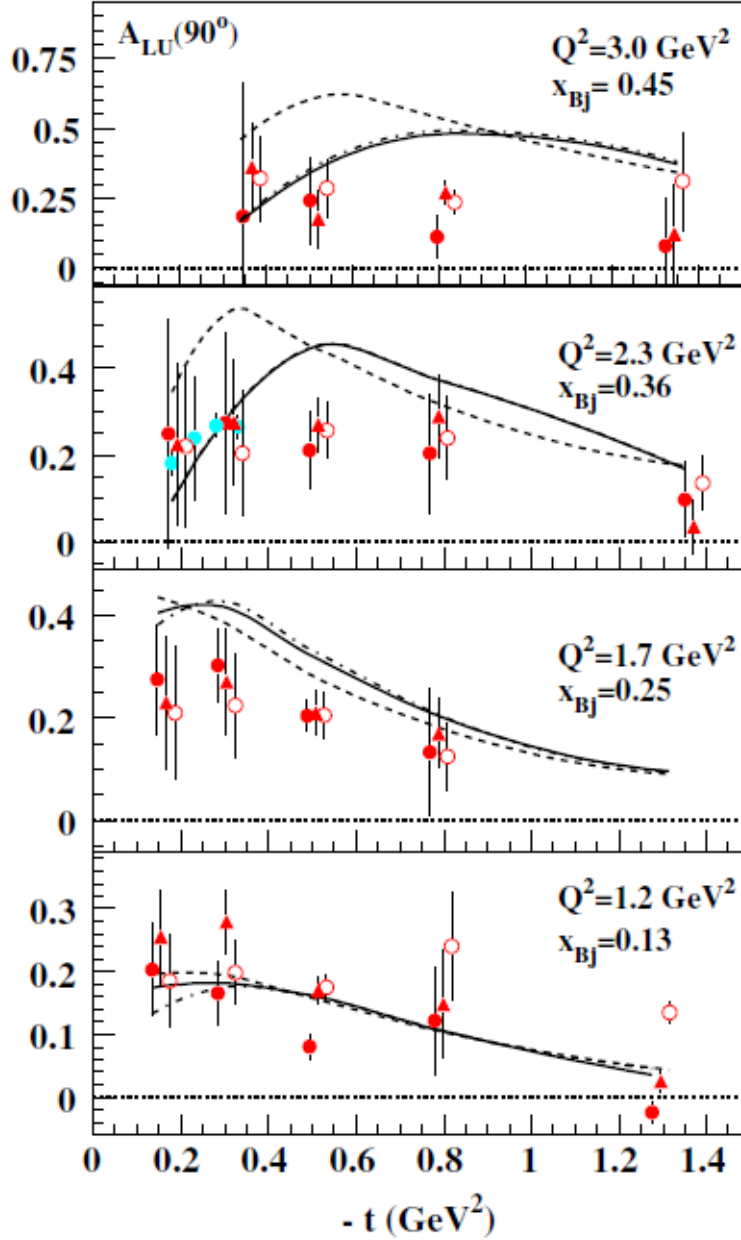


Figure 5.4: Values for  $A_{LU}(90^\circ)$  from experimental data collected by Hall A (blue points) and Hall B (red points), along with predictions for the theoretical values of the observable based on three unique GPD models. The open circles, full circles, and triangles represent data at  $Q^2$  values slightly displaced around the values displayed, in similar  $x_{Bj}$  and  $t$  bins. The error bands on the data points in the figure do not represent the uncertainties reported in the experimental analysis, as the statistical and systematic errors were added in quadrature and no error correlations were considered. The solid, dashed, and dot-dashed lines represent predictions using three different GPD models. The figure was taken directly from [33].

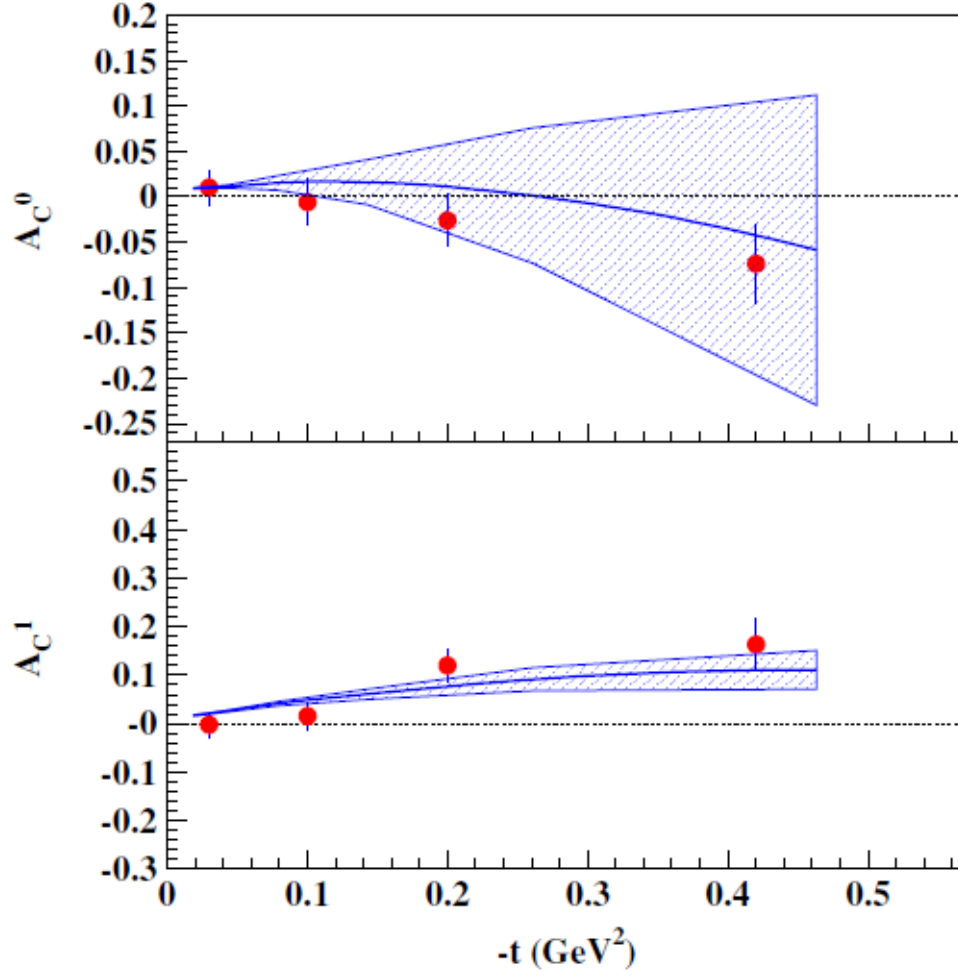


Figure 5.5: Values for  $A_C^{\cos(0\phi_{(tr)})}$  and  $A_C^{\cos(\phi_{(tr)})}$ , labeled here as  $A_C^0$  and  $A_C^1$  respectively, from experimental data collected by HERMES (red points). The blue lines and blue shaded portions represent the predictions for these observables based on theoretical GPD models. The figure was taken directly from [33].

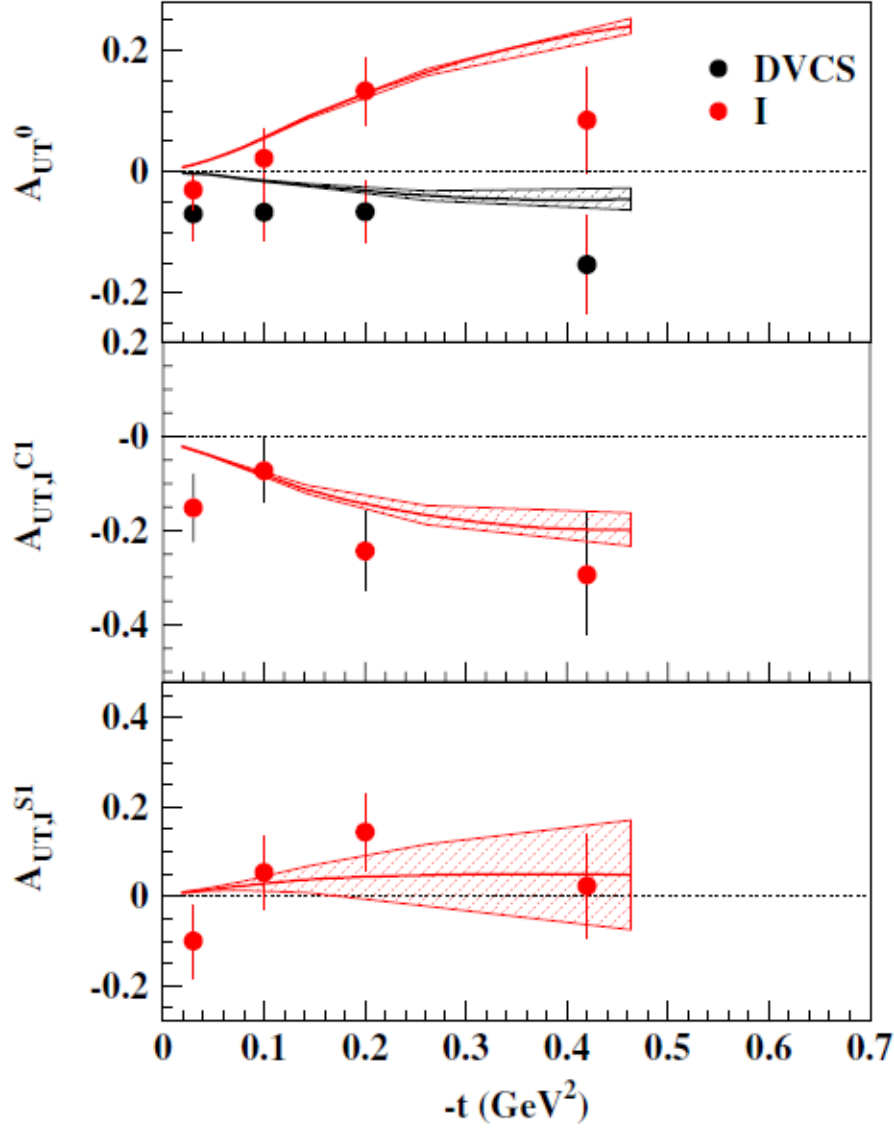


Figure 5.6: Values for  $A_{UT,DVCS}^{sin(\phi_{(tr)}-\phi_S)}$ ,  $A_{UT,I}^{sin(\phi_{(tr)}-\phi_S)}$ ,  $A_{UT,I}^{sin(\phi_{(tr)}-\phi_S)cos(\phi_{(tr)})}$ , and  $A_{UT,I}^{cos(\phi_{(tr)}-\phi_S)sin(\phi_{(tr)})}$  from experimental data collected by HERMES (black and red points) [38]. The first two observables are labeled here as  $A_{UT}^0$ , the third observable is labeled here as  $A_{UT,I}^{C1}$ , and the fourth observable is labeled here as  $A_{UT,I}^{S1}$ . The red and black lines as well as the red and black shaded portions represent the predictions for these observables based on theoretical GPD models. The figure was taken directly from [33].

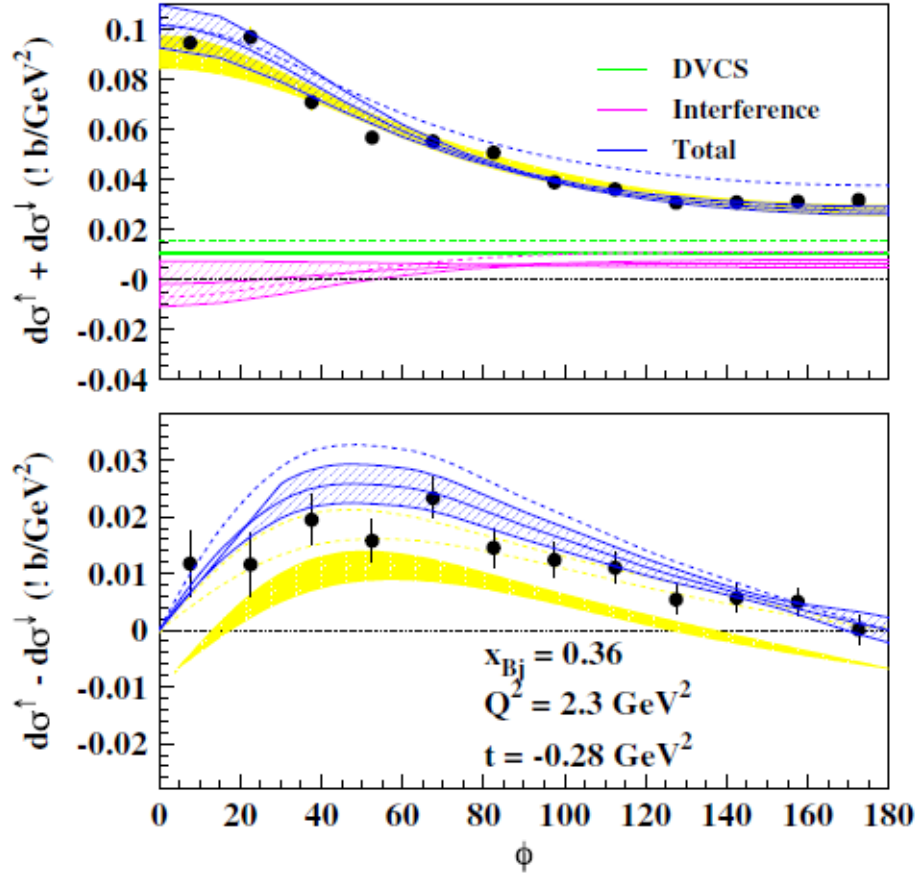


Figure 5.7: Values for  $\frac{d^4\sigma}{d^4\Phi}$  and  $\frac{d^4\Sigma}{d^4\Phi}$  from experimental data collected by Hall A (black points), using the notation in [43]. The first observable is labeled here as  $d\sigma^\uparrow + d\sigma^\downarrow$ , and the second observable is labeled here as  $d\sigma^\uparrow - d\sigma^\downarrow$ . The units for each are listed here as (! b/GeV<sup>2</sup>), while in [43] they are listed as (nb/GeV<sup>4</sup>). The azimuthal angle  $\phi_{\gamma\gamma}$  of the detected photon following the conventions and labels in [43] is represented here in units of degrees by the axis label  $\phi$ . The solid lines, dashed lines, and shaded portions that are colored blue, green, or purple represent predictions for these observables, or for contributions towards these observables from DVCS and interference terms, based on theoretical GPD models. The yellow band in the top graph represents the error of the data fit. The figure was taken directly from [33]. According to the caption of the figure in [33], the yellow band in the bottom graph represents the error of the data fit while a green band represents the theoretical error from their parametrization. Comparing this figure with the appropriate figure in [43], it is possible that the band formed by the dashed yellow lines in the bottom graph here represent the error of the data fit while the solid yellow band in the bottom graph here represents the theoretical error from the parametrization.

### 5.3 Accessing the Gluon GPDs

The DVCS and DVMP processes are ideal for evaluating leading twist quark and gluon GPDs, as the GPDs contribute to the various helicity amplitudes for these processes. Experimentally, the DVCS and DVMP interactions are typically generated by colliding either electrons or positrons with protons. Other processes, such as meson pair production, can also receive contributions from GPDs. This section will discuss the various processes that allow access to the gluon GPDs in particular. The GPDs discussed in this section are at leading twist. GPDs at higher levels of twist are beyond the scope of this analysis.

The helicity amplitudes for DVCS receive contributions from the "singlet" combinations of the helicity conserving quark GPDs starting at LO in  $\alpha_s$ , while they receive contributions from gluon GPDs starting at NLO. See section 1.5 for the definitions of the "singlet" combinations of the quark GPDs. The helicity conserving gluon GPDs contribute by means of the CFFs in equations 3.52 and 3.53. The helicity-flip gluon GPDs, which are discussed in section 5.6, contribute to DVCS amplitudes that involve a photon helicity flip. Theoretical expressions for the quark and gluon GPDs can be evaluated by using DVCS data. The expressions for the DVCS observables contain mingled contributions from quark and gluon GPDs. DVCS processes are useful for evaluating gluon GPDs, but there may be processes that offer cleaner access to the gluon GPDs without significant mingled contributions from quark GPDs.

DVMP processes offer more convenient access to helicity conserving gluon GPDs. More specifically, neutral vector meson production processes, such as the electroproduction of a  $\rho^0$ ,  $\omega$ , or  $\phi$  meson, are ideal for evaluating the unpolarized helicity conserving gluon GPDs. Contributions to these light meson electroproduction processes from unpolarized helicity conserving gluon GPDs dominate at small  $x_B$ , though the contributions from quark GPDs may become more significant when  $x_B$  is not small.  $J/\Psi$  production processes may also be useful for evaluating the unpolarized helicity conserving gluon GPDs, although the scale of  $Q^2$  in comparison to the charm quark and  $J/\Psi$  masses squared becomes relevant. See [11] for a more detailed discussion about the connection between the gluon GPDs and the  $(\gamma^{(*)} + P \rightarrow J/\Psi + P)$  processes. The gluon GPD  $\tilde{H}^g$ , on the other hand, is accessible through  $h_1$  production, where it contributes at  $O(\alpha_s^2)$ . However, experimental measurements of the  $h_1$  meson may be difficult to obtain.

There are also other methods for accessing the gluon GPDs. For example, gluon GPDs contribute to certain charged and neutral current production processes. Gluon GPDs can also contribute to the electroproduction of a  $\pi^+\pi^-$  pair or a  $K^+K^-$  pair. Overall, there are many ways to access the gluon GPDs. To summarize, DVCS processes are useful for accessing the full set of gluon GPDs. Certain vector meson production processes are ideal for accessing unpolarized helicity conserving gluon GPDs. Other processes, such as the electroproduction of certain meson pairs, allow for further access to gluon GPDs.

## 5.4 GPDs and Form Factors

As seen in equation (1.72), the integrals in  $x$  of the GPDs can be related to the Dirac, Pauli, axial, and pseudoscalar form factors. If the GPDs have been modeled and fit previously, they can be used to make predictions for the form factors. In this way, the GPD models can be evaluated for various  $\xi$  and  $t$  values. For example, the integrals in  $x$  from equation (1.72) should be independent of  $\xi$ . Alternatively, the form factor parametrizations can be used to fit several parameters for the GPDs in an iterative fit procedure. The form factor parametrizations can be used to fit several parameters that depend on  $t$ , and they contribute towards a fit of the functional polynomial parametrizations of the GPDs in the ERBL region. The form factors are useful for evaluating the dependence of the GPDs on  $\xi$  and  $t$ .

## 5.5 Impact Parameter Dependent Parton Distribution Functions

The GPDs are useful for describing the distribution of partons in terms of their transverse position. The following discussion relates the quark GPDs to the impact parameter dependent PDFs in the case that there is a purely transverse net momentum transfer ( $\xi = 0, \Delta^+ = 0, \Delta^- = 0$ ), using the kinematics and conventions from section 2.2. The impact parameter dependent PDF  $q(x, \vec{b}_\perp)$  describes the probability for a parton of flavor  $q$  ( $q = u, d, s, \dots$ ) to have a LC



momentum fraction of  $x$  and a transverse position  $\vec{b}_\perp$  defined relative to the proton's transverse center of momentum. The impact parameter dependent PDFs are related to the quark GPDs  $H_q(x, \xi, t)$  through the following relation [41]

$$q(x, \vec{b}_\perp) = \int \frac{d^2 \Delta_\perp}{(2\pi)^2} e^{i\vec{b}_\perp \cdot \vec{\Delta}_\perp} H_q(x, 0, -\Delta_\perp^2) \quad (5.9)$$

The mean squared transverse distance from the transverse center of momentum can be expressed as a function of  $x$  by

$$\langle b_\perp^2(x) \rangle_q = \frac{\int d^2 b_\perp q(x, \vec{b}_\perp) b_\perp^2}{\int d^2 b_\perp q(x, \vec{b}_\perp)} \quad (5.10)$$

These expressions give a good indication about the spread of partons within the proton, for a particular momentum fraction  $x$ . For example, the impact parameter dependent PDFs could hypothetically indicate that down quarks are clustered about the transverse center of momentum with a small mean squared transverse distance. See [42] for a more detailed discussion about the impact parameter dependent PDFs. See also [11] for a discussion of the impact parameter representation of GPDs in the general case where  $\xi$  can be nonzero.

There are additional impact parameter dependent PDFs to consider. A new set of impact parameter dependent PDFs,  $q_X(x, \vec{b}_\perp)$ , are defined for the case where the initial and final nucleon states are superpositions of  $+$  and  $-$  helicity states [42]. If the system was nonrelativistic, this would correspond

to initial and final state nucleons that are polarized in the  $x$  direction. The interpretation is not quite so simple for a relativistic system, but for the sake of this discussion it will be assumed that the nucleon states can be interpreted as being polarized in the  $x$  direction for the relativistic case as well. These new impact parameter dependent PDFs are defined as [42]

$$q_X(x, \vec{b}_\perp) = q(x, \vec{b}_\perp) - \frac{1}{2M} \frac{\partial}{\partial b_y} \mathcal{E}_q(x, \vec{b}_\perp) \quad (5.11)$$

where  $b_y$  is the  $y$  component of  $\vec{b}_\perp$ , and  $\mathcal{E}_q(x, \vec{b}_\perp)$  denotes the Fourier transform of  $E_q(x, 0, -\Delta_\perp^2)$

$$\mathcal{E}_q(x, \vec{b}_\perp) = \int \frac{d^2 \Delta_\perp}{(2\pi)^2} e^{i\vec{b}_\perp \cdot \vec{\Delta}_\perp} E_q(x, 0, -\Delta_\perp^2) \quad (5.12)$$

The  $q_X(x, \vec{b}_\perp)$  distributions account for distortions that are applied to the  $q(x, \vec{b}_\perp)$  distributions as a result of the nucleons being polarized in a transverse direction.

## 5.6 Helicity-Flip Gluon GPDs

This analysis derived expressions for the helicity conserving gluon GPDs. It is also possible to derive expressions for the helicity-flip gluon GPDs. The helicity-flip distributions were not given much consideration in this analysis, but they could benefit future studies, particularly those regarding DVCS. The same kinematics and conventions that were used to derive the helicity conserv-

ing GPDs are used here to derive the helicity-flip gluon GPDs. In the  $A^+ = 0$  gauge, the gluon helicity-flip GPDs are defined in terms of the following expansion

$$\begin{aligned}
& \frac{1}{\bar{P}^+} \int \frac{dz^-}{2\pi} e^{ix\bar{P}^+z^-} \langle P' | \mathbf{S} G^{+i} \left( -\frac{z}{2} \right) G^{j+} \left( \frac{z}{2} \right) | P \rangle \Big|_{z^+=0, \mathbf{z}_\perp=0} \\
&= \mathbf{S} \frac{1}{2\bar{P}^+} \frac{\bar{P}^+(-\Delta^j) - (-\Delta^+)\bar{P}^j}{2M\bar{P}^+} \bar{u}(P') \left[ H_T^g i\sigma^{+i} + \tilde{H}_T^g \frac{\bar{P}^+(-\Delta^i) - (-\Delta^+)\bar{P}^i}{M^2} \right. \\
&\quad \left. + E_T^g \frac{\gamma^+(-\Delta^i) - (-\Delta^+)\gamma^i}{2M} + \tilde{E}_T^g \frac{\gamma^+\bar{P}^i - \bar{P}^+\gamma^i}{M} \right] u(P) \quad (5.13)
\end{aligned}$$

where  $\mathbf{S}$  indicates a symmetrization of uncontracted Lorentz indices along with removal of the trace, and the indices  $i$  and  $j$  are restricted to the two transverse dimensions ( $i = 1, 2$  and  $j = 1, 2$ ).

In a procedure similar to the one described in section 1.4.3, the relevant LC helicity soft amplitudes can be expressed in terms of the helicity-flip GPDs in the following way.

$$\begin{aligned}
A_{++,+-}^{g(LC)} &= e^{2i\phi_D} \sqrt{1-\xi^2} \frac{t_0-t}{4M^2} \left( \tilde{H}_T^g + (1-\xi) \frac{E_T^g + \tilde{E}_T^g}{2} \right) \\
A_{-+,-}^{g(LC)} &= e^{2i\phi_D} \sqrt{1-\xi^2} \frac{t_0-t}{4M^2} \left( \tilde{H}_T^g + (1+\xi) \frac{E_T^g - \tilde{E}_T^g}{2} \right) \\
A_{++,-}^{g(LC)} &= e^{i\phi_D} (1-\xi^2) \frac{\sqrt{t_0-t}}{2M} \left( H_T^g + \frac{t_0-t}{4M^2} \tilde{H}_T^g - \frac{\xi^2}{1-\xi^2} E_T^g + \frac{\xi}{1-\xi^2} \tilde{E}_T^g \right) \\
A_{-+,-}^{g(LC)} &= -e^{3i\phi_D} (1-\xi^2) \frac{(t_0-t)^{\frac{3}{2}}}{8M^3} \tilde{H}_T^g \quad (5.14)
\end{aligned}$$

The interacting gluons are assumed to be massless. The interacting gluons are assumed to have large + lightcone momentum components compared to

their other momentum components. The initial state proton is assumed to have a large + lightcone momentum component and no transverse momentum, while the final state proton is assumed to have a large + lightcone momentum component compared to its other momentum components. In this limit, calculations using LC helicity are assumed to give identical results to calculations using ordinary helicity at the leading order in  $P^+$ . It is assumed that expressions relating the soft LC helicity amplitudes to the helicity-flip GPDs can substitute the soft LC helicity amplitudes for the soft helicity amplitudes that are obtained using the spectator model with ordinary helicity, along with the appropriate corrections such as the extra kinematics discussed in section 3.5. The relevant soft parton helicity-flip amplitudes using the spectator model and ordinary helicity are obtained using the same framework and methods from chapter 3 that were used to calculate the relevant soft parton helicity conserving amplitudes. These soft parton helicity-flip amplitudes are expressed as

$$\begin{aligned}
A_{++,+}^g &= \int d^2 k_\perp \mathcal{A}^g \left[ (-1)(1-X) \frac{(k_1 + ik_2)(\tilde{k}_1 + i\tilde{k}_2)}{XX'} \right] \\
A_{-+,-}^g &= \int d^2 k_\perp \mathcal{A}^g \left[ (-1)(1-X') \frac{(k_1 + ik_2)(\tilde{k}_1 + i\tilde{k}_2)}{XX'} \right] \\
A_{++,-}^g &= \int d^2 k_\perp \mathcal{A}^g \left[ \left( (1-X)M - M_X \right) \frac{(\tilde{k}_1 + i\tilde{k}_2)}{X'} - \left( (1-X')M - M_X \right) \frac{(k_1 + ik_2)}{X} \right] \\
A_{-+,-}^g &= 0
\end{aligned} \tag{5.15}$$

With the common factor

$$\mathcal{A}^g = \frac{\mathcal{N}^g}{\sqrt{1-X}\sqrt{1-X'}(1-X)P^+} \frac{1}{(k^2 - M_\Lambda^2)^2(k'^2 - M_\Lambda^2)^2} \quad (5.16)$$

The helicity-flip GPDs are calculated by replacing the LC helicity amplitudes on the left side of equation 5.14 with the soft amplitudes on the left side of equation 5.15, and then multiplying the soft amplitudes by a factor of  $\frac{X(X-\zeta)P^+}{1-\frac{\zeta}{2}}$  to account for the extra kinematics. The superscript labels (sp) are added to the GPDs on the right hand side, to indicate that these are the contributions to the full GPD expressions from the spectator model amplitudes.

It is convenient to define a new set of distributions

$$F_T^{g(sp)} = \mathcal{N}^g F_T^{g(h)} \quad (5.17)$$

where  $F_T = H_T, E_T, \tilde{H}_T, \tilde{E}_T$ , and  $\mathcal{N}^g$  is the constant in equation 5.16. The new distributions with the (h) label are defined to emphasize the variable content of the GPDs, as derived from the soft helicity amplitudes, separately from any constant factors.

## 5.7 Concluding Remarks and Outlook

The spectator model has provided a useful framework for modeling the generalized parton distributions. Previous studies have modeled the parton helicity conserving and parton helicity-flip valence quark GPDs at leading twist by

using the framework of the spectator model. These valence quark GPDs are modeled over the ERL and DGLAP regions, and several parameters have been fit as part of an iterative fit procedure. This analysis has expanded upon the previous studies by modeling the parton helicity conserving sea quark GPDs and parton helicity conserving gluon GPDs at leading twist by using the framework of the spectator model. These GPDs have been modeled in the ERL and DGLAP regions. The helicity conserving antiquark GPDs could potentially be modeled by using the framework of the spectator model discussed in this analysis, or they could potentially be related to the valence and sea quark GPDs. Several parameters have been fit for the gluon and sea quark GPDs in this analysis.

Future studies could expand upon this analysis in many ways. For example, several more parameters in the DGLAP and ERL regions remain to be fit for the sea quark and gluon GPDs. The antiquark GPDs could potentially be modeled in full, and all relevant parameters could be fit. The helicity-flip GPDs could be modeled in full for sea quarks, antiquarks, and gluons by using the framework of the spectator model. Future studies may also model the GPDs at higher levels of twist. In addition, new models with partonic interpretations could be created for the GPDs in the ERL region, to replace the currently used functional polynomial forms. The spectator model could potentially provide the basis for fully modeling quark, antiquark, and gluon GPDs at various levels of twist.

The GPDs play a significant role in modeling electron-proton and positron-

proton scattering processes. If GPDs at various levels of twist have been modeled previously using the framework of the spectator model, then the GPD models can be used to make predictions on the expected values of observables. Alternatively, several of the GPD parameters can be fit simultaneously to DIS and DVCS data in a global fit procedure. The GPDs have many other useful applications as well. They have a connection to Dirac, Pauli, axial, and pseudoscalar form factors. They have a connection to polarized and unpolarized PDFs. The GPDs can also be used to make predictions on parton density distributions with respect to both the parton's LC plus component momentum fraction,  $x$ , and the parton's transverse position vector  $\vec{b}_\perp$  which lies in the plane that is transverse to the proton's direction of motion [34]. They can also be used to make predictions for the total angular momentum and orbital angular momentum of partons within the proton. Future studies could potentially use the framework of the spectator model and build off of the sea quark and gluon GPD models from this analysis in order to form a full set of models for the GPDs. Afterwards, these GPD models could be implemented in a variety of applications. The outlook for the GPDs and the spectator model is very promising.

# Appendix A

## Acronyms

<b>BH</b>	Bethe-Heitler
<b>CFF</b>	Compton Form Factor
<b>DGLAP</b>	Dokshitzer, Gribov, Lipatov, Altarelli, Parisi
<b>DIS</b>	Deep Inelastic Scattering
<b>DVCS</b>	Deeply Virtual Compton Scattering
<b>DVMP</b>	Deeply Virtual Meson Production
<b>ERBL</b>	Efremov, Radyushkin, Brodsky, Lepage
<b>GPD</b>	Generalized Parton Distribution
<b>LC</b>	Light-Cone
<b>LO</b>	Leading Order
<b>NLO</b>	Next-to-Leading Order



<b>PDF</b>	Parton Distribution Function
<b>pQCD</b>	Perturbative Quantum Chromodynamics
<b>QCD</b>	Quantum Chromodynamics
<b>TCS</b>	Time-like Compton Scattering
<b>TMD</b>	Transverse-Momentum Distribution

# Appendix B

## GPD Parametrizations

The GPDs can be expressed as analytic integrals in terms of  $\kappa \equiv k_\perp^2$  and the angle  $\phi$ , where in this Appendix  $\phi$  is the angle  $\vec{k}_\perp$  makes with respect to  $\vec{\Delta}_\perp$ .

It is useful to first define the following notations:

$$L^2(X) = XM_X^2 + (1 - X)M_\Lambda^2 - X(1 - X)M_p^2$$

$$D^2(X') \equiv (1 - X')^2 \Delta_\perp^2$$

$$\mu = m_q + XM_p, \quad \mu' = m_q + X'M_p$$

$$M_{p-x} = (1 - X)M_p - M_X, \quad M'_{p-x} = (1 - X')M_p - M_X$$

$$Y_\pm = \left(1 \pm \frac{(1 - X)^2}{1 - \zeta}\right)$$

$$X' = \frac{X - \zeta}{1 - \zeta}$$

$$A = [L^2(X') + (1 - X')^2 \Delta_\perp^2]^2 = [L^2(X') + D^2(X')]^2$$

$$B = 2[L^2(X') - (1 - X')^2 \Delta_\perp^2] = 2[L^2(X') - D^2(X')]$$

where  $M_P$  is the proton's mass. It is useful to expand the denominators in these terms:

$$\begin{aligned}
k^2 - M_\Lambda^2 &= \frac{-1}{(1-X)}[L^2(X) + \kappa] \\
k'^2 - M_\Lambda^2 &\equiv a - b \cos \phi \\
a &= \frac{-1}{(1-X')}[L^2(X') + D^2(X') + \kappa], \quad b = \frac{-1}{(1-X')}[2(1-X')k_\perp \Delta_\perp]
\end{aligned} \tag{B.1}$$

The full expression for any helicity conserving valence quark, sea quark, or gluon GPD labeled as  $F$  is given by

$$F = \mathcal{N}_F R_F F^{(h)} \tag{B.2}$$

where  $\mathcal{N}_F$  is a parameter that scales the GPD, and  $R_F$  is the Regge term. The label  $F = H, E, \tilde{H}$ , or  $\tilde{E}$ , and the labels indicating the parton type and flavor have been omitted for simplicity. The distribution  $F^{(h)}$  is derived from soft helicity amplitudes.

Each of the quark and gluon GPDs can be expressed using the following general form:

$$F^{(h)} = G_1 \int_0^{2\pi} d\phi \int_0^\infty k_\perp dk_\perp \frac{C_1 + C_2 \cos(\phi)}{(k^2 - M_\Lambda^2)^n (a - b \cos(\phi))^n} + G_2 \tag{B.3}$$

where  $n=2$  for valence quarks and gluons, and  $n=3$  for sea quarks.

The integral over  $\phi$  has an analytic form and is solved first. These integrals are analytic in the limit that  $a > |b|$ . This condition cannot be satisfied for  $a < 0$ , so it is useful to use the sign of  $a$ , given by  $S_a$ , to define a new variable  $a'$  that will never be negative along with a variable  $b'$ .

$$\frac{a}{|a|} \equiv S_a, \quad S_a a \equiv a', \quad S_a b \equiv b' \quad (\text{B.4})$$

$$\frac{1}{(a - b \cos(\phi))^n} = \frac{(S_a)^n}{(S_a a - S_a b \cos(\phi))^n} \equiv \frac{(S_a)^n}{(a' - b' \cos(\phi))^n} \quad (\text{B.5})$$

The GPD expressions involve integrals of the following form

$$\int_0^{2\pi} d\phi \frac{f(\phi)}{(a - b \cos(\phi))^n} = (S_a)^n \int_0^{2\pi} d\phi \frac{f(\phi)}{(a' - b' \cos(\phi))^n} \quad (\text{B.6})$$

where  $f(\phi)$  is either 1 or  $\cos(\phi)$ .

For integrals with  $n = 2$  or 3, the analytic solutions take the following form for  $a' > |b'|$ :

$$t_2 = \int_0^{2\pi} d\phi \frac{1}{(a - b \cos(\phi))^2} = (S_a)^2 \int_0^{2\pi} d\phi \frac{1}{(a' - b' \cos(\phi))^2} = 2\pi \frac{a'}{(a'^2 - b'^2)^{\frac{3}{2}}} \quad (\text{B.7})$$

$$g_2 = \int_0^{2\pi} d\phi \frac{\cos(\phi)}{(a - b \cos(\phi))^2} = (S_a)^2 \int_0^{2\pi} d\phi \frac{\cos(\phi)}{(a' - b' \cos(\phi))^2} = 2\pi \frac{b'}{(a'^2 - b'^2)^{\frac{3}{2}}} \quad (\text{B.8})$$

$$t_3 = \int_0^{2\pi} d\phi \frac{1}{(a - b \cos(\phi))^3} = (S_a)^3 \int_0^{2\pi} d\phi \frac{1}{(a' - b' \cos(\phi))^3} = S_a \pi \frac{2a'^2 + b'^2}{(a'^2 - b'^2)^{\frac{5}{2}}} \quad (\text{B.9})$$

$$g_3 = \int_0^{2\pi} d\phi \frac{\cos(\phi)}{(a - b \cos(\phi))^3} = (S_a)^3 \int_0^{2\pi} d\phi \frac{\cos(\phi)}{(a' - b' \cos(\phi))^3} = S_a \pi \frac{3a'b'}{(a'^2 - b'^2)^{\frac{5}{2}}} \quad (\text{B.10})$$

To be completely rigorous, it should be shown that  $a' > |b'|$  for each set of

GPD parameters. In order to accomplish this, it is satisfactory to show that  $L^2(X) > 0$  for all  $X$  ranging from 0 to 1. This condition is met for every set of GPD fit parameters discussed in this analysis. For each of these sets of parameters, the following relation is also true.

$$(a'^2 - b'^2)^{m/2} = \frac{1}{(1 - X')^m} [A + B\kappa + \kappa^2]^{m/2} \quad (\text{B.11})$$

After completing the integration over  $\phi$ , the sea and gluon GPDs can be expressed as:

$$F^{(h)}(X, \zeta, t) = G_1 \int_0^\infty k_\perp dk_\perp \frac{C_1 \cdot t_n + C_2 \cdot g_n}{(k^2 - M_\Lambda^2)^n} + G_2$$

where  $n=2$  for valence quarks and gluons,  $n=3$  for sea quarks. See next page for lists of  $G_1$ ,  $G_2$ ,  $C_1$ , and  $C_2$  for sea quarks and gluons. The parameters are not provided here for valence quarks.

For sea Quarks :

$$G_1^H = \frac{(1 - \frac{\zeta}{2})}{1 - X}$$

$$G_2^H = \frac{\zeta^2}{4(1 - \zeta)} E_q$$

$$C_1^H = \left(m + MX\right) \left(m + M \frac{X - \zeta}{1 - \zeta}\right) + k_\perp^2$$

$$C_2^H = -k_\perp \Delta_\perp \frac{1 - X}{1 - \zeta}$$

$$G_1^E = \frac{-2M(1 - \zeta)}{1 - X}$$

$$G_2^E = 0$$

$$C_1^E = -\frac{1 - X}{1 - \zeta} (m + MX)$$

$$C_2^E = \left[ \left(m + MX\right) - \left(m + M \frac{X - \zeta}{1 - \zeta}\right) \right] k_\perp \frac{\Delta_\perp}{\Delta_\perp^2}$$

For Gluons :

$$G_1^H = \frac{1}{(1-X)^2}$$

$$G_2^H = \frac{\zeta^2}{4(1-\zeta)} E_g$$

$$C_1^H = X(X-\zeta)((1-X)M - M_X) \left( \frac{1-X}{1-\zeta} M - M_X \right) + (1-\zeta) \left( 1 + \frac{(1-X)^2}{1-\zeta} \right) k_\perp^2$$

$$C_2^H = - \left[ (1-X) \left( 1 + \frac{(1-X)^2}{1-\zeta} \right) \right] k_\perp \Delta_\perp$$

$$G_1^E = \frac{-2M(1-\zeta)}{1-X} \frac{1}{(1-\frac{\zeta}{2})}$$

$$G_2^E = 0$$

$$C_1^E = - \frac{1-X}{1-\zeta} X((1-X)M - M_X)$$

$$C_2^E = \left[ X((1-X)M - M_X) - (X-\zeta) \left( \frac{1-X}{1-\zeta} M - M_X \right) \right] k_\perp \frac{\Delta_\perp}{\Delta_\perp^2}$$

It is also useful to express the GPDs as analytic integrals in terms of  $\kappa \equiv k_{\perp}^2$ .

The expressions for the valence quark GPDs are presented in [33]

Each of the sea quark GPDs can be expressed using the following form

$$F_q^{(h)}(X, \zeta, t) = \pi \mathcal{G}_1 (1-X)^{5/2} (1-X')^{5/2} (-S_a) \\ \times \int_0^\infty \frac{d\kappa}{[\kappa + L^2(X)]^3} \frac{g_0 + g_1 \kappa + g_2 \kappa^2 + g_3 \kappa^3}{[A + B\kappa + \kappa^2]^{5/2}} + \mathcal{G}_2 \quad (\text{B.12})$$

Each of the gluon GPDs can be expressed using the following form

$$F_g^{(h)}(X, \zeta, t) = \pi \mathcal{G}_1 (1-X)^{3/2} (1-X')^{3/2} (-S_a) \\ \times \int_0^\infty \frac{d\kappa}{[\kappa + L^2(X)]^2} \frac{g_0 + g_1 \kappa + g_2 \kappa^2}{[A + B\kappa + \kappa^2]^{3/2}} + \mathcal{G}_2 \quad (\text{B.13})$$



For Sea Quarks :

$$\mathcal{G}_1^H = \frac{(1 - \frac{\zeta}{2})}{\sqrt{1 - \zeta}}$$

$$\mathcal{G}_2^H = \frac{\zeta^2}{4(1 - \zeta)} E_q$$

$$g_0^H = \mu\mu' \left( L^2(X') + D^2(X') \right)^2$$

$$g_1^H = 2\mu\mu' \left( L^2(X') + 2D^2(X') \right) \\ + \left( L^2(X') + D^2(X') \right) \left( L^2(X') - 2D^2(X') \right)$$

$$g_2^H = \mu\mu' + \left( 2L^2(X') + D^2(X') \right)$$

$$g_3^H = 1$$

$$\mathcal{G}_1^E = 2 \frac{(1 - X)}{\sqrt{1 - \zeta}}$$

$$\mathcal{G}_2^E = 0$$

$$g_0^E = \mu M_p \left( L^2(X') + D^2(X') \right)^2$$

$$g_1^E = M_p \left[ -\mu \left( L^2(X') - D^2(X') \right) + 3\mu' \left( L^2(X') + D^2(X') \right) \right]$$

$$g_2^E = -M_p(2\mu - 3\mu')$$

$$g_3^E = 0$$

For  $\tilde{H}$ , start with the same expressions as for  $H$  and then make the following changes:

Reverse the sign of  $g_0^H$ ,  $g_1^H$ ,  $g_2^H$ , and  $g_3^H$ . Next, replace  $(\mu' \rightarrow -\mu')$  but keep  $\mu$  the same.

For  $\tilde{E}$ , start with the same expressions as for  $E$  and then make the following changes: Replace  $(\mu' \rightarrow -\mu')$  but keep  $\mu$  the same. Use  $\mathcal{G}_1^{\tilde{E}} = \frac{2(1-\frac{\zeta}{2})}{\zeta} \mathcal{G}_1^E$

For Gluons :

$$\mathcal{G}_1^H = \frac{\sqrt{1-\zeta}}{(1-X)}$$

$$\mathcal{G}_2^H = \frac{\zeta^2}{4(1-\zeta)} E_g$$

$$g_0^H = XX' M_{p-x} M'_{p-x} \left( L^2(X') + D^2(X') \right)$$

$$g_1^H = \left( XX' M_{p-x} M'_{p-x} \right) + Y_+ \left( L^2(X') - D^2(X') \right)$$

$$g_2^H = Y_+$$

$$\mathcal{G}_1^E = 2 \frac{\sqrt{1-\zeta}}{(1-\frac{\zeta}{2})}$$

$$\mathcal{G}_2^E = 0$$

$$g_0^E = (1-X') X M_{p-x} M_p \left( L^2(X') + D^2(X') \right)$$

$$g_1^E = -M_p \left( (1-X') X M_{p-x} - 2(1-X) X' M'_{p-x} \right)$$

$$g_2^E = 0$$

For  $\tilde{H}$ , start with the same expressions as for  $H$  and then make the following changes:

Replace  $(Y_+ \rightarrow Y_-)$ .

For  $\tilde{E}$ , start with the same expressions as for  $E$  and then make the following changes:

Replace  $(M'_{p-x} \rightarrow -M'_{p-x})$  but keep  $M_{p-x}$  the same. Use  $\mathcal{G}_1^{\tilde{E}} = \frac{2(1-\frac{\zeta}{2})}{\zeta} \mathcal{G}_1^E$

# Appendix C

## Gordon Identities

The Gordon identities are given here for protons of equal mass  $m$ , with four-momenta  $p$  and  $p'$ .

The vector and axial vector expressions are

$$\begin{aligned} 2m\bar{u}(p')\gamma^\alpha u(p) &= \bar{u}(p')\left[(p' + p)^\alpha + i\sigma^{\alpha\beta}(p' - p)_\beta\right]u(p) \\ 2m\bar{u}(p')\gamma^\alpha\gamma_5 u(p) &= \bar{u}(p')\left[\gamma_5(p' - p)^\alpha + i\sigma^{\alpha\beta}\gamma_5(p' + p)_\beta\right]u(p) \end{aligned} \quad (\text{C.1})$$

The following expressions are useful for deriving other identities [10].

$$\begin{aligned} 0 &= \bar{u}(p')\left[(p' - p)^\alpha + i\sigma^{\alpha\beta}(p' + p)_\beta\right]u(p) \\ 0 &= \bar{u}(p')\left[\gamma_5(p' + p)^\alpha + i\sigma^{\alpha\beta}\gamma_5(p' - p)_\beta\right]u(p) \end{aligned} \quad (\text{C.2})$$

The expressions in C.1 and C.2 are contracted with different combinations of  $p_\alpha$  and  $p'_\alpha$  in order to obtain scalar and pseudoscalar expressions. The following properties are useful as well.

$$(\not{p} - m)u(p) = 0$$

$$\bar{u}(p')(\not{p}' - m) = 0$$

The scalar and pseudoscalar expressions are

$$\begin{aligned}\bar{u}(p')u(p) &= \bar{u}(p')\frac{i\sigma^{\alpha\beta}p'_\alpha p_\beta}{p'_\mu p^\mu - m^2}u(p) \\ \bar{u}(p')\gamma_5 u(p) &= \bar{u}(p')\frac{-i\sigma^{\alpha\beta}(p'_\alpha + p_\alpha)(p'_\beta - p_\beta)\gamma_5}{2(p'_\mu p^\mu + m^2)}u(p)\end{aligned}\tag{C.3}$$

# Appendix D

## QCD Evolution Equations

In chapter 1, Parton Distribution Functions are defined by considering deep inelastic lepton-proton scattering differential cross sections. The PDFs can also be derived from DIS differential cross sections [26]. The amplitudes for these processes involve a proton emitting a quark and leaving behind a hadronic final state. All possible configurations of the hadronic final state will be summed over. Alternatively, the proton can emit an antiquark or a gluon in place of the quark. In each case, the emitted parton will undergo a hard scattering process with the incoming virtual photon. As usual, the relevant hard processes can be sorted based on their order in  $\alpha_s$ , and then each associated amplitude can be evaluated separately.

The possible hard subprocesses that involve the photon interacting directly with a quark are discussed first. At the lowest order in  $\alpha_s$ , the photon will interact directly with an incoming quark. There are several subprocesses that give contributions at the next order. In one case, an incoming quark can

emit a gluon before interacting directly with the photon. Alternatively, the incoming quark can interact directly with the photon before emitting a gluon. In another case, an incoming gluon can produce a quark and antiquark pair, and the resulting quark can interact directly with the photon. See figure D.1 for diagrams of these four hard subprocesses. There are, of course, many other diagrams that contribute at different orders in  $\alpha_s$ .

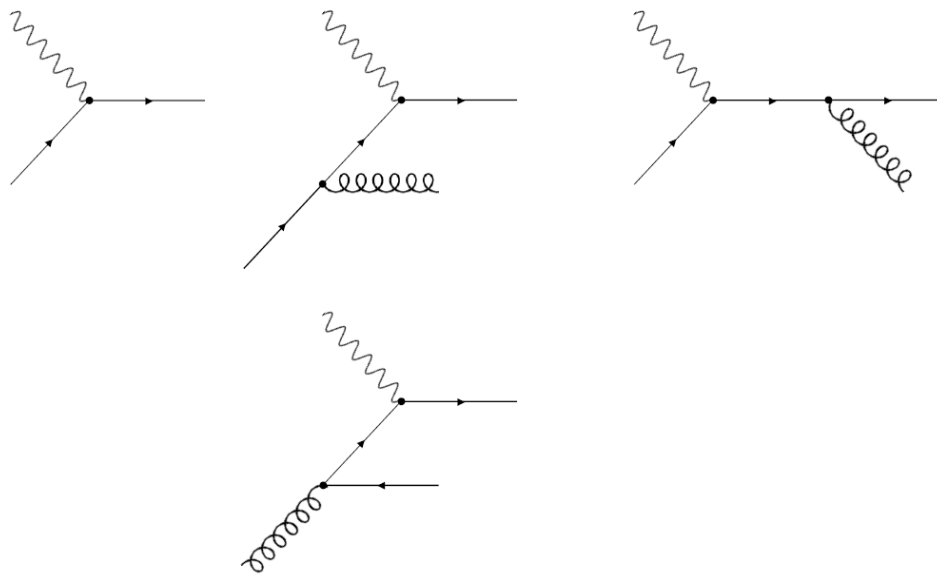


Figure D.1: Diagrams of the hard subprocesses that involve the virtual photon interacting directly with a quark. The top left diagram gives the leading contribute in  $\alpha_s$ . The remaining three diagrams give contributions at the next order in  $\alpha_s$ . The top center and top right diagrams involve the emission of a gluon. The bottom diagram begins with an incoming gluon, which was originally emitted by the proton, that splits into a quark and antiquark pair.

In general, each hard amplitude diagram has an incoming parton carrying a particular fraction of the initial proton's plus momentum component. Any number of basic QCD processes can occur before the photon interacts with anything. Any quark or antiquark can emit a gluon, and any gluon can produce

a quark and antiquark pair. Alternatively, any quark or antiquark can absorb a gluon, and any quark and antiquark pair can annihilate and produce a gluon. There are also contributing interactions that involve a triple or a quadruple gluon vertex. Each of the relevant hard amplitude diagrams at any desired order in  $\alpha_s$  can be constructed by starting with the incoming parton and virtual photon, and then applying valid combinations of QCD processes. The photon will interact with an object that is not necessarily the same type or flavor as the incoming parton. The object the photon interacts with may also have a different momentum fraction than the initial momentum fraction of the incoming parton. As a result, it is useful to define splitting functions in order to derive the QCD evolution equations. As a side note, see reference [26] for a discussion of parton fragmentation and recombination.

The splitting functions  $P_{BA}(z, \alpha_s)$  are associated with the set of combinations of the basic QCD processes described earlier that start with one object of type  $A$  and have a final state that includes an object of type  $B$ . The dimensionless variable  $z$  is the ratio of the momentum fractions of the two objects ( $z = x_B/x_A$ ). Each splitting function has a perturbative expansion with contributions at different orders in  $\alpha_s$ , with the form given by

$$P_{BA}(z, \alpha_s) = P_{BA}^{(0)}(z) + \frac{\alpha_s}{2\pi} P_{BA}^{(1)}(z) + \dots \quad (\text{D.1})$$

where the ... denotes higher order terms in  $\alpha_s$ .

Several of the diagrams for the hard amplitudes introduce divergences when



the full amplitude squared is evaluated. It becomes necessary to introduce a factorization scale for the PDFs. The PDFs at the scale defined by  $\mu^2$  with momentum fraction  $x$ , labeled as  $q(x, \mu^2)$ ,  $g(x, \mu^2)$ , and  $\bar{q}(x, \mu^2)$ , are defined in terms of the unmeasurable, bare distributions  $q_0(x)$ ,  $g_0(x)$ , and  $\bar{q}_0(x)$ . The QCD evolution equations describe how a set of PDFs at a particular energy scale change as the energy scale changes.

This section follows the conventions given by [24] for evaluating the leading order (Dokshitzer)-Gribov-Lipatov-Altarelli-Parisi, or (D)GLAP, evolution equations. The PDFs are given at a particular scale defined by  $t = \mu^2$  with momentum fraction  $x$ . The quark PDFs are given by  $q_i(x, t)$ , where  $q_i$  denotes the quark flavor ( $q_i = u, d, s, c, \dots$ ). Similarly, the antiquark PDFs are given by  $\bar{q}_i(x, t)$ , and new distributions are defined as  $q_i^\pm(x, t) = q_i(x, t) \pm \bar{q}_i(x, t)$ . The gluon PDF is given by  $g(x, t)$ . It is also useful to define non-singlet and singlet combinations of the quark distributions. The non-singlet distributions are given by

$$\begin{aligned}
V_i &= q_i^- \\
T_3 &= u^+ - d^+ \\
T_8 &= u^+ + d^+ - 2s^+ \\
T_{15} &= u^+ + d^+ + s^+ - 3c^+ \\
T_{24} &= u^+ + d^+ + s^+ + c^+ - 4b^+ \\
T_{35} &= u^+ + d^+ + s^+ + c^+ + b^+ - 5t^+
\end{aligned} \tag{D.2}$$

where the labels  $(x, t)$  are implicit. The singlet distribution is given by

$$\Sigma(x, t) = \sum_i q_i^+(x, t) \quad (\text{D.3})$$

For simplicity, the splitting functions will all be evaluated at LO. The full splitting function expressions can be expanded in terms of contributions at different orders of  $\alpha_s$ , as given in equation D.1. At LO, the evolution equations are defined in terms of the following four contributions from the splitting functions.

$$\begin{aligned} P_{qq}^{(0)}(z) &= C_F \left[ \frac{1+z^2}{(1-z)_+} + \frac{3}{2} \delta(1-z) \right], \\ P_{qg}^{(0)}(z) &= T_R \left[ z^2 + (1-z)^2 \right], \\ P_{gq}^{(0)}(z) &= C_F \left[ \frac{1+(1-z)^2}{z} \right], \\ P_{gg}^{(0)}(z) &= 2C_A \left[ \frac{z}{(1-z)_+} + \frac{1-z}{z} + z(1-z) \right] + \delta(1-z) \frac{(11C_A - 4n_f T_R)}{6} \end{aligned} \quad (\text{D.4})$$

where  $T_R = \frac{1}{2}$ , and  $n_f$  is the number of contributing flavors. In the case of the SU(3) color group,  $C_A = 3$  and  $C_F = \frac{4}{3}$ . The terms with  $(1-z)_+$  in the denominator are treated in a special way. Integrals that contain the term  $\frac{1}{(1-z)_+}$  along with any sufficiently smooth distribution  $f(z)$  are treated in the following way.

$$\int_0^1 dz \frac{f(z)}{(1-z)_+} = \int_0^1 dz \frac{f(z) - f(1)}{1-z} \quad (\text{D.5})$$

with the condition

$$\frac{1}{(1-z)_+} = \frac{1}{1-z} \quad \text{for } 0 \leq z < 1. \quad (\text{D.6})$$

The LO evolution equation takes a similar form for each of the non-singlet distributions defined in equation D.2. At leading order, the evolution equation for a non-singlet distribution labeled by  $V$  is given by

$$t \frac{\partial}{\partial t} V(x, t) = \frac{\alpha_s(t)}{2\pi} \int_x^1 \frac{d\xi}{\xi} P_{qq}^{(0)}(z) V(\xi, t) \quad (\text{D.7})$$

where  $z \equiv \frac{x}{\xi}$  and  $V$  is any one of the non-singlet distributions in equation D.2 ( $V = V_i, T_3, T_8, \dots$ ). The evolution of the singlet distribution is coupled with that of the gluon distribution. The evolution equations at leading order for the singlet and gluon distributions are presented in matrix form as

$$t \frac{\partial}{\partial t} \begin{pmatrix} \Sigma(x, t) \\ g(x, t) \end{pmatrix} = \frac{\alpha_s(t)}{2\pi} \int_x^1 \frac{d\xi}{\xi} \begin{pmatrix} P_{qq}^{(0)}(z) & 2n_f P_{qg}^{(0)}(z) \\ P_{gq}^{(0)}(z) & P_{gg}^{(0)}(z) \end{pmatrix} \begin{pmatrix} \Sigma(\xi, t) \\ g(\xi, t) \end{pmatrix} \quad (\text{D.8})$$

Using these evolution equations, it is possible to raise a set of quark and gluon PDFs from one scale to another. Evolution equations can also be obtained for GPDs, in the general case where skewness can be nonzero. See [22] for a set of evolution equations for GPDs.

The value of  $\alpha_s$  also depends on the energy scale, and it changes as the energy scale varies. One way of parametrizing  $\alpha_s$  is presented in [20]. The rate of

change of the running coupling  $\alpha_s$  with respect to the energy scale is presented as a perturbative expansion, and so any analysis using this parametrization can keep the terms up to the desired order. Note that there are certain mass thresholds associated with different quark flavors. The parametrization for  $\alpha_s$  is piecewise, and depends on the energy scale in relation to these mass thresholds.

# Bibliography

- [1] X. Ji and J. Osborne, *Phys. Rev. D* **58**, 094018 (1998).
- [2] X. Ji, *Phys. Rev. D* **55**, 7114 (1997).
- [3] X. Ji, *J. Phys. G* **24**, 1181 (1998).
- [4] S. I. Alekhin, *Phys. Rev. D* **68**, 014002 (2003).
- [5] A. Bacchetta, F. Conti, and M. Radici, *Phys. Rev. D* **78**, 074010 (2008).
- [6] A. V. Belitsky and A. V. Radyushkin, *Phys. Rep.* **418**, 1 (2005).
- [7] G. D. Cates, C. W. de Jager, S. Riordan, and B. Wojtsekhowski, *Phys. Rev. Lett.* **106**, 252003 (2011).
- [8] J. C. Collins and A. Freund, *Phys. Rev. D* **59**, 074009 (1999).
- [9] M. Diehl, Th. Feldmann, R. Jakob, and P. Kroll, *Nucl. Phys. B* **596**, 33 (2001).
- [10] M. Diehl, *Eur. Phys. J. C* **19**, 485 (2001).
- [11] M. Diehl, *Phys. Rep.* **388**, 41 (2003).

- [12] M. Diehl and S. Sapeta, *Eur. Phys. J. C* **41**, 515 (2005).
- [13] M. Diehl and W. Kugler, *Phys. Lett. B* **660**, 202 (2008).
- [14] S. J. Brodsky and F. J. Llanes-Estrada, *Eur. Phys. J. C* **46**, 751 (2006).
- [15] Y. S. Kim and M. E. Noz, *Am. J. Phys.* **50**, 721 (1982).
- [16] W. Melnitchouk, A. W. Schreiber, and A. W. Thomas, *Phys. Rev. D* **49**, 1183 (1994).
- [17] Jaffe, R. L. (1997). Spin, Twist and Hadron Structure in Deep Inelastic Processes. In F. Lenz, H. Griesshammer, and D. Stoll (Eds.), *Lectures on QCD: Applications* (pp. 178-249). Berlin: Springer.
- [18] R. L. Jaffe, MIT-CTP-1261.
- [19] J. J. Kelly, *Phys. Rev. C* **70**, 068202 (2004).
- [20] W. J. Marciano, *Phys. Rev. D* **29**, 580 (1984).
- [21] H. Moutarde, B. Pire, F. Sabatié, L. Szymanowski, and J. Wagner, *Phys. Rev. D* **87**, 054029 (2013).
- [22] K. J. Golec-Biernat and A. D. Martin, *Phys. Rev. D* **59**, 014029 (1998).
- [23] P. V. Pobylitsa, *Phys. Rev. D* **65**, 114015 (2002).
- [24] Ellis, R. K., W. J. Stirling, and B. R. Webber. *QCD and Collider Physics*. Cambridge: Cambridge University Press, 1996. Print.

- [25] Roberts, R. G. *The Structure of the Proton: Deep Inelastic Scattering*.  
Cambridge: Cambridge University Press, 1993. Print.
- [26] F. E. Close, J. Qiu, and R. G. Roberts, *Phys. Rev. D* **40**, 2820 (1989).
- [27] A. V. Belitsky, D. Müller, and A. Kirchner, *Nucl. Phys. B* **629**, 323  
(2002).
- [28] A. Bacchetta, U. D'Alesio, M. Diehl, and C. A. Miller, *Phys. Rev. D* **70**,  
117504 (2004).
- [29] B. Pire, L. Szymanowski, and J. Wagner, *Phys. Rev. D* **83**, 034009 (2011).
- [30] L. Mankiewicz, G. Piller, E. Stein, M. Vanttinen, and T. Weigl, *Phys.*  
*Lett. B* **425**, 186 (1998).
- [31] G. R. Goldstein, J. O. G. Hernandez, and S. Liuti, *Phys. Rev. D* **91**,  
114013 (2015).
- [32] S. Ahmad, H. Honkanen, S. Liuti, and S. K. Taneja, *Eur. Phys. J. C* **63**,  
407 (2009).
- [33] G. R. Goldstein, J. O. G. Hernandez, and S. Liuti, *Phys. Rev. D* **84**,  
034007 (2011).
- [34] J. O. Gonzalez-Hernandez, S. Liuti, G. R. Goldstein, and K. Kathuria,  
*Phys. Rev. C* **88**, 065206 (2013).
- [35] S. Ahmad, H. Honkanen, S. Liuti, and S. K. Taneja, *Phys. Rev. D* **75**,  
094003 (2007).

- [36] S. Ahmad, G. R. Goldstein, and S. Liuti, *Phys. Rev. D* **79**, 054014 (2009).
- [37] Aitchison, I. J. R., and A. J. G. Hey. *Gauge Theories in Particle Physics: A Practical Introduction. Vol. 1, From Relativistic Quantum Mechanics to QED*. New York: Taylor & Francis, 2003. Print.
- [38] A. Airapetian *et al.* (HERMES collaboration), *J. High Energy Phys.* **06** (2008) 066.
- [39] A. Airapetian *et al.* (HERMES collaboration), *Phys. Lett. B* **704**, 15 (2011).
- [40] A. V. Radyushkin, *Phys. Rev. D* **56**, 5524 (1997).
- [41] S. Liuti and S. K. Taneja, *Phys. Rev. D* **70**, 074019 (2004).
- [42] M. Burkardt, *Int. J. Mod. Phys. A* **18**, 173 (2003).
- [43] C. Muñoz Camacho *et al.* (Jefferson Lab Hall A Collaboration), *Phys. Rev. Lett.* **97**, 262002 (2006).